TU WIEN

Dissertation

Axisymmetric Annular Pipe Flow over a Backward-Facing Step on the Inner Cylinder and Its Global Instabilities

ausgeführt zum Zwecke der Erlangung des akademischen Grades des
Doktors der technischen Wissenschaften (PhD)
unter der Leitung von

Univ.Prof. Dipl.-Phys. Dr.rer.nat. Hendrik C. Kuhlmann
Institutsnummer E322
Institut für Strömungsmechanik und Wärmeübertragung

eingereicht an der Technischen Universität Wien

Fakultät für Maschinenwesen und Betriebswissenschaften

von

MEng. Behnaz Beladi
Matrikelnummer 1129951
Viktor-Kaplan-Strasse 6-8/420, 1220 Wien

Wien, 19. September 2017

Abstract

The two-dimensional axisymmetric incompressible Newtonian flow in an annular pipe with a backward-facing step in the radial direction is considered. The flow is driven by a pressure gradient and the radius of the inner cylinder decreases suddenly whereas the radius of the outer cylinder remains constant. In addition, the case in which the flow in an annular pipe expands into a simple pipe is also considered. The inlet and outlet lengths, upstream and downstream of the step, respectively, are selected long enough not to influence the flow. Therefore, the flow is characterized by the Reynolds number, the outlet radius ratio (inner-to-outer radius ratio at the outlet cross section) and expansion ratio (ratio of the step height to the outlet gap). The variation of all three these parameters is investigated.

The axisymmetric steady basic flow is computed discretizing the Navier-Stokes equations by a second-order finite volume method on a staggered grid. The resulting system of algebraic equations is solved using Newton-Raphson method and polynomial line-search strategy is used to globalize the convergence of this method. Reducing the outlet radius ratio, the Reynolds number at which the flow separates from the outer cylinder decreases. The recirculation zones on the outer cylinder and inner outlet cylinder correlate with each other. The growth of the recirculation zone on the inner outlet cylinder with Reynolds number is strongly reduced, as soon as the recirculation zone on the outer cylinder appears. It is seen that by increasing the expansion ratio, the original separation zone on the outer cylinder shrinks in axial direction while it grows radially. As a result, a strong annular jet between two separation zones appears. In comparison with the flow over a backward-facing step in plane channels, the flow separation on the outer cylinder is stronger and by increasing the Reynolds number this separation point moves toward the upstream which leads to arise a strong annular jet on the inner cylinder.

A global temporal linear stability analysis considering three-dimensional perturbations in form of normal modes is performed. An implicitly restarted Arnoldi algorithm and a Cayley transformation are used. Depending on the outlet radius ratio and the expansion ratio, stationary and oscillatory instabilities with different critical azimuthal wave numbers m have been found. We found a pronounced clustering of neutral modes for small radius ratios. In general, deceleration of the flow and lift-up mechanism which arise when a high shear gradient exists were the most important mechanism to destabilize the flow. For small outlet radius ratios, deceleration of the basic flow is found to be the most dominant instability mechanism. Comparing the obtained results with the instability of the flow over a backward-facing step in a plane channel, it can be seen that the cylindrical effect introduced by the annular geometry leads to a much thinner wall jet downstream of the separation zone on the inner cylinder. As a consequence, deceleration and acceleration effects are much more significant in axisymmetric geometries. On the other hand, by increasing the outlet radius ratio, lift-up effects dominate and the instability of the flow over backward-facing step in an annular pipe become more similar to the instability of the plane channel flow over a backward-facing step.

To my beloved parents and to my lovely husband

Acknowledgements

Contents

1. Introduction

1.1. Motivation

The dynamics and stability of annular flows confined within coaxial cylinders are important in many engineering systems, in particular, in the chemical and petrochemical industries. Specific examples are core annular flow in pipeline, the flow between borehole wall and drill pipe, and heat-exchangers [see 47, 33, 32, 50, 93, for review]. The abrupt change of the geometry in annular pipe flows is observed in the industrial applications like drill strings [42] and also in the biomedical applications such as aortic valve stenosis [7].

For instance in the case of drilling oil and gas wells, the fluid which is pupmed along the annulus between the drill colar and borehole wall expands radially inward at the locus where the drill colar connects to the drill pipe. Due to the complexity of drilling fluid including viscoelasticity, shear thinning and Thixotropy and also not precisely defined borehole geometry and the eccentricity of the cylinders, finding the flow behaviour became challenging [3]. To obtain a better understanding of the well bore fluid mechanism, Escudier et al. [33] simplified the problem and performed an exprimental study on the shear thinning liquid flows between two concenteric cylinders in axial direction. Later another experimental work has been done by Escudier and Gouldson [32] on the annular flow in concentric cylinders with a rotating inner cylinder in the absence of pressure gradient. However, these simplified models only considered the annular flow within the stationary and rotating coaxial cylinders and did not considered the effect of geometric discontinuities on the flow behaviour. Therefore to obtain more clear picture and a better understanding of the flow behaviour during drilling, we are highly motivated to investigate the flow behaviour over the backward-facing step in an annular pipe.

It is also very common to observe annular pipe flows with the abrupt change of the geometry in the nature, for example a disease namely aneurysmatic aortas [13, 14]. Abdominal Aortic Aneurysms known as the enlargements of the aorta in the abdomen, is characterized by the development of an intra-luminal thrombus. In order to understand the intra-luminal thrombus development, investigating the blood flow behaviour in the aneurysm which affect the dynamics of platelet is of interest. For this purpose, Biasetti et al. [14] simplified the model and considered the enlargement of the aorta as a backward-facing step in the plane channel. They carried out the Computational Fluid Dynamics (CFD) simulations and the results helped them to better understand how the platelet activates and convectes downstream in the abdominal aortic aneurysms. Considering this simplified fluid dynamic system, the knowledge of pathophysiology of fluid-driven intra-luminal thrombus growth has been improved. However, this simplified model did not considered the effect of the aorta curvature on the blood flow structure. Therefore, as an extension of Biasetti et al. [14] study, this thesis include the curvature effect for this simplified
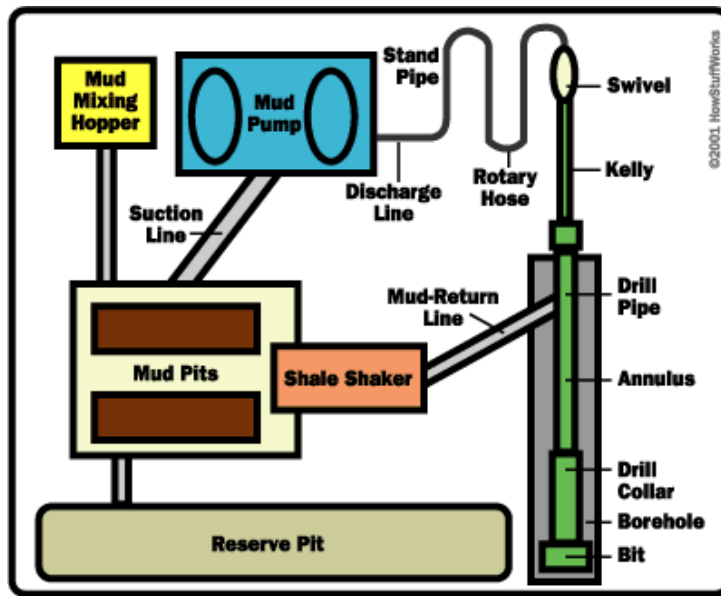
Figure 1.1.: Simplified sketch of the drilling rig [1].

geometry which may help to understand the intra-luminal thrombus development more clear.

Generally, in geometries with an abrupt discontinuity, flow separation may occur, associated with recirculation regions and flow re-attachment. Flow separation, recirculation, and re-attachment significantly affect the performance of engineering systems [21]. Therefore, many researches have been conducted to investigate the flow characteristics in benchmark geometries involving geometric discontinuities in form of sudden expansions or contractions of the cross section of the pipe or plane channel. In these type of geometries, separation emerge at the sharp edge leading to a recirculation zone immediately behind the step. Further downstream the separated flow reattaches to the wall. However, a thorough search of the relevant literature for the flow behaviour over a backward-facing step in an annular pipe yielded only a few related article. This gives further motivation to our study in which we will investigate this configuration in details for the first time.

Not only understanding the flow structure but also stability threshold in the planar or annular configurations is of great interest for designers. As an example for the practical application of stability analysis we refer to the axial flow within the concentric annular pipe which may exprience extreme vibrations known as flutter instability due to the fluid-structure interaction [82]. Since this type of oscillation is self-excited and depends on the interaction between fluid and structure is often called "fluid-elastic instability". This instability may lead to severe damage and failure of the components involved. Therefore, several researchers [80, 81, 67, 68] studied the vibration of cylindrical structures in annular set-ups caused by axial flow in the annular pipes. In many practical situations such as certain types of jet pumps [57], pistons and valves [17] annular-flow induce vibrations which leads to the instability. The most practical as well as theoretical cases of interest were the narrow annular flow passages where the leakage flow induced oscillations [see 67, 73, 79, 43]. Flow separation does not occur for axial flow in an annular pipe, therefore

2

modelling the problem analytically is possible. However, to the best of author's knowledge, there is barely any study on the fluid-elastic instability of axial flow over backward facing step in an annular pipe, where the separation appears. Generally, to find the fluid coupled dynamic system, we need to model both fluid and structure behaviour mathematically. There is hardly any Computational Fluid Dynamics (CFD) code which is capable of computing fully coupled flow-induced vibration for annular geometries with discontinuities. Therefore performing the global linear stability analysis for the rigid structure while we decouple the problem from the structural motion will give us the flow characteristics at the critical Reynolds number where the axisymmetric flow loose its azimuthal symmetry and becomes three dimensional. Some of these characteristics may inherit to flows with higher Reynolds numbers or originate the reasons of the flutter instability at the transient or turbulent regime. Therefore, performing the global linear stability analysis for laminar flow may help us to obtain the better understanding of the flow features at higher Reynolds numbers where the flutter instabillity occur. For flow over backward-facing step in the plane-channel at low Reynolds numbers, the stationary and oscillatory stability boundary and associated instability mechanism are already computed by Lanzerstorfer and Kuhlmann [60]. Therefore this study intend to extend this problem and include the curvature effect by performing three dimensional linear stability analysis for the axial flow over a backward-facing step in an annular pipe.

1.2. Flow in annular geometries

The flow behaviour between two concentric cylinders exhibits a rich variety of phenomena, depending on the radius ratio, the rotating rates of the inner and the outer cylinder, and the axial pressure gradient. In the absence of a pressure gradient the resulting Taylor–Couette problem has been investigated quite extensively [see 96, 5, 55, for a review]. Taylor [96] considered a rotating inner cylinder and fixed outer cylinder. The results showed that at low rotation rates of the inner cylinder, shear flow appears in the annulus between two cylinders. By increasing the inertial forces beyond a critical rotational speed, the laminar azimuthal-Couette flow becomes unstable and it transitions to steady toroidal vortices. Joseph [46] formulated the laminar Poiseuille flow arise due to the constant pressure gradient in an annular pipe in the absence of the rotation analytically. He observed the trace of a dye streak down the annular pipe as a straight line.

1.3. Geometric discontinuity in channel and pipe flows

Several researches have been conducted to understand the flow behaviour in geometries with discontinuities including suddenly expanded flows in axisymmetric pipe [66, 91, 89], suddenly expanded flows in planar geometry [29, 4] and flows over backward-facing step in a plane channel [54, 28, 95, 37, 39, 26, 6, 56, 36]. Macagno and Hung [66] and Badekas and Knight [8] investigated the flow characteristics in a pipe with expansion ratio $\Gamma = 0.5$ and 0.16667 respectively (i.e. the inlet-to-outlet diameter of the pipe). It is shown that the flow at low Reynolds numbers is

steady and two dimensional with two equal recirculation regions behind the expansion corners which are symmetric with respect to the central-plane. Both studies have shown that the length of the recirculation zone varies linearly with the Reynolds number. Mullin et al. [74] performed an experimental study on laminar and time-dependent pipe flows through sudden expansion with the expansion ratio 0.5 (i.e. the inlet-to-outlet diameter of the pipe). They have shown that by increasing the Reynolds number to Re = 1139 ± 10, there is a steady symmetry breaking bifurcation in the flow before the onset of time-dependency. Sanmiguel-Rojas and Mullin [89] carried out three-dimensional simulations for pipe flow through a sudden expansion in the presence of imperfection. They have shown that steady symmetry breaking bifurcation at Re = 1139 ± 10 which was observed by Mullin et al. [74] drived by the small imperfections and in reality there is no steady symmetry breaking bifurcation at this Reynold number. Scott et al. [91] formulated mathematical correlations for both planar and axisymmetric expansions by defining the effect of expansion ratio and Reynolds number on reattachment length of the recirculation zone.

Durst et al. [29] investigated the suddenly expanded flows in two-dimensional duct with a expansion ratio $\Gamma = 0.5$ (i.e. the inlet-to-outlet height of the channel) numerically and experimentally. They have found the critical Reynold number in which the symmetry-breaking arise. For Reynolds numbers higher than critical Reynolds number, the recirculation lengths become unequal. Alleborn et al. [4] observed a sequence of eddies at the corner of the flow passage when Re → 0.

An extensive literature is available for suddenly expanded flows over backward facing step in a plane channel to describe the laminar flow. In general, these studies investigated the effect of different control parameters such as Reynolds number, expansion ratio Γ i.e. the inlet-to-outlet height of the channel, and spanwise extension of the step [107, 101, 75, 15] on the flow behaviour. Armaly et al. [6] carried out an experimental analysis on flow over backward facing step with an expansion ratio $\Gamma = 0.5148$ and showed that the flow is two dimensional for Reynolds number below 300. Comparing the experimental and the numerical results, for Reynolds numbers higher than 300, a discrepancy of primary recirculation length have been found. This deviation is due to the creation of secondary separation bubble on the upper wall. Biswas et al. [15] showed that the primary reattachment length increased by enlarging the expansion ratio. Tylli et al. [101] showed that a wall jet due to the side walls appears at the lower wall of the channel. By increasing the Reynolds number the strength of the wall jet which directed to the mid plane of the channel increased. The wall jet cause the secondary recirculation zone become thinner than in two dimensional flow. The blockage effect reduced when the recirculation zone become thinner which causes growth of the primary recirculation zone. As a further investigation for the flow over backward-facing step, Brücker [20] investigates the transient phase of the starting flow over backward-facing step. For this purpose, he considered the channel with the aspect ratio 5 (i.e. the width-to-height of the step) and presented the obtained mesearments for two Reynolds numbers Re = 1000 and 2200, in which the Reynolds number was defined based on the step height and the steady state mean stream velocity. To capture the temporal evolution of the flow, a three-dimensional scanning PIV method in combination with digital high-speed

video was applied. The results showed that due to the interaction of starting vortex with the side walls, the flow became three-dimensional immidiately. It is also shown that from the early phase of the starting flow until the time that the primary vortex remains connected to the step edge, the streamwise position of the reattachment point almost follows a square root function of the time, while it propagates linear with time as soon as the primary vortex detach from the trailing edge.

Mohamed et al. [71] investigated the separation of annular flow passes over backward-facing step for a single expansion ratio $\Gamma = 0.66667$ (i.e. the inlet-to-outlet height of the annular pipe) and Reynolds numbers less than 400. They have shown that, for $\text{Re} < 100$, the length of the recirculation zone on the inner cylinder changes linearly with Reynolds number. They explained that the steady axisymmetric flow over a radially inward backward-facing step differs from the flow over a backward-facing step in plane channel flow. This differences introduced by the cylindrical geometry. To the best of author's knowledge, there is barely any other study on the flow behaviour over a backward facing step in an annular pipe.

Therefore, the first objective of the present study is to investigate the effect of the transverse curvature on the flow over a backward-facing step. For this purpose, we considered the axisymmetric incompressible Newtonian flow over a backward-facing step in an annular pipe. Fixing the radial expansion ratio to $\Gamma = 0.5$, axisymmetric flows are computed for outlet radius ratios (inner-to-outer outlet radius ratio) in the range $\eta^{\text{out}} \in [0.1, 0.998]$. Since, the differences introduced by the cylindrical geometry are most pronounced for a small radius ratio. Therefore, this study also discussed the basic flow for an outlet radius ratio $\eta^{\text{out}} = 0.1$ and for different expansion ratios in the range $\Gamma = [0.25, 0.75]$. In order to cover a wide range of geometric parameters, the characteristics of two-dimensional axisymmetric annular flow which expands into a simple pipe is also investigated by removing the inner cylinder at the outlet.

1.4. Hydrodynamic stability

A branch of fluid mechanics called hydrodynamic stability analysis investigates the reaction of a flow to an infinitesimal perturbation which may potentially cause the transition of the laminar flow to turbulence. It is worth mentioning the Reynolds [85] famous experimental investigation of the straight pipe flow transition from laminar state to turbulence as one of the early studies on the flow stability. For the first time he identified the non-dimensional group which characterizes the instability at which the laminar flow transitions to the turbulent state. Differently from the cases considered in this thesis work, the instability in a pipe flow is due to non-linear interaction of modes rather than linear instability of single harmonics. However, since we will investigate only linear stabilities in annular pipes, it is worth to mention that this might represent a limitation of our study, which does not deal with finite amplitude perturbations.

1.4.1. Global vs. local instability

Infinitesimal perturbations can grow both in time and space. An extensive review has been done by Drazin and Reid [27] on the stability analysis of parallel flows. In such analysis the

sensitivity of the flow to the disturbance at a specific streamwise station in the flow is determined by analysing the stability of the parallel velocity profile at that point. If the perturbations at the given station, always dissipate with time the flow is considered to be locally stable otherwise, the flow is unstable. There are two types of local instability namely, absolute and convective instability (see [45]). The flow considered to be absolutely unstable, if at a given streamwise station the magnitude of the perturbation grows with time. On the contrary, the flow is defined as convectively unstable when the perturbation grows as it advected upstream/downstream, such that at a fixed spatial location the flow returns to its original state (basic state) as $t \to \infty$. Briggs [19] and Bers [12] were the first ones who introduced and distinguish convective and absolute instabilities in plasmas.

With the increase of computational power, linear stability of the two-dimensional non-parallel flows toward infinitesimal perturbations which falls into the global stability analysis category became feasible. In the global stability analysis, basic flow and any transported perturbations are considered the result of the interaction of global modes. Chomaz et al. [23] explained that a globally unstable flow must necessarily expose a region of local absolute instability. However, local absolute instability of the flow is not a sufficient condition for global instability of the whole flow. This is shown by Giannetti and Luchini [38] for the flow past a very long circular cylinder in which the flow become globally unstable beyond the Reynolds number Re = 47, while a region of absolute instability develops at Reynolds number Re = 25. Therefore, a flow with a sufficiently small region of local absolute instability may remain globally stable.

1.4.2. Instability mechanism

An *a posteriori* energy analysis of the kinetic energy transferred between the basic state and the critical mode has been used in many studies e.g. [60, 76, 2] to understand the instability mechanism. The energy analysis can be traced back to Reynolds [86], and Orr [77] studies. Different types of instability mechanisms may occur in the flow however we only bring a description of the instability mechanisms which we will discuss through this thesis, namely, lift-up mechanism, centrifugal instability and finally flow deceleration.

The lift-up effect comes in to play in the presence of shear flows. Ellingsen and Palm [30] considered initial perturbations with infinitesimal amplitude and identified a linear mechanism known as lift-up which is responsible for the amplification of perturbations in shear flow. In lift-up mechanism, transverse perturbation velocity cause the cross-stream transport of the basic state momentum leading to the amplification of streamwise perturbation momentum. Landahl [59] demonstrated that in lift-up mechanism, the fluid is lift-up from the low velocity regions and intercts with high velocity areas, as a result a three dimensional perturbation is developed into streaks for the inviscid shear flows.

Rayleigh [84] defined centrifugal instability as a type of instability which may arise in circularly symmetric two dimensional inviscid flow in which the magnitude of the fluid angular momentum is reduced by increasing the radius in specific regions of the flow field. For this type of flow, a three dimensional perturbations will grow rapidly which leads to angular momentum redistribution. Later on, Bayly et al. [11] demonestrated that centrifugal instability not only

may arise in circularly symmetric set-ups but also it may occur in any type of settings with the convex closed streamlines which are highly curved.

Deceleration is another mechanism which might lead to instability [60]. In this instability mechanism, the streamwise perturbation momentum amplifies by streamwise transport due to the perturbation flow of basic state momentum.

1.4.3. Instability in annular geometries

Mott and Joseph [72] performed two dimensional linear stability analysis for pressure driven flow between two concentric cylinders and calculated the stability boundary as a function of the radius ratio (i.e. the inner-to-outer radius of the cylinder). They have shown that the critical Reynolds number varies monotonically with changing the radius ratio from the Hagen-Poiseuille flow which is recovered in the limit of vanishing radius ratio to the plane Poiseuille flow which is obtained by approaching the radius ratio to 1. Sadeghi and Higgins [88] carried out two and three dimentional linear stability analysis of pressure driven flow between two concentric cylinders where the inner cylinder moved with the constant speed in axial direction and the outer cylinder considered to be fixed. Their results showed that the velocity of the inner cylinder imposed in the axial direction has a stabilizing effect on all investigated modes.

1.4.4. Instability in geometries with discontinuity

Two-dimensional stability of the plane-channel flow over backward facing step has been investigated by several authors [48, 41, 49, 35] employing a linear stability analysis. Recently, Barkley et al. [10] and Lanzerstorfer and Kuhlmann [60] carried out three dimensional linear stability analysis of the flow over backward facing step in the plane-channel. Barkley et al. [10] considered a single geometry with an expansion ratio $\Gamma = 0.5$ (i.e. the inlet-to-outlet height of the channel) and found the neutral conditions beyond which the symmetry of the two-dimensional flow in the spanwise direction breaks down, giving rise to a three-dimensional steady flow. They further identified the critical Reynolds number $\mathrm{Re}_c = 748$. The computed instability was suspected to be of centrifugal type. Lanzerstorfer and Kuhlmann [60] generalized the problem and computed the critical wave numbers, the critical Reynolds numbers and instability mechanisms for expansion ratios in the range $\Gamma \in [0.25, 0.975]$ (i.e. the step-to-outlet height of the channel). They have shown different types of instabilities appear depending on Γ. Their analysis revealed that the critical Reynold number should be independent of inlet channel length. The mechanisms of instability were analyzed by an *a posteriori* energy analysis of the disturbance flow. For $\Gamma = 0.5$ the basic flow was found to be linearly stable up $\mathrm{Re}_c = 714.05$. The difference with respect to the result of Barkley et al. [10] is due to the longer inlet channel used by Lanzerstorfer and Kuhlmann [60] in order to eliminate the effect of the inlet channel length. Moreover, Lanzerstorfer and Kuhlmann [60] traced back the instability to a combination of different effects including the lift-up mechanism.

Another objective of the current research is to perform a three-dimensional temporal linear stability analysis of flow over backward-facing step in an annular pipe for outlet radius ratios (inner-to-outer outlet radius ratio) in the range $\eta^{\mathrm{out}} \in [0.1, 0.5]$ and a fixed expansion ratio

$\Gamma = 0.5$ (i.e. the step-to-outlet height of the annular pipe). Since, the differences introduced by the cylindrical geometry are most pronounced for a small outlet radius ratio, therefore, this study also obtained the stability boundary as a function of the expansion ratio in the range $\Gamma \in [0.25, 0.75]$ while the outlet radius ratio is fixed to $\eta^{\text{out}} = 0.1$. In the limit case of investigated geometric parameters, the global stability analysis for the flow in an annular pipe which expands into a simple pipe is also performed for three different expansion ratios $\Gamma = 0.75, 0.5, 0.25$. We find the stability boundary beyond which the two-dimensional steady flow becomes an unstable solution of the Navier-Stokes equations. This boundary can be of designers interest when the form of the instability is non-stationary. Under this condition the flutter phenomena might occur because of a coupling between the oscillation frequency of the flow and the natural frequency of the structure. With this study we also provide the parametric conditions under which non-stationary instability occures. Under such conditions, a non-stationary DNS of a fluid structure interaction is required in order to certify the design.

Finally, the last objective of this research is to find the underlying instability mechanisms which leads to the onset of non-axisymmetric motion of the fluid in considered set-ups. Therefore, an *a posteriori* analysis of the kinetic energy transferred between the basic state and the critical mode has been derived based on Reynolds-Orr-equation for the considered set-ups and the flow regions where different type of instabilities localized are obtained by means of kinetic energy analysis.

1.5. Outline of the thesis

In the present thesis, chapter 2 represents the mathematical formulation of the two-dimensional basic flow, three-dimensional linear stability problem and the corresponding boundary conditions as well as the energy analysis. The numerical implementation of the governing equations along with the discretization techniques and the numerical solution methods are explained for computing the basic flow and performing the linear stability analysis in chapter 3. The verification tests of the developed finite volume solver for both the basic state and the stability problem, grid convergence of the calculated results and also the inlet/outlet lengths independent study are presented in chapter 4. The numerical results obtained for the basic state, the linear stability analysis and an *a posteriori* analysis for the considered set-ups and geometric parameters are presented and discussed in chapter 5. In chapter 6, the summary of this study is presented followed by the discussion of the most important results achieved in this thesis. In Appendix A details of the derivation of the energy analysis based on Reynolds–Orr equation for the considered set-ups in cylindrical coordinate is explained.

2. Mathematical Formulation

The incompressible flow of a Newtonian fluid of density ρ and kinematic viscosity ν is considered over two different set-ups. The aims of this study are: 1) to understand the flow behaviour over the considered geometries, 2) to find out the effect of various geometric parameters on the flow behaviour, 3) to investigate the linear stability of a flow in these set-ups. Therefore, this chapter comprises of three main parts. In the first part, two-dimensional flow, 1) over a backward-facing step in an annular pipe and 2) in an annular pipe which transits into a simple pipe will be formulated mathematically. In both cases cylindrical coordinates (r, z, ϕ) are employed. In the second part of this chapter, a three-dimensional temporal linear stability analysis of the obtained steady axisymmetric flows is formulated mathematically. Following the mathematical formulation of the problem for stability analysis, the energy analysis based on the Reynolds–Orr equation is presented in the last part of this chapter.

2.1. Basic flow

2.1.1. Geometry one: Flow over a backward-facing step in an annular pipe

The incompressible flow over a backward-facing step in an annular pipe is considered. The radius of the inner cylinder decreases suddenly from R_i^{in} to R_i^{out} while the radius of the outer cylinder R_o remains constant. The superscripts 'in' and 'out' refer to the inlet and outlet pipe, while the subscripts i and o refer to the inner and outer cylinder, respectively. A sketch of the geometry with annular inlet width $h = R_o - R_i^{\text{in}}$ and outlet width $H = R_o - R_i^{\text{out}}$ is shown in Fig. 2.1. The origin of the cylindrical coordinate system is located on the axis of symmetry and at the locus of the sudden expansion. The inlet and outlet length are shown with L_i and L_o respectively. Together the inlet and outlet lengths define the length of the finite computational domain. With the step height $h_s = H - h$ the geometry is completely characterized, in addition to the in- and outlet lengths, by the non-dimensional expansion ratio and the outlet radius ratio which are defined, respectively, as

$$\Gamma = \frac{h_s}{H}, \qquad \text{and} \qquad \eta^{\text{out}} = \frac{R_i^{\text{out}}}{R_o}. \tag{2.1}$$

The axisymmetric steady flow of an incompressible Newtonian fluid is computed in cylindrical coordinates (r, z) by solving the steady Navier–Stokes and continuity equations. Equation (2.2) shows the dimensional Navier–Stokes and continuity equation. The origin of the cylindrical coordinate system is located on the axis of symmetry and at $z = 0$.

$$\partial_t^* \boldsymbol{u}_0^* + \boldsymbol{u}_0^* \cdot \nabla^* \boldsymbol{u}_0^* = -\frac{1}{\rho}\nabla^* P_0^* + \nu \nabla^{*2} \boldsymbol{u}_0^*, \tag{2.2a}$$

$$\nabla^* \cdot \boldsymbol{u}_0^* = 0 \tag{2.2b}$$

where $\boldsymbol{u}_0^* = u_0^* \boldsymbol{e}_r + v_0^* \boldsymbol{e}_\varphi + w_0^* \boldsymbol{e}_z$ is the velocity vector, P_0^* is the pressure and $\boldsymbol{e}$ denotes the respective unit vectors. ν and ρ are considered to be constant. The subscript 0 and the superscript $*$ are used to indicate a steady axisymmetric flow (basic flow) and dimensional variable respectively. In the present problem, we non-dimensionalized Navier–Stokes and continuity using a convective scaling, as follow

Variable	Length	Velocity	Pressure	Time
Scaling	$(R_o^* - R_i^{\text{out}*})/2$	$w_{\text{in,max}}^*$	$\rho w_{\text{in,max}}^{*2}$	$(R_o^* - R_i^{\text{out}*})/2 w_{\text{in,max}}^*$

Table 2.1.: Convective scaling used to non-dimensionalize Navier–Stokes and continuity equations

here $w_{\text{in,max}}^*$ is the maximum of the inlet velocity profile. Therefore the non-dimensional axisymmetric steady ($\partial_t \boldsymbol{u}_0 = 0$) Navier–Stokes and continuity equations read

$$\boldsymbol{u}_0 \cdot \nabla \boldsymbol{u}_0 = -\nabla P_0 + \frac{1}{\text{Re}}\nabla^2 \boldsymbol{u}_0, \tag{2.3a}$$

$$\nabla \cdot \boldsymbol{u}_0 = 0 \tag{2.3b}$$

where the Reynolds number is defined based on half of the annular gap at the outlet $(R_o - R_i^{\text{out}})/2$ and the maximum inlet velocity of the annular Poiseuille flow $w_{\text{in,max}}$

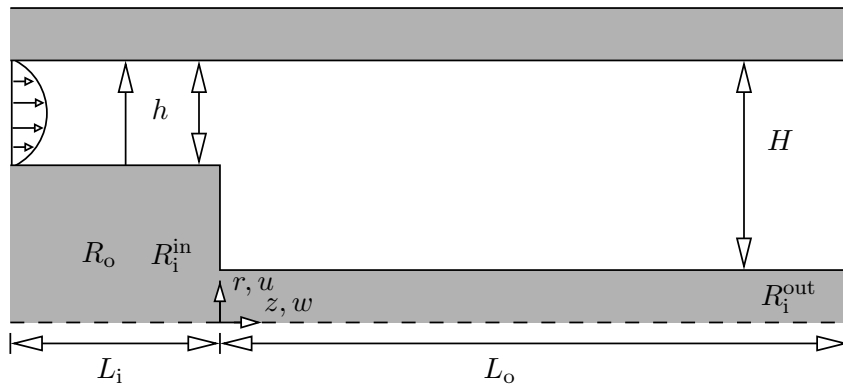$$\text{Re} = \frac{w_{\text{in,max}}^*(R_o^* - R_i^{\text{out}*})}{2\nu}, \tag{2.4}$$

Figure 2.1.: Geometry of the annular backward-facing step and notation. u and w denote the radial and axial velocities, respectively.

At the inlet ($z = -L_\text{i}$, $r \in [R_\text{i}^\text{in}; R_\text{o}]$), we assume a fully developed annular Poiseuille flow

$$\frac{w_\text{in}}{w_\text{in,max}} = \frac{R_\text{i}^\text{in2} - r^2 + (R_\text{o}^2 - R_\text{i}^\text{in2})\ln(r/R_\text{i}^\text{in})}{\ln(R_\text{o}/R_\text{i}^\text{in})\left[R_\text{i}^\text{in2} - r_\text{c}^2 + 2r_\text{c}^2\ln(r_\text{c}/R_\text{i}^\text{in})\right]}, \tag{2.5a}$$

$$u_\text{in} = 0 \tag{2.5b}$$

in which the inlet velocity profile $w_\text{in}(r, z = -L_\text{i})$ takes it maximum value at $r_\text{c} = \left[(R_\text{o}^2 - R_\text{i}^\text{2in})/(2\ln(R_\text{o}/R_\text{i}^\text{in}))\right]^{1/2}$ (for details, see [46]).

No-slip and impermeable boundary conditions are employed along the step and the walls.

$$u_0 = w_0 = 0 \tag{2.6}$$

To have negligible dependence on the finite lenght of the pipe, outlet is located very far downstream of the step ($L_\text{o} = 80$). In this case we set the derivatives of all variables except the pressure, in the main flow direction z to zero at the outlet boundary [102]. The pressure at the outlet is fixed at the ambient pressure p_atm (further details are given in [37]). Therefore, at the outlet ($z = L_\text{o}$, $r \in [R_\text{i}^\text{out}; R_\text{o}]$), a standard outflow boundary condition is imposed (see [37] and [102])

$$\frac{\partial u_0}{\partial z} = \frac{\partial w_0}{\partial z} = 0 \tag{2.7a}$$

$$p_0 = p_\text{atm} \tag{2.7b}$$

2.1.2. Geometry two: Flow in an annular pipe which expands into the simple pipe

An axial fluid flow in an annular pipe which transits to the simple pipe is considered (see Fig. 2.2). The inner cylinder at the inlet has the radius R_i and length L_i and the pipe has the radius R_o and length $L_\text{i} + L_\text{o}$. The origin of the cylindrical coordinate system is located on the axis of symmetry where the inner cylinder ends ($z = L_\text{i}$). This geometry is characterized by non-dimensional expansion ratio which is defined as the radius of the inner cylinder divided by the the radius of the pipe $\Gamma = R_\text{i}/R_\text{o}$.
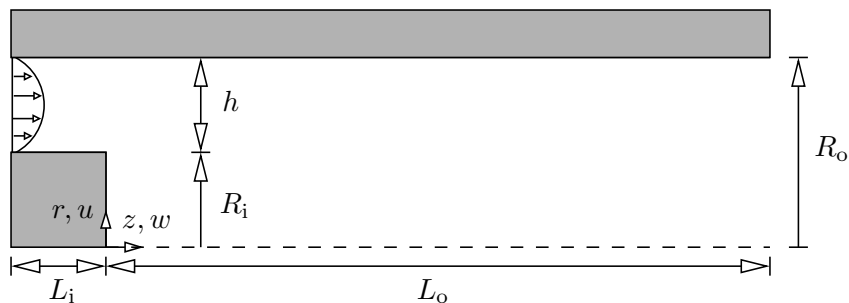

Figure 2.2.: Geometry of an annular pipe which transits into a simple pipe. Notations u and w denote the radial and axial velocities, respectively.

The two-dimensional axisymmetric steady flow of an incompressible fluid is computed in cylindrical coordinates (r, z) by solving the steady Navier–Stokes and continuity equations. Hence, we start from Eqn. (2.2) and non-dimensionalize this equation with the following convective scaling

Variable	Length	Velocity	Pressure	Time
Scaling	$R_\mathrm{o}^*/2$	$w_\mathrm{in,max}^*$	$\rho w_\mathrm{in,max}^{*2}$	$R_\mathrm{o}^*/2w_\mathrm{in,max}^*$

Table 2.2.: Convective scaling used to non-dimensionalize Navier–Stokes and continuity equations

Therefore the non-dimensional axisymmetric steady Navier–Stokes and continuity equations in conservative form are

$$\frac{1}{r}\frac{\partial r u_0^2}{\partial r} + \frac{\partial u_0 w_0}{\partial z} = -\frac{\partial p_0}{\partial r} + \frac{1}{\mathrm{Re}}\left[\frac{1}{r}\frac{\partial}{\partial r}\left(r\frac{\partial u_0}{\partial r}\right) + \frac{\partial^2 u_0}{\partial z^2} - \frac{u_0}{r^2}\right], \tag{2.8a}$$

$$\frac{1}{r}\frac{\partial r u_0 w_0}{\partial r} + \frac{\partial w_0^2}{\partial z} = -\frac{\partial p_0}{\partial z} + \frac{1}{\mathrm{Re}}\left[\frac{1}{r}\frac{\partial}{\partial r}\left(r\frac{\partial w_0}{\partial r}\right) + \frac{\partial^2 w_0}{\partial z^2}\right], \tag{2.8b}$$

$$\frac{1}{r}\frac{\partial r u_0}{\partial r} + \frac{\partial w_0}{\partial z} = 0. \tag{2.8c}$$

At the inlet $(z = -L_\mathrm{i},\ r \in [R_\mathrm{i}; R_\mathrm{o}])$, a fully developed annular Poiseuille flow is employed

$$\frac{w_\mathrm{in}}{w_\mathrm{in,max}} = \frac{R_\mathrm{i}^2 - r^2 + (R_\mathrm{o}^2 - R_\mathrm{i}2)\ln(r/R_\mathrm{i})}{\ln(R_\mathrm{o}/R_\mathrm{i})\left[R_\mathrm{i}^2 - r_\mathrm{c}^2 + 2r_\mathrm{c}^2 \ln(r_\mathrm{c}/R_\mathrm{i})\right]}, \tag{2.9a}$$

$$u_\mathrm{in} = 0 \tag{2.9b}$$

where the inlet velocity profile $w_\mathrm{in}(r, z = -L_\mathrm{i})$ takes it maximum value at $r_\mathrm{c} = \left[(R_\mathrm{o}^2 - R_\mathrm{i}^2)/(2\ln(R_\mathrm{o}/R_\mathrm{i}))\right]^{1/2}$ (for details, see [46]).

For the axis $(r = 0,\ z \in [0; L_\mathrm{o}])$ the following boundary conditions are considered

$$u_0 = \frac{\partial w_0}{\partial r} = 0 \tag{2.10}$$

No-slip and impermeable boundary conditions are imposed at the walls.

$$u_0 = w_0 = 0 \tag{2.11}$$

At the outlet, the standard outflow boundary conditions which are suggested by Gartling [37] and Versteeg [102] are applied

$$\frac{\partial u_0}{\partial z} = \frac{\partial w_0}{\partial z} = 0, \tag{2.12a}$$

$$p_0 = p_\mathrm{atm}. \tag{2.12b}$$

2.2. Linear Stability Analysis

For the global linear stability analysis of the two dimensional basic flow $(\boldsymbol{u}_0, p_0)$, a three-dimensional unsteady Navier–Stokes and continuity equations are considered.

$$\partial_t \boldsymbol{U} + \nabla \cdot (\boldsymbol{U}\boldsymbol{U}) = -\nabla P + \frac{1}{\mathrm{Re}} \nabla^2 \boldsymbol{U}, \tag{2.13a}$$

$$\nabla \cdot \boldsymbol{U} = 0 \tag{2.13b}$$

here $\boldsymbol{U} = (U, W, V)$ is the total velocity field, where U, V and W denote the radial, azimuthal and axial velocities, respectively, and P is the total pressure field.

Equation (2.13) is non-dimensionalized using the convective scaling shown in Table 2.1 for the flow over backward-facing step in an annular pipe and the convective scaling shown in Table. 2.2 for the flow over cylindrical rod in a pipe. In order to obtain perturbation equations, the total flow fields $\boldsymbol{U}$ and P are decomposed into a basic $(\boldsymbol{u}_0, p_0)$ and a perturbation flow $(\tilde{\boldsymbol{u}}, \tilde{p})$

$$\boldsymbol{U} = \boldsymbol{u}_0 + \tilde{\boldsymbol{u}}, \tag{2.14a}$$

$$P = p_0 + \tilde{p} \tag{2.14b}$$

Since the basic state $(\boldsymbol{u}_0, p_0)$ satisfies the Navier–Stokes equations, by substituting Eqn. (2.14) into the Eqn. (2.13), the non-linear perturbation equation is obtained as follow

$$\partial_t \tilde{\boldsymbol{u}} + \boldsymbol{u}_0 \cdot \nabla \tilde{\boldsymbol{u}} + \tilde{\boldsymbol{u}} \cdot \nabla \boldsymbol{u}_0 + \tilde{\boldsymbol{u}} \cdot \nabla \tilde{\boldsymbol{u}} = -\nabla \tilde{p} + \frac{1}{\mathrm{Re}} \nabla^2 \tilde{\boldsymbol{u}}, \tag{2.15a}$$

$$\nabla \cdot \tilde{\boldsymbol{u}} = 0 \tag{2.15b}$$

Considering infinitely small perturbations $\tilde{\boldsymbol{u}} = (\tilde{u}, \tilde{w}, \tilde{v})$, we arrive at the linearised perturbation equations as follow

$$\frac{\partial \tilde{u}}{\partial t} + \left[\left(\frac{1}{r} + \frac{\partial}{\partial r} \right) (2u_0 \tilde{u}) + \frac{1}{r} \frac{\partial u_0 \tilde{v}}{\partial \varphi} + \frac{\partial (u_0 \tilde{w} + \tilde{u} w_0)}{\partial z} \right] \tag{2.16a}$$
$$= -\frac{\partial \tilde{p}}{\partial r} + \frac{1}{\mathrm{Re}} \left[\frac{1}{r} \frac{\partial}{\partial r} \left(\frac{r \partial \tilde{u}}{\partial r} \right) + \frac{\partial^2 \tilde{u}}{\partial z^2} - \frac{\tilde{u}}{r^2} - \frac{2}{r^2} \frac{\partial \tilde{v}}{\partial \varphi} + \frac{1}{r^2} \frac{\partial^2 \tilde{u}}{\partial \varphi^2} \right],$$

$$\frac{\partial \tilde{w}}{\partial t} + \left[\left(\frac{1}{r} + \frac{\partial}{\partial r} \right) (w_0 \tilde{u} + \tilde{w} u_0) + \frac{1}{r} \frac{\partial w_0 \tilde{v}}{\partial \varphi} + \frac{\partial (2 w_0 \tilde{w})}{\partial z} \right] \tag{2.16b}$$
$$= -\frac{\partial \tilde{p}}{\partial z} + \frac{1}{\mathrm{Re}} \left[\frac{1}{r} \frac{\partial}{\partial r} \left(\frac{r \partial \tilde{w}}{\partial r} \right) + \frac{\partial^2 \tilde{w}}{\partial z^2} + \frac{1}{r^2} \frac{\partial^2 \tilde{w}}{\partial \varphi^2} \right],$$

$$\frac{\partial \tilde{v}}{\partial t} + \left[\left(\frac{2}{r} + \frac{\partial}{\partial r} \right) u_0 \tilde{v} + \frac{\partial w_0 \tilde{v}}{\partial z} \right] \tag{2.16c}$$
$$= -\frac{1}{r} \frac{\partial \tilde{p}}{\partial \varphi} + \frac{1}{\mathrm{Re}} \left[\frac{1}{r} \frac{\partial}{\partial r} \left(\frac{r \partial \tilde{v}}{\partial r} \right) + \frac{2}{r^2} \frac{\partial \tilde{u}}{\partial \varphi} - \frac{\tilde{v}}{r^2} + \frac{1}{r^2} \frac{\partial^2 \tilde{v}}{\partial \varphi^2} + \frac{\partial^2 \tilde{v}}{\partial z^2} \right],$$

$$\frac{1}{r} \frac{\partial r \tilde{u}}{\partial r} + \frac{1}{r} \frac{\partial \tilde{v}}{\partial \varphi} + \frac{\partial \tilde{w}}{\partial z} = 0. \tag{2.16d}$$

In geometries with a homogeneous third direction, the linear solution $\tilde{\boldsymbol{u}}$ can be decomposed into a Fourier series. The azimuthal symmetry in cylindrical coordinate results in a Fourier decomposition with azimuthal modes. Therefore, solutions to the perturbation equations are sought in form of normal modes

$$[\tilde{u}, \tilde{w}, \tilde{v}, \tilde{p}]^{\mathrm{T}} = [\hat{u}, \hat{w}, \hat{v}, \hat{p}]^{\mathrm{T}}(r, z)e^{-\gamma t + \mathrm{i}m\varphi} + \text{c.c.}, \tag{2.17}$$

where $\hat{u}, \hat{w}, \hat{v}$ and $\hat{p}$ are functions of r and z only, m is the integer azimuthal wave number and $\gamma = \sigma + \mathrm{i}\omega$ the temporal complex decay rate with real decay rate $\sigma = \Re(\gamma)$ and angular oscillation frequency $\omega = \Im(\gamma)$. The linear nature of the solution $\tilde{\boldsymbol{u}}$ results in a decoupling of these waves, allowing the solutions for individual wavenumbers, m, to be computed separately in a two-dimensional context.

Inserting Eqn. (2.17) into the linear perturbation equations Eqn. (2.16) leads to an eigenvalue problem in form of linear differential equations in r and z for $\hat{u}$, $\hat{w}$, $\hat{v}$ and $\hat{p}$.

$$\frac{\partial \hat{p}}{\partial r} - \frac{1}{\mathrm{Re}}\left[\frac{1}{r}\frac{\partial}{\partial r}\left(r\frac{\partial \hat{u}}{\partial r}\right) + \frac{\partial^2 \hat{u}}{\partial z^2} - (m^2 + 1)\frac{\hat{u}}{r^2} - \mathrm{i}m\frac{2\hat{v}}{r^2}\right] + \tag{2.18a}$$

$$\left[\left(\frac{1}{r} + \frac{\partial}{\partial r}\right)(2u_0\hat{u}) + \mathrm{i}m\frac{u_0\hat{v}}{r} + \frac{\partial(u_0\hat{w} + \hat{u}w_0)}{\partial z}\right] = \gamma\hat{u},$$

$$\frac{\partial \hat{p}}{\partial z} - \frac{1}{\mathrm{Re}}\left[\frac{1}{r}\frac{\partial}{\partial r}\left(r\frac{\partial \hat{w}}{\partial r}\right) + \frac{\partial^2 \hat{w}}{\partial z^2} - m^2\frac{\hat{w}}{r^2}\right] + \tag{2.18b}$$

$$\left[\frac{1}{r}\frac{\partial r(w_0\hat{u} + \hat{w}u_0)}{\partial r} + \mathrm{i}m\frac{w_0\hat{v}}{r} + \frac{\partial(2w_0\hat{w})}{\partial z}\right] = \gamma\hat{w},$$

$$\mathrm{i}m\frac{1}{r}\hat{p} - \frac{1}{\mathrm{Re}}\left[\mathrm{i}m\frac{2}{r^2}\hat{u} + \frac{1}{r}\frac{\partial}{\partial r}\left(r\frac{\partial \hat{v}}{\partial r}\right) - (m^2 + 1)\frac{\hat{v}}{r^2} + \frac{\partial^2 \hat{v}}{\partial z^2}\right] + \tag{2.18c}$$

$$\left[\left(\frac{2}{r} + \frac{\partial}{\partial r}\right)u_0\hat{v} + \frac{\partial w_0\hat{v}}{\partial z}\right] = \gamma\hat{v},$$

$$\frac{1}{r}\frac{\partial r\hat{u}}{\partial r} + \mathrm{i}m\frac{\hat{v}}{r} + \frac{\partial \hat{w}}{\partial z} = 0. \tag{2.18d}$$

The following boundary conditions for the flow over backward-facing step in an annular pipe is applied.

Since the physical boundary conditions are taken care of by the basic state the following boundary conditions are employed for the considered set-ups (for details, see [98]).

Due to the no-slip conditions for $\boldsymbol{u}$ the perturbation flow should vanish on the all solid boundaries. Since the perturbation flow is expected to be localized near the backward-facing step [16, 60] the perturbations should not affect the flow at the inlet. Therefore, we also assume the perturbation flow and the perturbation pressure to vanish at $z = -L_{\mathrm{i}}$.

$$\hat{u} = \hat{w} = \hat{v} = 0 \tag{2.19}$$

The boundary conditions at the outlet are given by

$$\frac{\partial \hat{u}}{\partial z} = \frac{\partial \hat{w}}{\partial z} = \hat{v} = \hat{p} = 0 \tag{2.20}$$

Different boundary conditions are implemented for the axis of symmetry depending on the azimuthal wave number m. Equations (2.21a)–(2.21c) show the boundary conditions on the axis of symmetry which are used in this study.

$$\text{For} \quad m = 0 \Rightarrow \hat{u} = 0, \quad \partial_r \hat{w} = 0 \tag{2.21a}$$

$$\text{For} \quad m = 1 \Rightarrow \partial_r \hat{u} = 0, \quad \hat{w} = 0 \tag{2.21b}$$

$$\text{For} \quad m > 1 \Rightarrow \hat{u} = 0, \quad \hat{w} = 0 \tag{2.21c}$$

The basic flow is linearly stable if $\sigma > 0$ (normal mode decay), unstable if $\sigma < 0$ (normal mode grow) and neutrally stable if $\sigma = 0$. Neutral Reynolds numbers Re_n and associated neutral modes for given azimuthal wave number m are found by searching the lowest zero of the real growth rate σ. In this study, we are interested in the linear stability boundary $\text{Re}_c(\Gamma, \eta^{\text{out}}) = \min_{m,k} \text{Re}_n(m, k, \Gamma, \eta^{\text{out}})$, where $\text{Re}_n(m, k, \Gamma, \eta^{\text{out}})$ is the neutral Reynolds number and k denote the discrete part of the spectrum of eigenvalues associated with the radial and axial coordinates. The critical Reynolds number Re_c is then obtained as the envelope of all neutral curves.

2.3. A posteriori energy analysis

An *a posteriori* analysis of the kinetic energy transferred between the basic state and the critical mode is very useful to identify the physical instability mechanisms and to check the overall energy conservation. To that end we numerically evaluate all terms of the Reynolds-Orr-equation. A detailed discussion of each term derivation is presented in appendix A.

$$\frac{1}{D}\frac{\mathrm{d}E^{\text{kin}}}{\mathrm{d}t} = -1 + \sum_{n=1}^{5} \int_V I_i(I_i')\mathrm{d}V + K^{\text{out}}, \tag{2.22}$$

where E^{kin} is the total kinetic energy, D the viscous dissipation which reads as

$$D = \int_V \left[\left(\frac{\partial \tilde{u}}{\partial r}\right)^2 + \left(\frac{1}{r}\frac{\partial \tilde{u}}{\partial \varphi} - \frac{\tilde{v}}{r}\right)^2 + \left(\frac{\partial \tilde{u}}{\partial z}\right)^2 + \left(\frac{\partial \tilde{v}}{\partial r}\right)^2 + \left(\frac{1}{r}\frac{\partial \tilde{v}}{\partial \varphi} + \frac{\tilde{u}}{r}\right)^2 \right.$$
$$\left. + \left(\frac{\partial \tilde{v}}{\partial z}\right)^2 + \left(\frac{\partial \tilde{w}}{\partial r}\right)^2 + \left(\frac{1}{r}\frac{\partial \tilde{w}}{\partial \varphi}\right)^2 + \left(\frac{\partial \tilde{w}}{\partial z}\right)^2 \right] \mathrm{d}V, \tag{2.23}$$

and K^{out} the transport of perturbation energy through the outlet surface S^{out} (see Eqn. (2.24)).

$$K^{\text{out}} = -\frac{1}{2D}\text{Re}\int_S w_0 \tilde{w}^2 \mathrm{d}S^{\text{out}} \tag{2.24}$$

There is no advection of perturbation energy through the inlet surface S^{in}, because the perturbation velocity $\tilde{\boldsymbol{u}} = 0$ is enforced to vanish at the inlet. Since we also assumed a zero pressure perturbation at the outlet $\tilde{p} = 0$, there is no change of kinetic energy by pressure forces.

The total local energy production in the bulk is independent of the coordinate system used. In cylindrical coordinates local energy-transfer terms as given by I_{i} which normalized by the total dissipation D, are

$$
\begin{aligned}
I_1 &= -\frac{1}{D}\tilde{w}^2\frac{\partial w_0}{\partial z}, & I_2 &= -\frac{1}{D}\tilde{w}\tilde{u}\frac{\partial w_0}{\partial r}, \\
I_3 &= -\frac{1}{D}\tilde{u}\tilde{w}\frac{\partial u_0}{\partial z}, & I_4 &= -\frac{1}{D}\tilde{u}^2\frac{\partial u_0}{\partial r}, \\
I_5 &= -\frac{1}{D}\tilde{v}^2\frac{u_0}{r}.
\end{aligned}
\tag{2.25}
$$

In streamline coordinates [2] the perturbation flow is decomposed into

$$
\tilde{\boldsymbol{u}} = \tilde{\boldsymbol{u}}_{\parallel} + \tilde{\boldsymbol{u}}_{\perp} + \tilde{\boldsymbol{u}}_{\varphi},
\tag{2.26}
$$

where $\tilde{\boldsymbol{u}}_{\parallel}$ denotes the perturbation velocity in direction of the basic flow, $\tilde{\boldsymbol{u}}_{\perp}$ is the perturbation velocity perpendicular to the basic flow in the (r, z) plane, and $\tilde{\boldsymbol{u}}_{\varphi}$ represents the perturbation velocities in azimuthal direction. Using this decomposition the normalized local energy-transfer terms as given by I_{i}' are obtained as

$$
\begin{aligned}
I_1' &= -\frac{1}{D}\tilde{\boldsymbol{u}}_{\perp}\cdot\left(\tilde{\boldsymbol{u}}_{\perp}\cdot\nabla\boldsymbol{u}_0\right), & I_2' &= -\frac{1}{D}\tilde{\boldsymbol{u}}_{\parallel}\cdot\left(\tilde{\boldsymbol{u}}_{\perp}\cdot\nabla\boldsymbol{u}_0\right), \\
I_3' &= -\frac{1}{D}\tilde{\boldsymbol{u}}_{\perp}\cdot\left(\tilde{\boldsymbol{u}}_{\parallel}\cdot\nabla\boldsymbol{u}_0\right), & I_4' &= -\frac{1}{D}\tilde{\boldsymbol{u}}_{\parallel}\cdot\left(\tilde{\boldsymbol{u}}_{\parallel}\cdot\nabla\boldsymbol{u}_0\right), \\
I_5' &= -\frac{1}{D}\tilde{\boldsymbol{u}}_{\varphi}\cdot\left(\tilde{\boldsymbol{u}}_{\varphi}\cdot\nabla\boldsymbol{u}_0\right).
\end{aligned}
\tag{2.27}
$$

Expanding Eqn. (2.27) results in

$$
\begin{aligned}
I_1' &= -\frac{1}{D}\left(\tilde{w}_{\perp}^2\frac{\partial w_0}{\partial z} + \tilde{w}_{\perp}\tilde{u}_{\perp}\frac{\partial w_0}{\partial r} + \tilde{u}_{\perp}\tilde{w}_{\perp}\frac{\partial u_0}{\partial z} + \tilde{u}_{\perp}^2\frac{\partial u_0}{\partial r}\right), \tag{2.28} \\
I_2' &= -\frac{1}{D}\left(\tilde{w}_{\parallel}\tilde{w}_{\perp}\frac{\partial w_0}{\partial z} + \tilde{w}_{\parallel}\tilde{u}_{\perp}\frac{\partial w_0}{\partial r} + \tilde{u}_{\parallel}\tilde{w}_{\perp}\frac{\partial u_0}{\partial z} + \tilde{u}_{\parallel}\tilde{u}_{\perp}\frac{\partial u_0}{\partial r}\right), \\
I_3' &= -\frac{1}{D}\left(\tilde{w}_{\parallel}\tilde{w}_{\perp}\frac{\partial w_0}{\partial z} + \tilde{w}_{\perp}\tilde{u}_{\parallel}\frac{\partial w_0}{\partial r} + \tilde{u}_{\perp}\tilde{w}_{\parallel}\frac{\partial u_0}{\partial z} + \tilde{u}_{\parallel}\tilde{u}_{\perp}\frac{\partial u_0}{\partial r}\right), \\
I_4' &= -\frac{1}{D}\left(\tilde{w}_{\parallel}^2\frac{\partial w_0}{\partial z} + \tilde{w}_{\parallel}\tilde{u}_{\parallel}\frac{\partial w_0}{\partial r} + \tilde{u}_{\parallel}\tilde{w}_{\parallel}\frac{\partial u_0}{\partial z} + \tilde{u}_{\parallel}^2\frac{\partial u_0}{\partial r}\right), \\
I_5' &= -\frac{1}{D}\left(\tilde{v}^2\frac{u_0}{r}\right).
\end{aligned}
$$

A positive (negative) value of $I_{\text{i}}(I_{\text{i}}')$ indicates energy gain (loss) of the perturbation by the mechanism represented by $I_{\text{i}}(I_{\text{i}}')$. Since the energy of the critical mode must be preserved, at

the threshold to instability of kinetic energy of the disturbance flow should satisfy

$$\sum_{i=1}^{5} \int_V I_i' \mathrm{d}V = \sum_{i=1}^{5} \int_V I_i \mathrm{d}V = 1, \tag{2.29}$$

due to the conservation. Here $I_i'(I_i)$ denote the normalized local integral energy-transfer terms. This condition can be used as an additional check of the numerics.

3. Numerical Implementation

3.1. Finite Volume Discretization

In order to discretize partial differential equations (2.8a)–(2.8c) numerically, we employed finite volume method on a staggered grid. This method is a natural approach for fluid dynamics and it is well-established in the literature ([34], [63], [102], [106], [60]). Our study extended the numerical code developed by Lanzerstorfer and Kuhlmann [60], for the backward-facing step in plane channels, in order to consider cylindrical geometries. The left side of Fig. 3.1 shows the schematic sketch of two dimensional staggered grid for considered geometries and the right side of this figure represents a two-dimensional finite volume cell centered at (i, j). In this sketch the indices for radial r and axial z directions are indicated by subscript i and j respectively. Here the grid nodes are numbered as $i = 1, ..., I$, $j = 1, ..., J$. The velocity components are located on the cell faces and the pressure is placed at the cell center, therefore we have the combination of vertex and cell centred discretization (see details in [106]). In order to discretize the equations care has to be taken about interior and boundary points. Filled black symbols in Fig. 3.1 stands for interior points, while grey filled symbols represent boundary points and the open symboles are the ghost nodes.
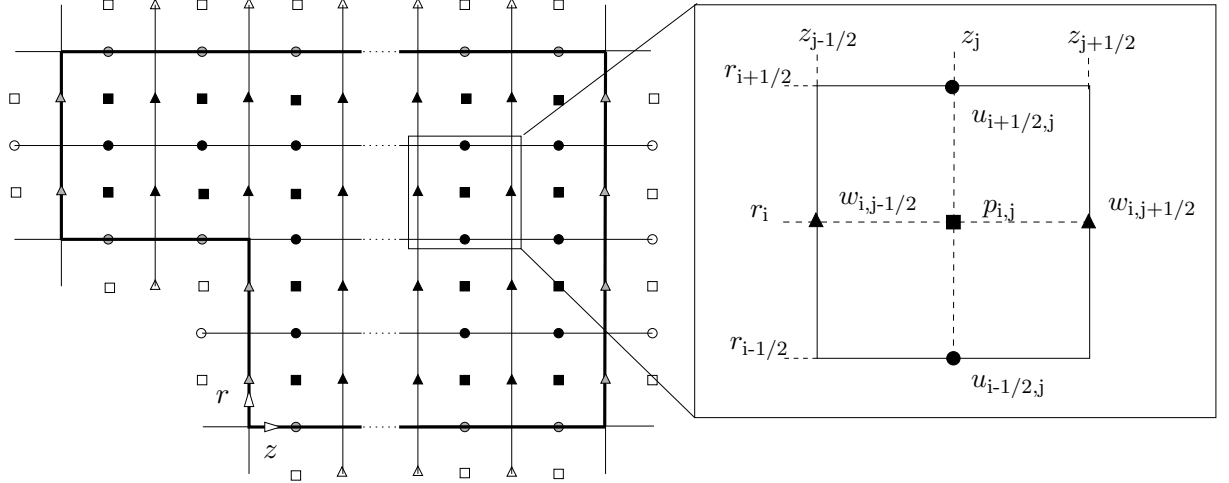
Figure 3.1.: Schematic sketch of two dimensional staggered grid for considered geometries (left), two dimensional finite volume cell of a grid point (i,j) (right)

In this study, pressure nodes $p_{i,j}$ are located at the (r_i, z_j) which is considered as the center for the pressure control volume $\Omega_{i,j}^p$. Radial velocities $u_{i,j}$ are located at the $(r_{i+1/2}, z_j)$ and the locus of axial velocities $w_{i,j}$ are at the positions $(r_i, z_{j+1/2})$ which are construct the centers for

the radial velocity control volume $\Omega^{\mathrm{u}}_{\mathrm{i,j}}$ and axial velocity control volume $\Omega^{\mathrm{w}}_{\mathrm{i,j}}$ respectively. The corresponding two-dimensional control volumes for pressure p, axial velocity component w, and radial velocity component u are as follow

$$\Omega^{\mathrm{p}}_{\mathrm{i,j}} = [r_{\mathrm{i\text{-}1/2}}, r_{\mathrm{i+1/2}}] \times [z_{\mathrm{j\text{-}1/2}}, z_{\mathrm{j+1/2}}], \tag{3.1a}$$

$$\Omega^{\mathrm{w}}_{\mathrm{i,j}} = [r_{\mathrm{i\text{-}1/2}}, r_{\mathrm{i+1/2}}] \times [z_{\mathrm{j}}, z_{\mathrm{j+1}}], \tag{3.1b}$$

$$\Omega^{\mathrm{u}}_{\mathrm{i,j}} = [r_{\mathrm{i}}, r_{\mathrm{i+1}}] \times [z_{\mathrm{j\text{-}1/2}}, z_{\mathrm{j+1/2}}]. \tag{3.1c}$$

In the two-dimensional computational domain in (r, z) plane, $N^{\mathrm{in}}_{\mathrm{z}}$, $N^{\mathrm{in}}_{\mathrm{r}}$, $N^{\mathrm{out}}_{\mathrm{z}}$, and $N^{\mathrm{out}}_{\mathrm{r}}$ denote the total number of cells in the inlet and the outlet part of the annulus and in z and r directions, respectively. Therefore we have $\left[(N^{\mathrm{in}}_{\mathrm{z}} + 1) \times N^{\mathrm{in}}_{\mathrm{r}} + (N^{\mathrm{out}}_{\mathrm{z}} + 1) \times N^{\mathrm{out}}_{\mathrm{r}}\right]$ cells for axial velocity component w, $\left[(N^{\mathrm{in}}_{\mathrm{r}} + 1) \times N^{\mathrm{in}}_{\mathrm{z}} + (N^{\mathrm{out}}_{\mathrm{r}} + 1) \times N^{\mathrm{out}}_{\mathrm{z}}\right]$ cells for radial velocity component u, and $\left[(N^{\mathrm{in}}_{\mathrm{r}} \times N^{\mathrm{in}}_{\mathrm{z}}) + (N^{\mathrm{out}}_{\mathrm{r}} \times N^{\mathrm{out}}_{\mathrm{z}})\right]$ cells for pressure p. The horizontal and vertical sides of $\Omega_{\mathrm{i,j}}$ have the lengths $l^{\mathrm{z}}_{\mathrm{j}}$ and $l^{\mathrm{r}}_{\mathrm{i}}$ respectively. As a representative example, in the following, the discretization of continuity equation (2.8c) using finite volume method is shown. For this purpose, Eqn. (2.8c) is integrated over a two dimensional control volume $\Omega^{\mathrm{p}}_{\mathrm{i,j}}$

$$\int_{r_{\mathrm{i\text{-}1/2}}}^{r_{\mathrm{i+1/2}}} \int_{z_{\mathrm{j\text{-}1/2}}}^{z_{\mathrm{j+1/2}}} \left(\frac{1}{r} \frac{\partial r u_0}{\partial r} + \frac{\partial w_0}{\partial z} \right) r \mathrm{d}z \mathrm{d}r = 0 \tag{3.2}$$

which yields to

$$\int_{z_{\mathrm{j\text{-}1/2}}}^{z_{\mathrm{j+1/2}}} (r u_0)|^{r_{\mathrm{i+1/2}}}_{r_{\mathrm{i\text{-}1/2}}} dz + \int_{r_{\mathrm{i\text{-}1/2}}}^{r_{\mathrm{i+1/2}}} r(w_0)|^{z_{\mathrm{j+1/2}}}_{z_{\mathrm{j\text{-}1/2}}} \mathrm{d}r = 0 \tag{3.3}$$

Applying the midpoint rule [34], results in

$$(z_{\mathrm{j+1/2}} - z_{\mathrm{j\text{-}1/2}})(r u_0)|^{r_{\mathrm{i+1/2}}}_{r_{\mathrm{i\text{-}1/2}}} + (r_{\mathrm{i+1/2}} - r_{\mathrm{i\text{-}1/2}}) r_{\mathrm{i}}(w_0)|^{z_{\mathrm{j+1/2}}}_{z_{\mathrm{j\text{-}1/2}}} = 0 \tag{3.4}$$

which is of the second order. As it is seen in Eqn. (3.4), no further approximation is necessary in this equation due to the staggered placement of the unknowns. Equations (2.8a) and (2.8b) are discretized by finite volume method in a similar way. In the discretization of the momentum equations (2.8a), (2.8b), no further approximation is necessary for p_0 because it is occured only in its nodal points. However w_0, u_0 and derivatives should be calculated in terms of neighboring nodes. Therefore, the derivatives are estimated by the second order central difference scheme as follow

$$\partial_z w|_{\mathrm{i,j}} \approx \frac{(w_{\mathrm{i,j+1/2}} - w_{\mathrm{i,j\text{-}1/2}})}{l^{\mathrm{z}}_{\mathrm{j}}} \tag{3.5a}$$

$$\partial_r w|_{i\text{-}1/2,j+1/2} \approx \frac{(w_{i,j+1/2} - w_{i\text{-}1,j+1/2})}{l^r_{i\text{-}1/2}} \tag{3.5b}$$

$$\partial_r u|_{i,j} \approx \frac{(u_{i+1/2,j} - u_{i\text{-}1/2,j})}{l^r_i} \tag{3.5c}$$

$$\partial_z u|_{i+1/2,j\text{-}1/2} \approx \frac{(u_{i+1/2,j} - u_{i+1/2,j\text{-}1})}{l^z_{j\text{-}1/2}} \tag{3.5d}$$

here $l^r_{i\text{-}1/2} = (l^r_i + l^r_{i\text{-}1})/2$ and $l^z_{j\text{-}1/2} = (l^z_j + l^z_{j\text{-}1})/2$. For the convenience of notation, we eliminate the subscript 0 of the flow quantities. In order to discretize the inertia terms, the value of the variables should be approximated at the points which do not occur on the nodal points. Therefore, the linear interpolation (see [34]) which is consistent with the second order of the scheme is applied. After completing finite volume discretization in the interior, the boundary conditions are implemented on the existing staggered grid.

Considering the staggered grid, some points are located on the boundary whereas the others have a boundary between them. At points that lie on the boundary Dirichlet boundary conditions are directly prescribed. Therefore, in the annular pipe with one sided sudden expansion, Dirichlet boundary conditions for w_0 at the inflow boundary ($z = -L_i$, $r \in [R^{in}_i; R_o]$) and vertical lenght of the step ($z = 0$, $r \in [R^{out}_i; R^{in}_i]$) and u_0 at the bottom and top walls ($z \in [0, L_o]$, $r = R^{out}_i$ and $z \in [-L_i, L_o]$, $r = R_o$) and along the horizontal length of the step ($z \in [-L_i, 0]$, $r = R^{in}_i$) are implemented directly. For the w_0 at the boundaries ($z \in [0, L_o]$, $r = R^{out}_i$, ($z \in [-L_i, L_o]$, $r = R_o$), ($z \in [-L_i, 0]$, $r = R^{in}_i$) and for the u_0 at the boundaries ($z = -L_i$, $r \in [R^{in}_i; R_o]$), ($z = 0$, $r \in [R^{out}_i; R^{in}_i]$), we consider a row and a column of ghost cells outside the domain with virtual nodes (see open symbols in Fig. 3.1). The ghost cells are assumed to be of the same size with the neighboring ones inside the domain. Therefore we defined the value on the boundary as the average of two data points. For instance no-slip boundary condition at the bottom wall ($z \in [0, L_o]$, $r = R^{out}_i$) is defined as the average of the axial velocity w_0 at nodes i = 1 and at the virtual nodes i = 0

$$\frac{w_{1,j+1/2} + w_{0,j+1/2}}{2} = 0 \tag{3.6}$$

All the considered virtual values are eliminated by taking into account the defined Dirichlet boundary conditions. Therefore, in this study, we do not need to define any virtual value for the ghost nodes. As an example, in discretizing the momentum equation, derivative of w_0 in r direction needs to be approximated by means of surrounding nodes. By substituting i = 1 into Eqn. (3.5b), we obtain

$$\partial_r w|_{1/2,j+1/2} \approx \frac{(w_{1,j+1/2} - w_{0,j+1/2})}{l^r_{1/2}} \tag{3.7}$$

Therefore, in order to calculate the $\partial_r w|_{1/2,j+1/2}$ using the finite volume scheme, we need to know the value of the virtual node $w_{0,j+1/2}$ which is located outside the domain. In this case

the virtual value $w_{0,j+1/2}$ is eliminated by considering the no-slip boundary condition (see Eqn. (3.6)) at the bottom wall ($z \in [0, L_o]$, $r = R_i^{\text{out}}$).

By discretizing the momentum equation we have to calculate $\partial_r w|_{i+1/2, J+1/2} \approx (w_{i+1, \ J+1/2} - w_{i, \ J+1/2}/l_{i+1/2}^{r})$ and $\partial_z u|_{i+1/2, J+1/2} \approx (u_{i+1/2, \ J+1} - u_{i+1/2, \ J}/l_{J+1/2}^{z})$ at the outlet. Therefore, the values of the virtual nodes $w_{I+1, \ J+1/2}$ and $u_{i+1/2, \ J+1}$ is needed. Considering the Neumann boundary conditions $\partial_z u = \partial_z w = 0$ at the outlet, the ghost values $u_{i+1/2, \ J+1}$ and $w_{I+1, \ J+1/2}$ are eliminated

$$\frac{u_{i+1/2, \ J+1} - u_{i+1/2, \ J}}{l_{J+1/2}^{z}} = 0 \tag{3.8a}$$

$$\frac{w_{I+1, \ J+1/2} - w_{I, \ J+1/2}}{l_{J+1/2}^{z}} = 0 \tag{3.8b}$$

By descretizing the momentum equations, $p_{I,J+1}$ is needed to be determind. This ghost node can be eliminated by considering the boundary conditions for the pressure at the outlet as follow

$$\frac{p_{I,J} + p_{I \ + \ J+1}}{2} = p_{\text{atm}} \tag{3.9}$$

where p_{atm} is the ambient pressure.

In the pipe with the cylindrical insert the boundary conditions are implemented in the same way as described for the annular pipe with sudden expansion except for the axis ($z \in [0, L_o]$, $r = 0$) in which a Neumann boundary condition for w_0 and Dirichlet boundary condition for u_0 are implemented. In this case the Newuman boundary condition $\partial_r w = 0$ is substituted directly instead of $w_{1/2,j+1/2}$ in discretized momentum equation.

3.2. Grid Generation

Due to the large gradient of solution near the sharp corner and walls, there is a necessity of using either a very fine uniform grid or applying a grid refinement near the mentioned regions. By considering the uniform grid a huge increase of cell numbers are required to resolve the existing scales which would be really expensive regarding computational time and resources. Therefore, it is more efficient to refine the grid only in regions where strong gradient are expected. To define a non-uniform grid we introduce two fundamental parameters namely the local stretching factor δ and the global stretching factor Λ for both r and z drirections. The local stretching factors δ_r and δ_z are defined as

$$\delta_r = \frac{\Delta r_{i+1}}{\Delta r_i}, \tag{3.10a}$$

$$\delta_z = \frac{\Delta z_{j+1}}{\Delta z_j}. \tag{3.10b}$$

where $\Delta r_{i+1} = r_{i+1} - r_i$, $\Delta r_i = r_i - r_{i-1}$, $\Delta z_{j+1} = z_{j+1} - z_j$ and $\Delta z_j = z_j - z_{j-1}$. In this study we applied uniformly stretched grid with constant local stretching factor $\delta = \delta_r = \delta_z = $ constant. The global stretching factors Λ_r and Λ_z are defined as

$$\Lambda_r = \frac{\Delta r_{max}}{\Delta r_{min}}, \tag{3.11a}$$

$$\Lambda_z = \frac{\Delta z_{max}}{\Delta z_{min}}. \tag{3.11b}$$

where $\Delta r_{max}(\Delta z_{max})$ is the maximum grid increment and $\Delta r_{min}(\Delta z_{min})$ shows the minimum grid increament in $r(z)$ direction. In general, for a moderate to large grid stretching, the range of a global streching factor Λ should be between 4 to 32 [100]. In the current project, the global stretching factors Λ_r and Λ_z are considered to be around 8 and 4 respectively. Central difference scheme were used to approximate the derivatives. Therefore, the accuracy of considered numerical approximation for derivatives is calculated by the expansion of Taylor series around r_i or z_j for the function f (see Eqn. (3.12)).

$$f'(r_i) = \frac{f(r_{i+1}) - f(r_{i-1})}{\Delta r_{i+1} - \Delta r_i} + \frac{f''(r_i)}{2!}(\Delta r_{i+1} - \Delta r_i) + \mathcal{O}(\Delta r^2) \tag{3.12}$$

As it is shown in Eqn. (3.12), the central difference $f(r_i)'' = [f(r_{i+1}) - f(r_{i-1})]/[(\Delta r_{i+1} - \Delta r_i)]$, would be second order accurate for the uniform grid ($\Delta r_{i+1} = \Delta r_i$). while the accuracy would be reduced to the first order for non-uniform grids ($\Delta r_{i+1} \neq \Delta r_i$). However, the accuracy could improve to the second order asymptotically if the grid do not stretch rapidly [34]. If the local grid stretching factor $\delta = \Delta r_{i+1}/\Delta r_i$ is not too far from the unity, the factor $(\Delta r_{i+1} - \Delta r_i) = \Delta r_i(\delta - 1)$ in the leading order error can then still be second order. Therefore, to have a second order accuracy asymptotically, the grid local stretching factor should not deviate more than 5% from the unity [100]. In the current project, the grid stretching factor considered to be $\delta = 1.03$ which would change the dimensions of two adjacent cells by 3%.

3.3. Basic-State

By discretizing equations (2.8a)–(2.8c) via finite volume method, a discrete non-linear system of equations for all the grid points (i, j) is achieved

$$L(x) \cdot x = \text{rhs} \tag{3.13}$$

where $x = (u_{0,0}, w_{0,0}, p_{0,0}, ..., p_{n_{r+1}, n_{z+1}})^{\mathrm{T}}$. Obtained system of algebraic equations (3.13) is solved with the help of Newton–Raphson method [83]. In this method, the residual of each iteration step is defined as

$$f(x^{(n)}) = L(x^{(n)}) \cdot x^{(n)} - \text{rhs} \tag{3.14}$$

where n is the number of iteration step. To obtain the basic flow x_0, the Newton's iteration should converge $f(x^{(n+1)}) \to 0$. The iteration is considered to be converged when the root mean square norm of the residual $\frac{\|f(x^{(n+1)})\|}{\sqrt{N}}$ is smaller than $\mathcal{O}(10^{-8})$. The root mean square norm of the residual is defined as the Euclidean norm which is scaled by the square root of the number of unknowns $\sqrt{N}$. Figure 3.2 shows the step by step procedure of solving Eqn. (3.14) by means of Newton–Raphson method. At the first stage, n = 0, a random vector $x^{(0)}$ is considered and the residual is calculated $f(x^{(0)}) = L(x^{(0)}) \cdot x^{(0)} - \text{rhs}$. Then the Jacobi matrix would be computed for $x^{(n)}$. Consequently, we solved the linear system $J(x^{(n)}).\delta x = -f(x^{(n)})$ directly by backslash operator ($\backslash$) in MATLAB to find the δx and obtain the new vector $x^{(n+1)}$. Then, the residual is calculated for the new vector $x^{(n+1)} = \delta x + x^{(n)}$. Finally, the root mean square (RMS) norm of the residual $\frac{\|f(x^{(n+1)})\|}{\sqrt{N}}$ is calculated. If RMS would be smaller than 10^{-8}, $x^{(n+1)}$ is considered as the solution vector, otherwise $x^{(n+1)}$ is approximated as an initial guess and all the iteration steps would be repeated.

In order to solve Eqn. (3.13) with Newton–Raphson method, the initial guess should be selected near the final solution, otherwise this method would diverge. Local convergencey is the biggest disadvantage of Newton's method. Therefore, in order to improve the convergency, the classical continuation method in which the converged solution of the old Reynolds number Re serves as an initial guess for the new Reynolds number is applied [44]. This method would be efficient only if both old and new Reynolds numbers have the same solution path [44].The continuation becomes difficult when approaching a turning or bifurication point. Therefore, an arclength continuation method [51] is also implemented. For this purpose, additional variable ζ representing the direction of continuation is introduced. We define an arclength Δs indicating the distance between the unknown (x, ζ) and known $(x^{\dagger}, \zeta^{\dagger})$ solutions as

$$\Delta s^2 = \| x - x^{\dagger} \|_2^2 + (\zeta - \zeta^{\dagger})^2 \tag{3.15}$$

By means of arclength definition (see Eqn. 3.15), $f(x, \zeta)$ extends to $F(x, \zeta) := (f(x, \zeta), g(x, \zeta))^{\mathrm{T}}$ where $g(x, \zeta)$ defined by arclength constraint

$$g(x, \zeta) := \| x - x^{\dagger} \|_2^2 + (\zeta - \zeta^{\dagger})^2 - \Delta s^2 \tag{3.16}$$

Accordingly, the linear equations extends to

$$\begin{pmatrix} \frac{\partial f_i}{\partial x_j} & \frac{\partial f_i}{\partial \zeta} \\ \frac{\partial g}{\partial x_j} & \frac{\partial g}{\partial \zeta} \end{pmatrix}^{(n)} \cdot \begin{pmatrix} \Delta x \\ \Delta \zeta \end{pmatrix} = - \begin{pmatrix} f_i \\ g \end{pmatrix}^{(n)} \tag{3.17}$$

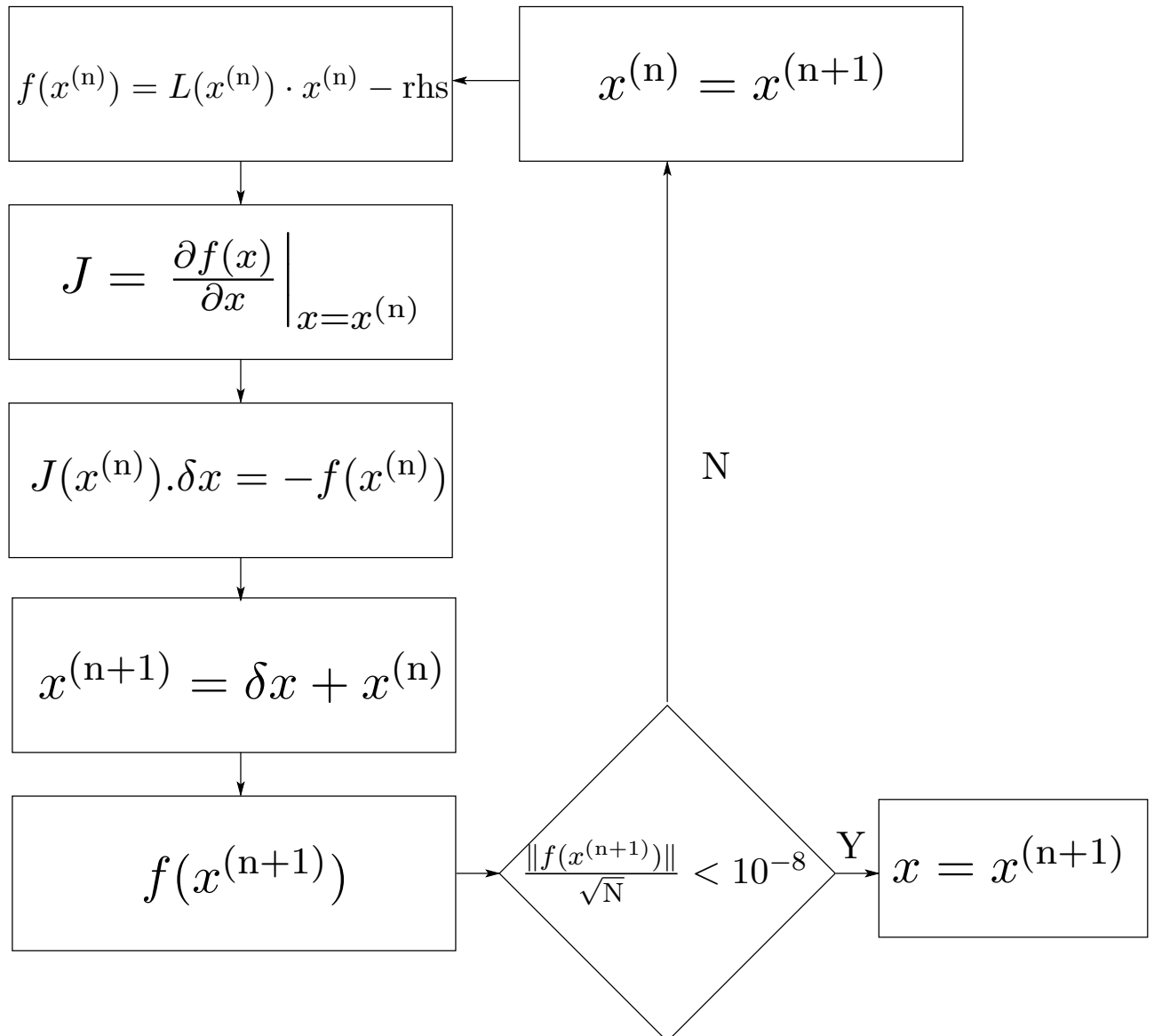where the difference between two consequent equations are shown by $\Delta x = x^{(n+1)} - x^{(n)}$ and

Figure 3.2.: Newton–Raphson method algorithm

$\Delta\zeta = \zeta^{(n+1)} - \zeta^{(n)}$. In order to obtain a good start value on the solution branch $f(x,\zeta) = 0$ from the previous known solution point $(x^\dagger, \zeta^\dagger)$ and the predictor step length Δs, a tangantical vector $T = (t, t^\zeta)$ of the function f at the known solution $(x^\dagger, \zeta^\dagger)$ is calculated as

$$t\frac{\partial f_i}{\partial x_j} + t^\zeta \frac{\partial f_i}{\partial \zeta} = 0 \tag{3.18}$$

where the tangent vector $T = (t, t^\zeta)$ is uniquely determined by defining the length of the tangantical vector to an arbitary value, e.g. $T_1 = 1$. Since the predictor step length is considered to be Δs in T direction, we normalized the tangantical vector T and determined the initial point for the Newton–Raphson iteration as

$$\begin{pmatrix} x^{(0)} \\ \zeta^{(0)} \end{pmatrix} = \begin{pmatrix} x^\dagger \\ \zeta^\dagger \end{pmatrix} + \begin{pmatrix} \frac{t}{\|t\|_2} \\ \frac{t^\zeta}{\|t^\zeta\|_2} \end{pmatrix} \Delta s \tag{3.19}$$

In addition, to globalize the Newton–Raphson method, the polynomial line search strategy which is suggested by Kelley [52] is implemented. This method activated when the residual of the new vector is bigger than the residual of the previous one $f(x^{(n+1)}) > f(x^{(n)})$. Therefore, 10 different step length α_i would be considered in the range $\alpha_i \in]0,1[$. The new vectors with all 10 discrete step lengths $x_i^{(n+1)} = x^{(n)} + \alpha_i \delta x$ and their related residuals $f(x_i^{(n+1)})$ are calculated. In order to obtain the most efficient value for the step lenght α_{eff}, the three smallest residuals have been chosen and a parabola is fitted to these residuals. In other words, by checking different step size $\alpha_i \in]0,1[$, α_{eff} is calculated in order to estimate the best new vector $x^{(n+1)}$ which is accompanied by the least residual $f(x^{(n+1)})$ among the others. This new vector $x_i^{(n+1)} = x^{(n)} + \alpha_{\text{eff}}\delta x$ could serve either as the solution vector or the best initial guess for the next iteration depending on its RMS.

3.4. Stability-Analysis

The same discretization scheme as the basic state is applied to discretize the obtained differential equations of perturbation amplitudes (2.18a)–(2.18d). Defining the boundary conditions for (2.18a)–(2.18d) yields to a complex generalized eigenvalue problem

$$A \cdot \hat{x} = \gamma B \cdot \hat{x} \tag{3.20}$$

where γ is the temporal decay rate, A and B represent operators of the set of linear equations and $\hat{x}^T = (\hat{u}, \hat{w}, \hat{v}, \hat{p})$ comprises of the perturbation amplitudes. In order to save memory, the complex eigenvalue problem is transformed to the real one by applying the transformation $i\hat{v} = \bar{v}$ [97]. To solve the eigenvalue problem an Implicitly Restarted Arnoldi Method is applied which is provided by the ARPACK software library [62]. It is used with the eigs command in MATLAB. The system under consideration (3.20) has an infinite number of degrees of freedom. In order

to solve it, we reduce the number of degrees of freedom to κ (Krylov subspace dimension) by an appropriate discretization. The dimension of the Krylov subspace used is $\kappa = 250$. The most dangerous eigenvalues (decay rates) have the smallest real part. Since B is singular due to the assumption of incompressibility, the most dangerous eigenvalues cannot be calculated by the Arnoldi Method alone. Therefore, a shift–invert transformation with the zero shift is required.

$$(A - \delta_1 B) \cdot \hat{x} = (\gamma - \delta_1) B \cdot \hat{x} \tag{3.21}$$

$$\frac{(A - \delta_1 B)}{(\gamma - \delta_1)} \cdot \hat{x} = B \cdot \hat{x} \tag{3.22}$$

$$\Rightarrow B \cdot \hat{x} = \frac{1}{\gamma} A \cdot \hat{x} \quad \text{when} \quad \delta_1 = 0 \tag{3.23}$$

the shift–invert transformation maps the irrelevant eigenvalues to zero and it finds the eigenvalues which are close to the shift $\delta_1 = 0$ [9]. This transformation is already implemented in the eigs command.

To check that no eigenvalues with smaller real parts are missed a Cayley transformation was implemented as an additional verification step. The eigenvector corresponding to the most dangerous eigenvalue obtained from the shift–invert step is then selected as the starting vector for the Cayley transformation. The Cayley transformation is defined as

$$(A - \delta_2 B) \cdot \hat{x} = \frac{\gamma - \delta_2}{\gamma - \delta_1}(A - \delta_1 B) \cdot \hat{x} \tag{3.24}$$

Two Cayley parameters δ_1 and δ_2 are calculated from the most dangerous eigenvalues which obtained from the shift–invert transformation (see [24], [69], [61] and [92]). We apply the Meerbergen's method [69] of finding δ_1 and δ_2. Therefore, to calculate r eigenvelues by the Cayley transformation, $r + 1$ most dangerous eigenvalues which were computed by restarted Arnoldi algorithm with shift–invert transformation are considered. Then, the real part of mentioned eigenvalues are sorted in an ascending order $[\Re(\gamma_1), \Re(\gamma_2), ..., \Re(\gamma_n), \Re(\gamma_{n+1})]$. Finally, the following equations are solved to calculate two free parameters of Cayley transformation

$$\frac{\mid \Re(\gamma_1) - \delta_2 \mid}{\mid \Re(\gamma_1) - \delta_1 \mid} = \rho_{\text{user}}, \tag{3.25a}$$

$$\delta_1 + \delta_2 = 2\gamma_{\text{ref}} \tag{3.25b}$$

where $\gamma_{\text{ref}} = \Re(\gamma_{r+1})$ and ρ_{user} is a empirical parameter which is prescribe by user. Typical values for ρ_{user} are 1.2 and 1.5 [69]. In this study, for the calculation of δ_1 and δ_2, the parameters $r = 6$ and $\rho_{\text{user}} = 1.2$ are selected. With Cayley transformation, most of the eigenvalues are mapped inside a unit circle. The eigenvalues which are far from both δ_1 and δ_2 are mapped to 1.

To find the neutral curves $\text{Re}_n(m, \Gamma, \eta^{\text{out}})$, minimized with respect to k, for each investigated wave number m, a very small initial Reynolds number Re_{init} (e.g. $\text{Re}_{\text{init}} = 5$) corresponding

to a stable flow condition ($\sigma > 0$) is selected for the first investigated case of each curve and the most dangerous eigenvalue is computed. The Reynolds number is increased until the sign of σ changes meaning that at least there is one root in the interval of investigated Reynolds numbers. Therefore, the neutral mode can be found by a single root finding method. Once the first neutral Reynolds number is found, natural continuation method is used for variation of Γ and η^{out} starting from a known value of Re_{n} meaning that the known Re_{n} is used as the initial Reynolds number Re_{init} for the consecutive parameter set. Depending on the sign of σ the Reynolds number either increased or decreased until the sign of σ changes. For each new parameter value the neutral Reynolds number is then found by means of a bisected direct quadratic regula falsi (BDQRF) method [40]. This method is a combination of regula falsi, bisection and direct quadratic interpolation. The regula falsi method needs many iterations to converge to the root [18]. Therefore, within each iteration, a bisection method can be applied to divide the investigated intervals in half [18]. Bisection method converges to the root linearly. Therefore, the rate of the convergency can be improved by fitting the quadratic polynomial to the three existing points [40]. Bisected direct quadratic regula falsi method is a very powerful method which is robust and converge faster than other types of regula falsi root finding algorithms such as Brent's method [18]. The procedure of root finding in the applied BDQRF method is shown in Table 3.4. In this algorithm the initial Reynolds number is shown by Re_{init} and the constant number C represent a relative increment/decrement in the Re. By computing all the neutral Reynolds numbers for the investigated parameter range, neutral curves are obtained. The critical Reynolds number Re_c is then obtained as the envelope of all neutral curves.

Finding the root by bisected direct quadratic regula falsi (BDQRF) algorithm

$x_1 = \text{Re}_\text{init}; \qquad y_1 = f(x_1)$

$x_2 = x_1 \times C; \qquad y_2 = f(x_2) \qquad C = Cons.$

while $y_1 \times y_2 > 0$

$\quad x_1 = x_2; \qquad y_1 = y_2; \qquad x_2 = x_1 \times C; \qquad y_2 = f(x_2)$

end while

Find the root x which is between x_1 and x_2 by BDQRF method

if $(y_1 < 0)$

$\quad x_\text{down} = x_1; \qquad y_\text{down} = y_1$

$\quad x_\text{up} = x_2; \qquad y_\text{up} = y_2$

else

$\quad x_\text{up} = x_1; \qquad y_\text{up} = y_1$

$\quad x_\text{down} = x_2; \qquad y_\text{down} = y_2$

end

while $(\mid y \mid > tol)$

$\quad D = (x_\text{up} - x_\text{down})/2;$

$\quad x_\text{m} = (x_\text{up} + x_\text{down})/2;$

$\quad y_\text{m} = f(x_\text{m});$

$\quad a = (y_\text{up} + y_\text{down} - 2y_\text{m})/2D^2;$

$\quad b = (y_\text{up} - y_\text{down})/2D;$

$\quad x = x_\text{m} - 2y_\text{m}/\left[b\left(1 + \sqrt{1 - 4ay_\text{m}/b^2}\right)\right];$

$x_\text{last} = x;$

$y = f(x);$

if $y > 0$

$\quad y_\text{up} = y; \qquad x_\text{up} = x;$

$\quad$ if $(y_\text{m} < 0)$

$\quad\quad y_\text{down} = y_\text{m}; \qquad x_\text{down} = x_\text{m};$

$\quad$ end if

else

$\quad y_\text{down} = y; \qquad x_\text{down} = x;$

$\quad$ if $(y_\text{m} > 0)$

$\quad\quad y_{up} = y_\text{m}; \qquad x_\text{up} = x_\text{m};$

$\quad$ end if

end if

end while

4. Verification of the Numerical Code

To assure that the results presented in chapter 5 are correct, applied numerical code should be verified. Cylindrical coordinates (r, z, ϕ) are used to formulate the configurations of interest in this study. To the best of author's knowledge, for both set-ups, there are barely any experimental and numerical data for the characteristics of the basic flow and its two and three-dimensional stability to compare with. However, there are numerous studies on the flow behaviour and its linear stability for (a) the plane flow over backward-facing step in cartesian coordinates ([6], [25], [10], [16], [31] and [60]) and (b) the half zone problem of the liquid bridge ([104], [64], and [76]) in the cylindrical (r, z, ϕ) coordinates, which are employed as the verification of our numerical code in this chapter. Considering the backward-facing step in an annular-pipe, backward-facing step problem for plane-channel flow is recovered in the limit of unit outlet radius ratio $\eta^{\text{out}} \to 1$. Therefore, this limit is used as the first verification of our numerical code for the basic state. Even though both geometry and boundary conditions of the liquid bridge are different from the considered cases in this study, however in order to check and verify the basic state and three-dimensional stability analysis in cylindrical coordinate system (r, z, ϕ), the half zone model of the liquid bridge in the limit of the zero Prandtl number is considered and the obtained results are compared with the existing ones in the literature.

4.1. Verification of the basic state

Two cases are considered to verify the developed finite volume solver for Navier–Stokes and continuity equations (2.8a)–(2.8c) for the basic flow. Considering the flow over backward-facing step in an annular pipe (see Fig. 2.1), the backward-facing-step problem for plane-channel flow should be recovered in the limit of unit outlet radius ratio $\eta^{\text{out}} \to 1$. Therefore, as the first check of the applied numerical code for the basic-state, flow over backward-facing step in an annular pipe (see Fig. 2.1) with the outlet radius ratio $\eta^{\text{out}} = 0.998$ and radial expansion ratio $\Gamma = 0.5$ is considered and the z location of the separation and reattachment points on the inner and outer cylinder are obtained and compared to the results of Barkley et al. [10]. As second test of our finite volume solver in a cylindrical coordinate system, a half zone model of the liquid bridge in the limit of zero Prandtl number $\text{Pr} = 0$ is considered. The basic-state is obtained and stream function minimum Ψ for different Reynolds numbers Re are calculated and compared to the existing results in the literature ([65] and [87]).

4.1.1. Verification of the results with the backward-facing step in plane-channel flows

To verify the present code for the basic flow, we consider the limit of unit outlet radius ratio $\eta^{\mathrm{out}} \to 1$, for which reference data are available. Therefore, we set $\eta^{\mathrm{out}} = R_{\mathrm{i}}^{\mathrm{out}}/R_{\mathrm{o}} = 0.998$.
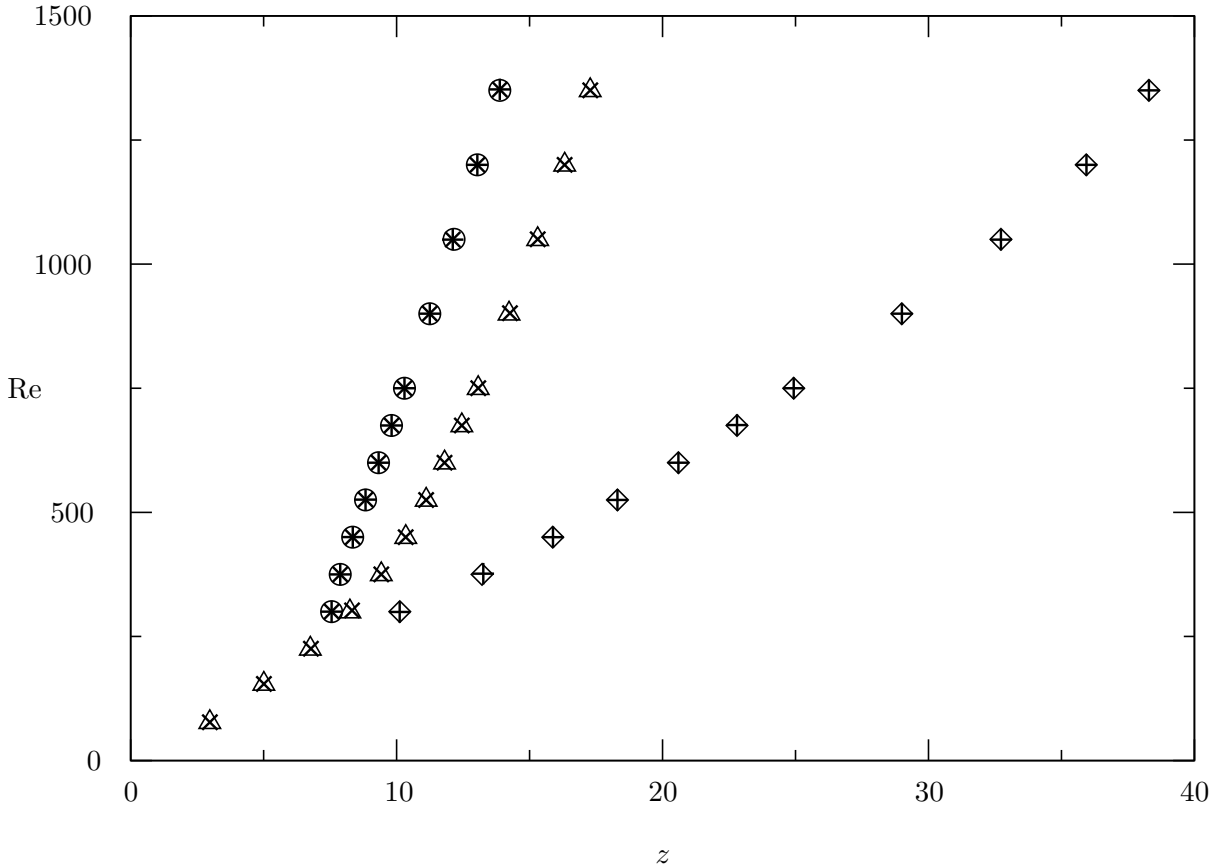

Figure 4.1.: Separation and reattachment points of the flow behind the backward-facing step (located at $z = 0$) for $\Gamma = 0.5$ as a function of the Reynolds number. Current results are compared with the data of Barkley et al. [10] for $\eta^{\mathrm{out}} = 1$. Separation point on the outer cylinder $\circ$: $\eta^{\mathrm{out}} = 0.998$, $*$: Barkley et al. [10], reattachment point on the outer cylinder $\diamond$: $\eta^{\mathrm{out}} = 0.998$, $+$: Barkley et al. [10], reattachment point on the inner cylinder $\triangle$: $\eta^{\mathrm{out}} = 0.998$, $\times$: Barkley et al. [10]

For the sake of consistency, the same computational domain as Barkley et al. [10] are considered. Therefore, we set the radial expansion ratio $\Gamma = 0.5$ and the inflow length equal to the non-dimensional step height $L_{\mathrm{i}} = h_{\mathrm{s}}$ as our computational domain. At the inlet ($z = -L_{\mathrm{i}}$, $r \in [R_{\mathrm{i}}^{\mathrm{in}}; R_{\mathrm{o}}]$), the annular Poiseille flow (2.5) is imposed. On all walls and along the step, no-slip boundary condition $u_0 = w_0 = 0$ are implemented. At the outlet, standard outflow boundary condition for velocity and pressure is employed (see [37] and [102]). Finally, the locations of the separation and reattachment points on the inner and the outer cylinder are obtained and compared with the results of Barkley et al. [10] in Fig. 4.1. Upon an increase of the Reynolds number the lengths of the recirculation zones behind the step grow on both, the inner cylin-

der R_i^{out} and the outer cylinder R_o. Furthermore, the separation and reattachment points are shifted downstream as Re increased. The relative deviation between Barkley et al. [10] results and the obtained results is less than $\varepsilon^{\text{rel}} \leqslant 3.3056e - 04$ showing that the results are in very good agreement.

4.1.2. Verification of the results with the half zone model of liquid bridge

As a second verification we consider a benchmark in cylindrical geometry (r, z, ϕ): an incompressible Newtonian fluid in a liquid bridge. A sketch of the liquid bridge with the length d and radius R is shown in Fig. 4.2. The cylindrical disks with the radius R are considered at the constant temperatures $T_0 - \Delta T/2$ and $T_0 + \Delta T/2$ respectively. T_0 is the mean temperature. In general, the driving force is due to the surface tension gradient which is generated by the gradient of the temperature

$$\sigma = \sigma_0 - \gamma(T - T_0) \tag{4.1}$$

where $\gamma = \partial\sigma/\partial t|_{T=T0}$ and σ_0 represents the surface tension at the mean temperature T_0.
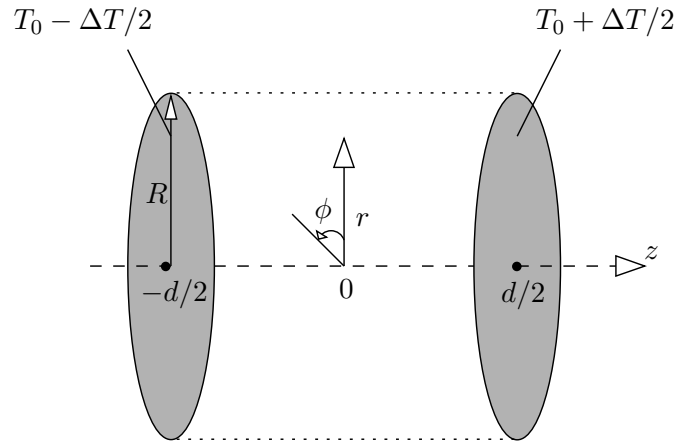

Figure 4.2.: Sketch of the liquid bridge. dashed line represents the axis and dotted lines indicates the free surface.

To obtain the basic flow in the liquid bridge, axisymmetric Navier–Stokes, continuity and energy equations are considered. The following viscous scaling is applied to non-dimensionalize the equations

Variable	Length	Velocity	Pressure	Time	Temperature
Scaling	d	ν/d	$\rho\nu^2/d^2$	d^2/ν	ΔT

Table 4.1.: Viscous scaling used to non-dimensionalize equations

where ρ and ν show the density and kinematic viscosity of the fluid respectively. By applying the viscous scaling (see Table. 4.1), non-dimensional Navier–Stokes, continuity and energy

equations reads

$$\partial_t \boldsymbol{U} + \nabla \cdot (\boldsymbol{U}\boldsymbol{U}) = -\nabla P + \nabla^2 \boldsymbol{U}, \tag{4.2a}$$

$$\nabla \cdot \boldsymbol{U} = 0, \tag{4.2b}$$

$$\partial_t \Theta + U \cdot \nabla\Theta = \frac{1}{\text{Pr}} \nabla^2 \Theta \tag{4.2c}$$

where the Prandtl number is defined as $\text{Pr} = \nu/\kappa$ and Θ is the deviation of dimensionless temperature from the pure conduction

$$\Theta = \frac{T - T_0}{\Delta T} - z \tag{4.3}$$

To check if the developed solver for the basic-state in cylindrical coordinate (r, z, ϕ) (Eqn. (2.8a)–(2.8c)) works properly for the internal flow, we consider the limit of zero Prandtl number $\text{Pr} = 0$ of the liquid bridge half zone model, for which reference data are available in the literature ([105], [76]). In this case, energy equation reduce to $\nabla^2\Theta = 0$. Therefore, the energy and momentum equations decoupled from each other. As is shown in Fig. 4.2, the origin of the considered cylindrical coordinate system is located on the axis of symmetry at the middle of the liquid bridge length $(z = d/2)$. This geometry is characterized with the non-dimentional aspect ratio $\Gamma = d/R$. As a representative example of grid generation for the half zone model of the liquid bridge, the computational mesh for $\Gamma = 1$ is shown in Fig. 4.3. In order to generate the mesh, double-sided grid refinement with the local stretching factor $\delta_r = \delta_z = 1.05$ which distributes using the hyperbolic tangent stretching function is employed (see details in [103]).
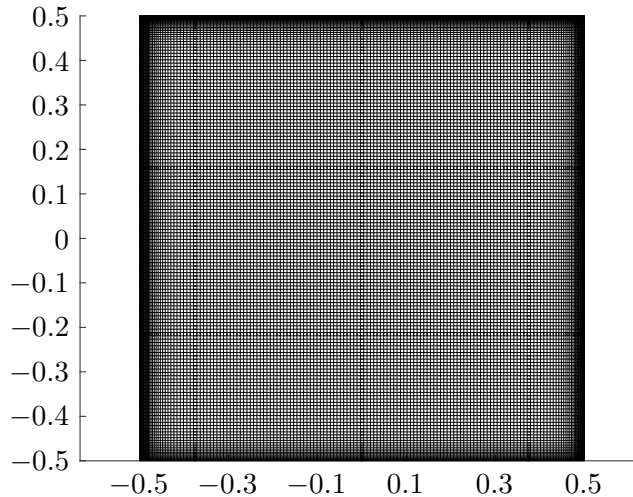

Figure 4.3.: Employed mesh for half zone problem with 156×156 computational nodes and streching factor $\delta_r = \delta_z = 1.05$.

The equations (Eqn. (4.2a)–(4.2c)) of the half zone model for $\text{Pr} = 0$ are equivalent to the

system of equations which we discretized and solved for the cases under investigation (Eqn. (2.8a)–(2.8c)) in cylindrical geometry (r, z, ϕ). Considering the half zone model of the liquid bridge, we implement the following boundary conditions in our numerical code,

No slip boundary condition is considered at the walls $(z = \pm d/2)$

$$u_0 = w_0 = 0 \tag{4.4}$$

Along the axis $(r = 0$ and $z \in [-d/2, d/2])$, the axisymmetric boundary condition is imposed

$$u_0 = \frac{\partial w_0}{\partial r} = 0 \tag{4.5}$$

On the free surface $(r = R$ and $z \in [-d/2, d/2])$, axial shear stress is considered to be constant, therefore

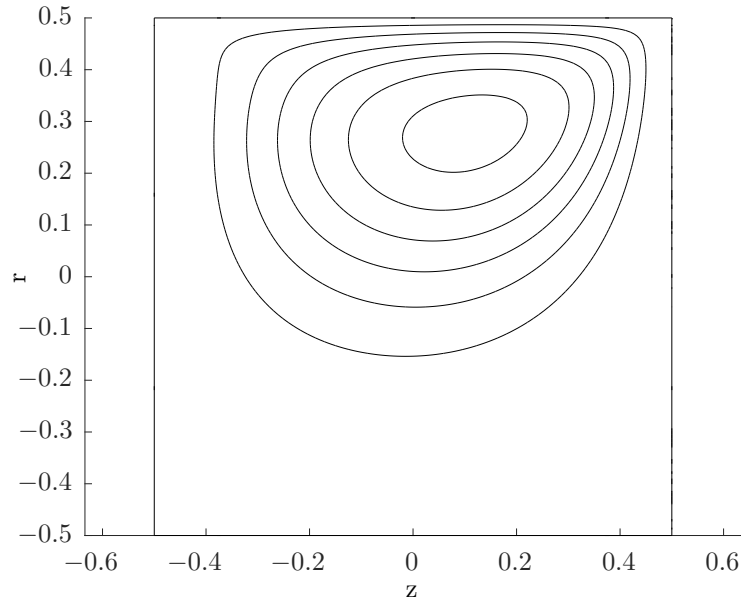$$\frac{\partial w_0}{\partial r} = \text{Re}, \tag{4.6a}$$

$$u_0 = 0 \tag{4.6b}$$

Figure 4.4.: Streamlines of the basic flow for the half zone model with the $\Gamma = 1$, Pr $= 0$ and Re $= 1500$

In order to test the existing finite volume solver for the basic-state in this study, the liquid bridge with $\Gamma = 1$ is considered for various Reynolds numbers. Figure 4.4 shows the obtained streamlines for the basic-flow with the Re $= 1500$.

The Stokes streamfunction Ψ in the cylindrical coordinate system calculated by $u_0 = -r^{-1}\partial_z \Psi$

and $w_0 = r^{-1}\partial_r\Psi$. Table 4.2 shows the computed minima of the Stokes streamfunction $\Psi_{\min}$ for a unit length-to-radius ratio in comparison with results of Romanò [87]. The results are in an excellent agreement with each other for different Reynolds numbers.

Re	1500	1600	1700	1800	1900	2000
present work	8.6426	8.5432	8.4515	8.3652	8.2843	8.2089
Romanò [87]	8.6431	8.5455	8.4534	8.3678	8.2868	8.2102

Table 4.2.: Comparison of stream function minima $\Psi_{\min}$ for $\Gamma = 1$ and $\mathrm{Pr} = 0$

Leypoldt et al. [65] performed an extensive study on the flow in cylindrical liquid bridge and calculated the stream function minimum $\Psi_{\min}$ for Re = 1000, $\Gamma = 1$ and very small Prandtl number Pr = 0.02 (Table. 4.3). Comparing obtained results with the one achieved by [65] for the very small Prandtl number, it is seen that, there is an acceptable agreement between our results and the ones in the literature.

1	Peresent study	Leypoldt et al. [65]
Pr	0	0.02
$\Psi_{\min}$	9.0927	8.93

Table 4.3.: Comparison of stream function minima $\Psi_{\min}$ for $\Gamma = 1$ and Re = 1000

4.2. Verification of the linear stability analysis

In this part, the grid convergence is checked and the developed numerical code for the two and three-dimensional linear stability analysis is verified. As the verification for two-dimensional stability analysis ($m = 0$), the critical mode for an annular pipe in the limit of the unit radius ratio ($\eta = R_\mathrm{i}/R_\mathrm{o} \to 1$) is calculated. We compared the results with the ones exists in the literature ([99], [78], and [60]) for the plane channel flow. In order to verify the applied solver for three-dimensional stability analysis, a half zone model of the liquid bridge with an aspect ratio $\Gamma = 1$ and non-deformable free surface in the limit of zero Prandtl number Pr = 0 (see Fig. 4.2) is considered. The critical Reynolds number Re$_c$ and oscillation frequency ω_c are calculated and compated to the results which obtained by Wanschura et al. [105] for very small Prandtl number Pr = 10^{-8}.

To check the implementation of boundary conditions for the perturbation on the axis of symmetry for $m = 1$ and $m = 2$, the critical Reynolds number Re_c for the thermocapillary liquid bridge with an aspect ratio $\Gamma = 2$ and non-deformable cylindrical free surface in the limit of zero Prandtl number Pr = 0 (see Fig. 4.2) are calculated for $m = 1$ and $m = 2$ and compared to the results which were obtained by Wanschura et al. [105] for the small Prandtl number Pr = 0.02. As an additional check, the perturbation flow in (r, ϕ) at the obtained critical modes are depicted and compared qualitatively with the existing data of the perturbation flow for these wave numbers in the literature ([22], [105] and [76]).

4.2.1. Grid convergence study

In this section the flow over annular backward-facing step with the radius ratio $\eta^{\text{out}} = 0.1$ and $\Gamma = 0.5$ is considered as a representative case for the grid convergence study. In order to estimate the accuracy of our neutral curves, the critical Reynolds number Re_c is considered as the representative quantity. Therefore, we measure the convergence of relative error (ε) defined as

$$\varepsilon = \frac{\text{Re}_c^{\text{a}} - \text{Re}_c^*}{\text{Re}_c^*} \tag{4.7}$$

where Re_c^{a} and Re_c^* denote the critical Reynold numbers corresponding to the investigated grid and to the highest resolution respectively. Since the exact critical Reynolds number is unknown, the critical Reynolds number associated to the highest resolution Re_c^* is used as reference in the relative error ε.

	N_{z}^{in}	N_{r}^{in}	$N_{\text{z}}^{\text{out}}$	$N_{\text{r}}^{\text{out}}$	N_{total}	N_{u}
1	94	40	539	80	46880	187520
2	141	60	809	120	105540	422160
3	188	80	1078	160	187520	750080
4	282	120	1617	240	421920	1687680
5	376	160	2156	320	750080	3000320
6	470	200	2695	400	1172000	4688000

Table 4.4.: The characteristic of the grids used for the convergence study.

In order to perform the grid convergence study, six different grids are considered (see Table 4.4) and the critical Reynolds number is calculated for each of the grids. The characteristics of all six grids applied is shown in Table 4.4. N_{z}^{in}, N_{r}^{in}, $N_{\text{z}}^{\text{out}}$, and $N_{\text{r}}^{\text{out}}$ represent the total number of finite volumes in the inlet and the outlet part of the annulus and in z and r directions, respectively. The total number of cells in (r, z) plane is shown by $N_{\text{total}} = N_{\text{z}}^{\text{in}} \times N_{\text{r}}^{\text{in}} + N_{\text{z}}^{\text{out}} \times N_{\text{r}}^{\text{out}}$ and the total number of unknowns demonstrated by N_{u}. It can be seen that the highest resolution employed in (r, z) plane is 1172000 finite volumes which corresponds to 4688000 unknowns. Therefore, the calculated critical Reynolds number for case 6 (Table 4.4) is considered as Re_c^*.

Figure 4.5 shows the relative error ε as a function of the square root of the total number of cells $\sqrt{N_{\text{total}}}$. The calculated relative error ε for each case is shown by open circles while the full line shows the power law fitting curve $\varepsilon = a(\sqrt{N_{\text{total}}})^b$ with $b = -2.47$. The asymptotic behavior with small errors of $O(10^{-7})$ signals grid convergence. For the parametric variations to be presented in the following we selected the grid $n = 5$ (see Table 4.4). It provides a relative error less than $\varepsilon < 10^{-7}$ at an acceptable computational cost. A similar grid convergence was found for all other outlet radius ratios η and step heights Γ investigated.
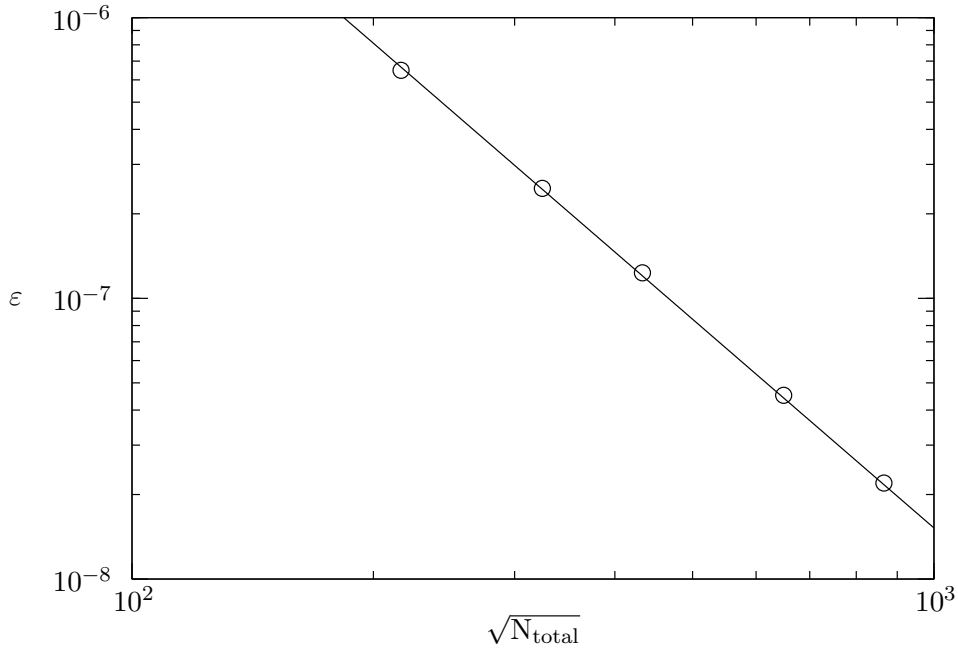
Figure 4.5.: The relative error ε as a function of the square root of the grid resolution $\sqrt{\mathrm{N_{total}}}$.

4.2.2. Verification of the results of linear stability analysis for two-dimensional perturbations $m = 0$

As a verification of the linear stability analysis for two-dimensional perturbations the critical Reynolds number for an annular pipe (see Fig. 4.6) with the radius ratio $\eta = R_\mathrm{i}/R_\mathrm{o} \to 1$ is calculated. This limit corresponds to plane channel flow. To that end, an annular pipe with the radius ratio $\eta = 0.99998$ which is very close to the limit $\eta = 1$ corresponding to plane channel flow, the height $H = R_\mathrm{o} - R_\mathrm{i} = 2$ and the following boundary conditions are considered.

Periodic boundary conditions in streamwise direction z are implemented.

$$\boldsymbol{u}_0(r, z = 0) = \boldsymbol{u}_0(r, z = L) \tag{4.8}$$

No-slip boundary condition is applied for the walls ($r = R_\mathrm{i}$, $r = R_\mathrm{o}$ and $z \in [0, L]$)

$$u_0 = w_0 = 0 \tag{4.9}$$

The linear perturbation equations can be solved by normal mode ansatz

$$[\tilde{u}, \tilde{w}, \tilde{p}]^\mathrm{T} = [\hat{u}, \hat{w}, \hat{p}]^\mathrm{T}(r, z)e^{-\gamma t} + \mathrm{c.c.}, \tag{4.10}$$

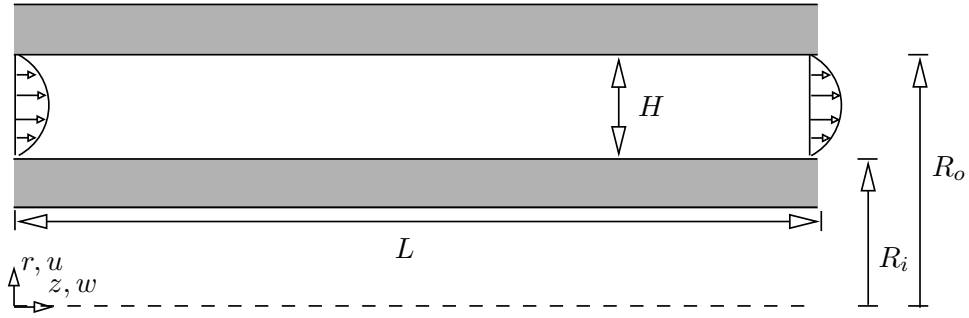where $\gamma = \sigma + i\omega$ is the complex temporal decay rate which comprises of the real decay rate

Figure 4.6.: sketch of the annular pipe.

σ and oscillation frequancy ω. We have found the axisymmetric instability is oscillatory and corresponds to a Tollmien–Schlichting wave which becomes unstable at $\mathrm{Re}_c = 5779$ (see Fig. 4.7). The critical Reynolds number, oscillation frequency $\omega_c = 0.269$ and wave number $k_c = 1.021$, corresponding to the wavelength $\lambda_c = 2\pi/k_c$, compare very well with literature results for the linear stability of plane channel flow [99, 78, 60]).

The streamlines and the perturbation flow of the critical mode ($\mathrm{Re}_c = 5779$, $\omega_c = 0.269$, $k_c = 1.021$ and $L_c = 2\pi/k_c$) are shown in Fig. 4.7(a) while Fig. 4.7(b) depicts the integral of the perturbation components $\tilde{u}, \tilde{w}, \tilde{p}$ up to the half of the annular height $H/2 = 1$, as a function of z. As it is shown, $\tilde{u}$ is symmetric while $\tilde{w}$ and $\tilde{p}$ are anti-symmetric with respect to π/k_c (black dotted line in Fig. 4.7(b)). By comparing the 4.7(b) with the obtained curves by Lanzerstorfer [60] for the plane channel flow, excellent agreement have been found.

4.2.3. Verification of the results of linear stability analysis for three-dimensional perturbations ($m = 1$ and 2)

In order to verify our developed numerical solver for the three-dimensional stability analysis of curved geometries, we consider a the axisymmetric toroidal vortex flow in the cylindrical thermocapillary liquid bridge with a non-deformable cylindrical free surface (see Fig. 4.2) and for the aspect ratio (length-to-radius ratio) $\Gamma = 1$ with the zero Prandtl number $\mathrm{Pr} = 0$.

	Pr	Re$_c$	ω_c
present work	0	1789.93	0
Wanschura et al. [105]	10^{-8}	1793	0

Table 4.5.: Comparison of critical Reynolds number and oscillation frequency for $\Gamma = 1$ and $m = 2$.

Table 4.5 shows the critical Reynolds number Re$_c$ and oscillation frequency ω_c for a unit aspect ratio ($\Gamma = 1$) and an azimuthal wave number $m = 2$. it can be seen that the flow becomes unstable to a stationary mode ($\Omega_c = 0$) with $m = 2$ at Re $= 1789.93$. These critical parameters are in very good agreement with the result of Wanschura et al. [105] who obtained $\omega_c = 0$, $m = 2$ and Re$_c = 1793$ for a thermal variant of the problem, but for extremely small Prandtl number $\mathrm{Pr} = 10^{-8}$ which is very close to the inertial problem ($\mathrm{Pr} \to 0$) considered here.
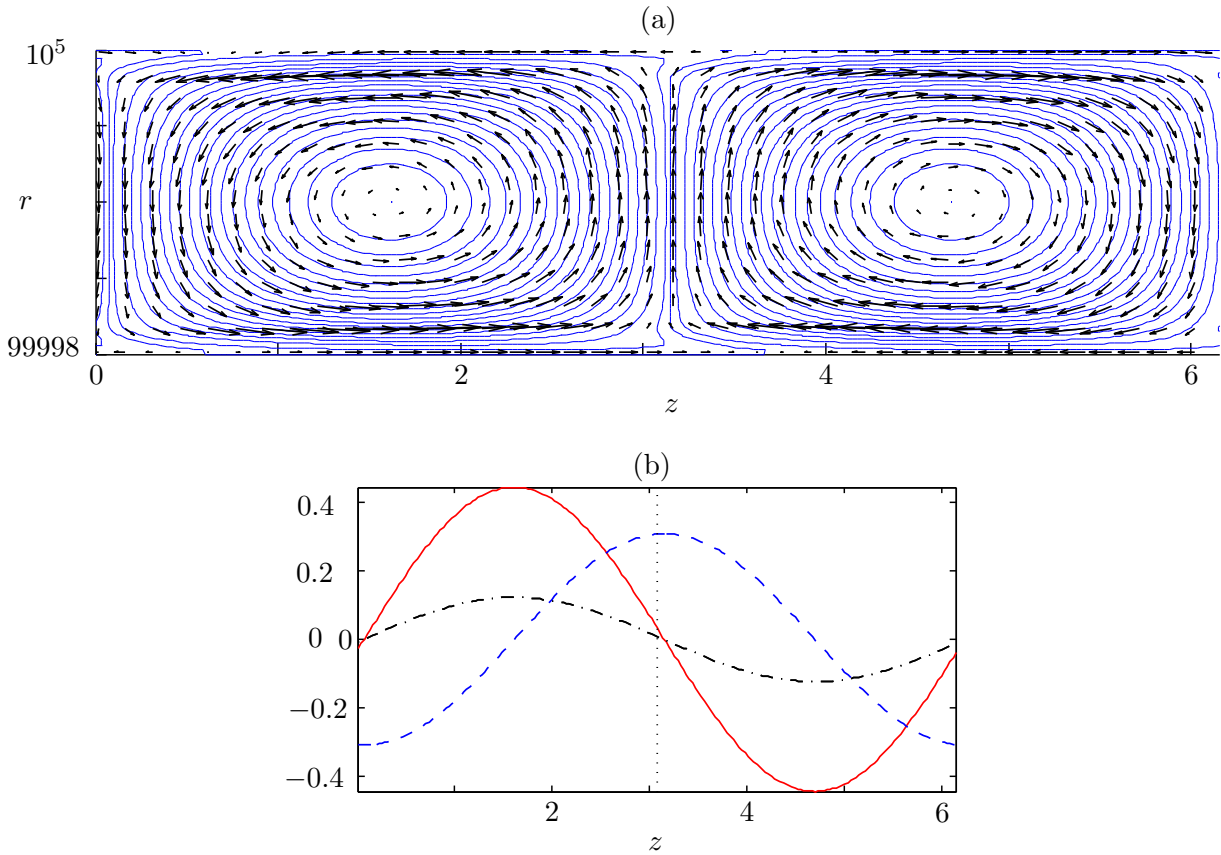
Figure 4.7.: (a) Streamlines of the critical mode (blue solid lines) and perturbation flow (black arrows) at critical conditions. (b) The integral of the perturbation components up to the half of the annular height $H/2$, as a function of streamwise direction z. The red solid, the black dashed dotted and the blue dashed curves show the integral of the $\tilde{w}$, $\tilde{p}$ and $\tilde{u}$ up to the half of the channel respectively.

	Pr	Re$_c$	m
present work	0	1599.5	1
Wanschura et al. [105]	0.02	1689	1
present work	0	3431.5	2
Wanschura et al. [105]	0.02	3565	2

Table 4.6.: Comparison of critical Reynolds numbers for $\Gamma = 2$ for different azimuthal wave numbers m.

As it is shown by Eqn. (2.21), the boundary conditions of the perturbations on the axis of symmetry are depending on the considered azimuthal wave number m. Therefore, to check the implementation of the boundary conditions of perturbations along the axis, for different wave numbers m, the critical Reynolds numbers Re_c for the aspect ratio ($\Gamma = 2$) and azimuthal wave numbers $m = 1$ and $m = 2$ are calculated and compared with Wanschura et al. [105] results for small Prandtl number Pr $= 0.02$ (see Table. 4.6). As it is shown, the flow becomes unstable to

a mode with $m = 1$ and $m = 2$ at Re = 1599.5 and Re = 3431.5 respectively. Obtained critical Reynolds numbers are in very good agreement with the result of Wanschura et al. [105] for the small Prandtl number Pr = 0.02 who obtained $\text{Re}_c = 1689$ and $\text{Re}_c = 3565$ for $m = 1$ and $m = 2$ respectively.
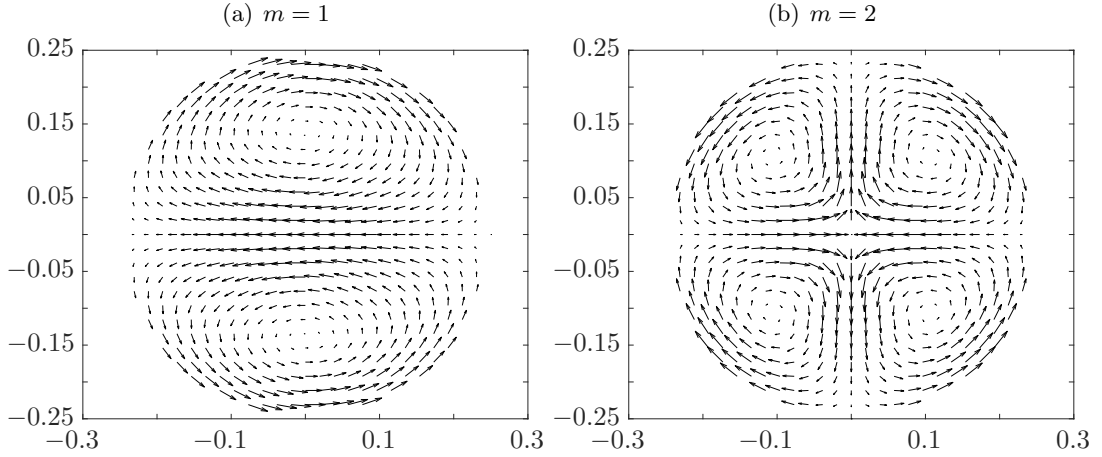

(a) $m = 1$ (b) $m = 2$

Figure 4.8.: Perturbation flow in (r, ϕ) at the critical mode for aspect ratio $\Gamma = 2$ and Prandtl number Pr = 0 for (a) wave number $m = 1$ and (b) $m = 2$.

Figure 4.8 shows the perturbation flow in (r, ϕ) direction at the critical mode for (a) wave number $m = 1$ and (b) $m = 2$. By comparing the existing numerical data ([22], [105] and [76]) with the obtained results, we can conclude that the boundary conditions of the perturbations amplitude for $m = 1$ and $m = 2$ implemented correctly along the axis.

4.3. Independence study for the inlet/outlet lenghts

In this section, we found the limit in which the inlet and outlet lengths of the annular pipe have a negligible influence on the flow characterisitcs and stability boundary. For this purpose, the recirculation length at Re = 800 and the critical Reynolds number Re_c are considered as the representative quantities.

As it is shown in Table 4.7, the recirculation length at Re = 800 and critical Reynolds number Re_c are computed for different expansion ratios and outlet radius ratios and various inlet lenghts $L_i = 5$, 10, 15 and 20 while the outlet length is $L_o = 100$. It can be seen that for the inlet lengths equal or larger than $L_i \geqslant 10$ the results are independent of this lenght.

To have negligible dependence on the finite lenght of the pipe, outlet should locate very far downstream of the step. To obtain the outlet length independent results, the inlet length kept constant L_i and the recirculation length at Re = 800 and critical Reynolds number Re_c is calculated for the outlet lenghts $L_o = 40$, 60, 80 and 100 and different expansion ratios Γ and outlet radius ratios η^{out} (see Table 4.8). It can be seen that for $L_o \geqslant 80$, the results are independent of the outlet length. Therefore, in this study, we select $L_i = 10$ and $L_o = 80$ as the inlet and outlet lengths respectively.

L_{i}	5	10	15	20
$\eta^{\mathrm{out}} = 0.1,$ $\Gamma = 0.25,$ $L_{\mathrm{o}} = 100$				
Recirculation length at Re = 800	35.9882	37.0290	37.0290	37.0290
Re_c	131.6389	126.7841	126.7841	126.7841
$\eta^{\mathrm{out}} = 0.1,$ $\Gamma = 0.5,$ $L_{\mathrm{o}} = 100$				
Recirculation length at Re = 800	24.9825	28.8246	28.8246	28.8246
Re_c	66.0827	60.4998	60.4998	60.4998
$\eta^{\mathrm{out}} = 0.1,$ $\Gamma = 0.75,$ $L_{\mathrm{o}} = 100$				
Recirculation length at Re = 800	14.9429	15.8942	15.8942	15.8942
Re_c	61.4257	57.9763	57.9763	57.9763
$\eta^{\mathrm{out}} = 0.3,$ $\Gamma = 0.5,$ $L_{\mathrm{o}} = 100$				
Recirculation length at Re = 800	24.6871	27.8217	27.8217	27.8217
Re_c	299.9247	283.9432	283.9432	283.9432
$\eta^{\mathrm{out}} = 0.5,$ $\Gamma = 0.5,$ $L_{\mathrm{o}} = 100$				
Recirculation length at Re = 800	26.2309	26.4402	26.4402	26.4402
Re_c	311.9281	311.4028	311.4028	311.4028

Table 4.7.: Recirlulation lenght at the outer cylinder and the critical Reynolds number Re_c as a function of the inlet length L_{i}.

L_{o}	40	60	80	100
$\eta^{\mathrm{out}} = 0.1,$ $\Gamma = 0.25,$ $L_{\mathrm{i}} = 10$				
Recirculation length at Re = 800	30.0651	35.1972	37.0290	37.0290
Re_c	145.281	129.8461	126.7841	126.7841
$\eta^{\mathrm{out}} = 0.1,$ $\Gamma = 0.5,$ $L_{\mathrm{i}} = 10$				
Recirculation length at Re = 800	27.20	28.8246	28.8247	28.8246
Re_c	69.0064	60.4998	60.4998	60.4998
$\eta^{\mathrm{out}} = 0.1,$ $\Gamma = 0.75,$ $L_{\mathrm{i}} = 10$				
Recirculation length at Re = 800	15.9142	15.8942	15.8942	15.8942
Re_c	56.7829	57.9763	57.9763	57.9763
$\eta^{\mathrm{out}} = 0.3,$ $\Gamma = 0.5,$ $L_{\mathrm{i}} = 10$				
Recirculation length at Re = 800	21.0011	25.6437	27.8217	27.8217
Re_c	312.5282	293.82	283.94	283.94
$\eta^{\mathrm{out}} = 0.5,$ $\Gamma = 0.5,$ $L_{\mathrm{i}} = 10$				
Recirculation length at Re = 800	25.8971	26.4402	26.4402	26.4402
Re_c	315.6392	311.4028	311.4028	311.4028

Table 4.8.: Recirlulation lenght at the outer cylinder and the critical Reynolds number Re_c as a function of the outlet length L_{o}.

5. Results and Discussion

This chapter is divided into two main parts. In the first part, the characteristics of the basic flow for both set-ups are described, and the effect of different control parameters on the flow behaviour is investigated and discussed. In the second part of this chapter, the critical modes as a function of different control parameters are obtained for the considered cases and the instability mechanisms are described by performing an *a posteriori* energy analysis.

5.1. Basic-state

At the first part of this section, we present the general description of the two-dimensional steady state flow field as a function of (a) outlet radius ratio η^{out} and (b) radial expansion ratio Γ, for the flow over backward-facing step in an annular pipe. In the second part, the charactristics of two-dimensional annular flow expansion into the simple pipe as a function of Reynolds number Re and expansion ratio Γ are addressed.

5.1.1. Flow over backward-facing step in an annular pipe

Variation of the outlet radius ratio η^{out} for $\Gamma = 0.5$

In order to have a better understanding of the similarities and differences of the steady axisymmetric annular flow over radially inward backward-facing step and the flow over a backward-facing step in plane channel, the effect of outlet radius ratio η^{out} on the flow behaviour is investigated. Backward-facing step in a plane-channel problem is recovered in the limit of radius ratio $\eta^{\text{out}} \rightarrow 1$. Considering a constant expansion ratio $\Gamma = 0.5$ and Reynolds number (Re = 800), the cylindrical effect becomes stronger by decreasing the outlet radius ratio η^{out}. Therefore, the basic flow for the outlet radius ratio in the range $\eta^{\text{out}} \in [0, 1[$ is calculated.

Figure 5.1 shows the streamlines for four different outlet redius ratios $\eta^{\text{out}} = 0.1$, 0.3, 0.5 and 0.998 at Re = 800. Since considered geometry is very long and slender, for a better visualization, we only showed the streamlines in part of the annular pipe where two reciculation zone behind the step exist. It can be seen that by increasing the outlet radius ratio η^{out} at the constant Reynolds number, the recirculation bubble behind the step on the inner cylinder grows in the streamwise direction. While, the length of a recirculation zone on the outer cylinder shrinks in both axial and radial directions and its separation point moves toward downstream. The Reynolds number beyond which flow separation from the outer cylinder arises decreases with decreasing outlet radius ratio η^{out}. As a result the flow separation becomes stronger at constant Re upon a decrease of η^{out}. As the cylindrical effect becomes stronger by reducing η^{out} at constant Re the separation point on the outer cylinder moves upstream (Fig. 5.1). Therefore,

for small outlet radius ratios, i.e. for $\eta^{\text{out}} = 0.1$, 0.3, a strong annular jet is formed due to the upstream shift of the separation point and radial thickening of the separated zone on the outer cylinder. Since the strong shear arise on the recirculation bubble due to formation of annular jet, cat's eyes vortices embedded in the downstream part of the outer separation zone formed in the main separation zone on the outer cylinder (see Fig. 5.1(c),(d)). For the smallest outlet radius ratio considered ($\eta^{\text{out}} = 0.1$) also separation bubbles nested inside of the main recirculation zone appear. By decreasing the oulet radius ratio η^{out}, the strength of the recirculation bubble on the outer cylinder increased and the return flow upstream and along the outer cylinder inside of the separated region separates again. This leads to multiple separations of the upstream flow nested in the original large separation zone on the outer cylinder (see Figs. 5.1(d)). We do not find any co-rotating vortices for $\eta^{\text{out}} = 0.5$ and 0.998. As shown in Fig. 5.1, the numerical grid resolution is sufficient to resolve the nested viscous eddies known as Moffat vortex [70] at the locus of the sudden expansion ($z = 0$) on the inner cylinder for all considered cases.
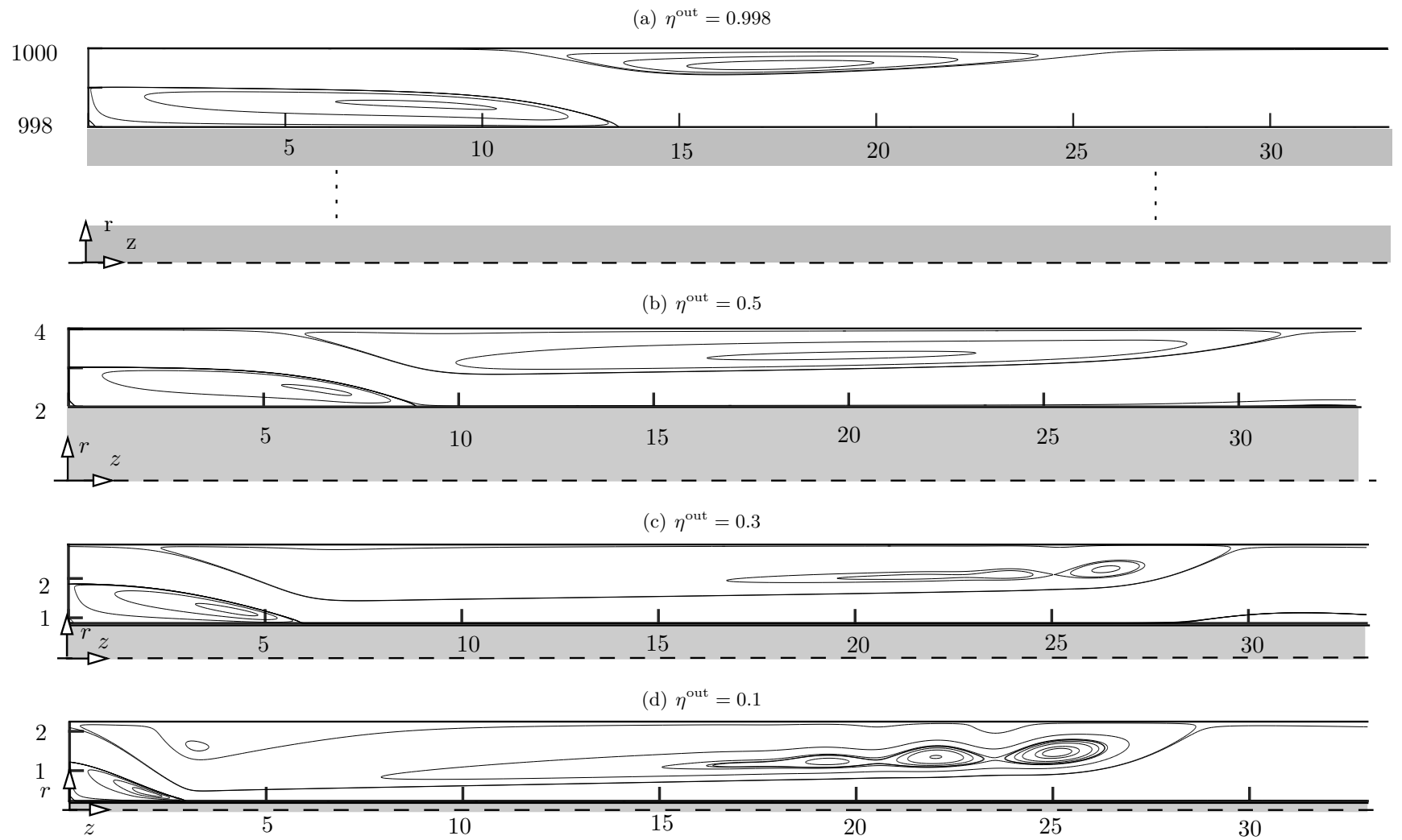
Figure 5.1.: Streamlines for the outlet radius ratio (a) $\eta^{\text{out}} = 0.998$, (b) $\eta^{\text{out}} = 0.5$, (c) $\eta^{\text{out}} = 0.3$, and (d) $\eta^{\text{out}} = 0.1$ at Re $= 800$. The expansion ratio is $\Gamma = 0.5$. The axes are in scale.

To better understand the main topological features of the basic flow, quantitative results of the flow structure for $\eta^{\text{out}} = 0.998$, 0.5, 0.3 and 0.1 and $\Gamma = 0.5$ are shown in Figs. 5.2 and 5.3. Figure 5.2 shows the length of the separation zone on the inner cylinder immediately behind the step (open symbols and solid-line) as well as the length of the main separation zone on the outer cylinder (open symbols dotted lines) as a function of Reynolds number. As it is shown, by increasing the Reynolds number (Re), the streamwise extension of the recirculation zones on both the outer and the inner cylinder becomes larger. However, beyond the Reynolds number at which separation arises on the outer cylinder, the growth with Re of the length of the recirculation zone on the inner cylinder (open symbols and solid-line) is slowed down (in the range Re $\in [50, 200]$, depending on η^{out}), while the length of the separation zone on the outer cylinder (open symbols dotted lines) continues to grow nearly linearly. The difference in behavior is particularly pronounced form small radius ratios.
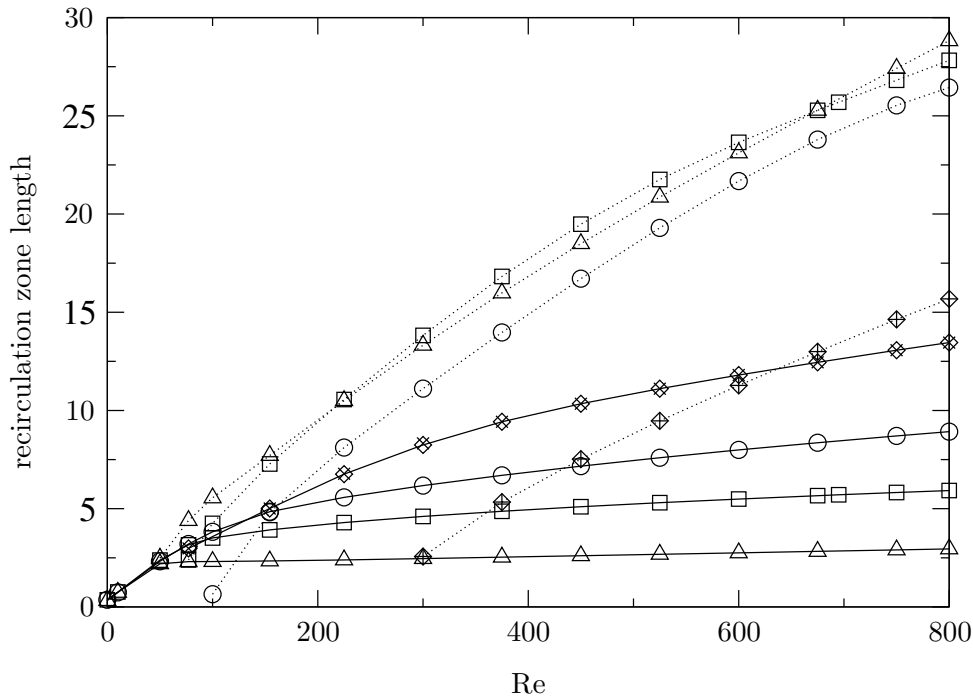

Figure 5.2.: Length of the recirculation zones on the inner (full lines) and the outer cylinder (dotted lines) as functions of the Reynolds number Re for different outlet radius ratios η indicated by open symbols: $\eta = 0.998$ ($\diamond$), 0.5 ($\circ$), 0.3 ($\square$), and 0.1 ($\triangle$). For comparison the results for plane flow of Barkley et al. [10] are shows for the length of the primary ($\times$) and secondary recirculation zone ($+$), respectively.

The lenght of the recirculation zones as a function of Re for the backward-facing step in plane channel flow is computed by extracting the location of separation and reattachment points obtained by Barkley et al. [10] (see the ($\times$) (primary recirculation length) and the $+$ (secondary recirculation length) in Fig. 5.2). By comparing the obtained recirculation lengths on the inner and outer cylinder for $\eta^{\text{out}} = 0.998$ and results of Barkley et al. [10], it can be seen that backward-facing step in a plane-channel problem is recovered in the limit of radius ratio $\eta^{\text{out}} \to 1$.

Figure 5.3 shows the z coordinates of the separation (dotted lines) and reattachment (solid
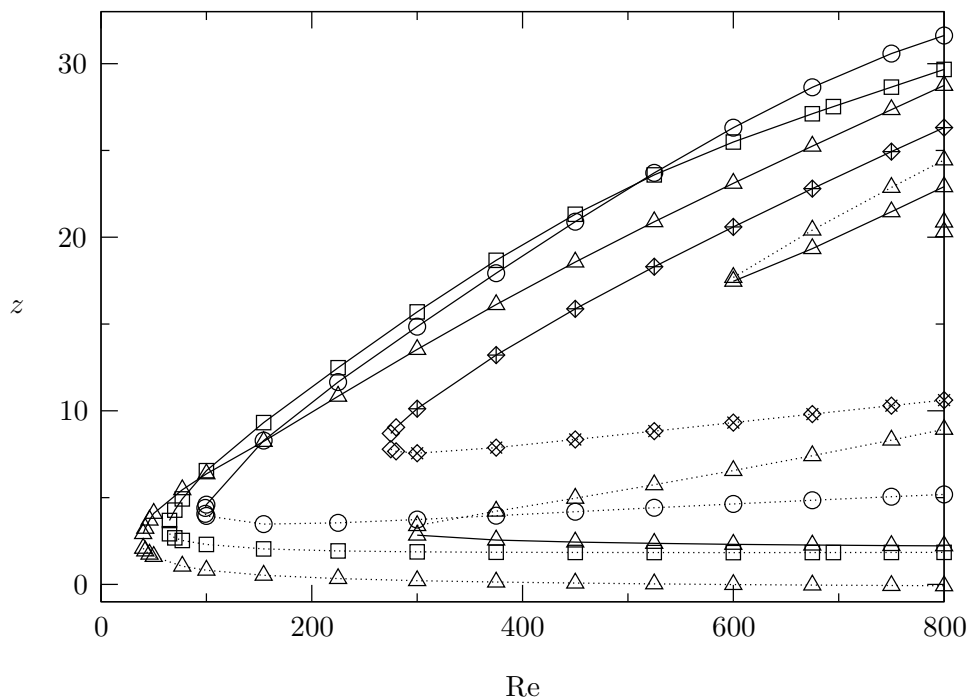
Figure 5.3.: Separation (dotted lines) and reattachment points (solid lines) on the outer cylinder for step height $\Gamma = 0.5$ and outlet radius ratios $\eta = 0.998$ ($\Diamond$), 0.5 ($\circ$), 0.3 ($\square$), 0.1 ($\triangle$) as a function of the Reynolds number Re. The separation and reattachment points obtained by Barkley et al. [10] for a backward-facing step in plane channel flow are indicated by $\times$ and $+$, respectively.

lines) points on the outer cylinder as function of the Reynolds number. It can be seen that for plane channel flow (diamonds) the separation arises at Re $= 269 \pm 7$. Depending on the outlet radius ratio η^{out}, the main separation zone on the outer cylinder arise at the range Re $\in [39, 275]$. For outlet radius ratios $\eta^{\text{out}} < 0.3$, by increasing the Reynolds number Re, the separation point moves toward upstream (Fig. 5.3). Therefore, a strong annular jet on the inner cylinder emerges due to the topological changes of the separation zone on the outer cylinder (Fig. 5.1). The reverse behavior is found for large outlet radius ratios η^{out}. As is shown in Fig. 5.3, for $\eta^{\text{out}} = 0.998$, by increasing the Reynolds number, the first separation point on the outer cylinder shifts downstream (also see [10]), except for a small range of Reynolds numbers near the onset of flow separation. The results also shown that for all considered oulet radius ratios η^{out}, the streamwise extension of the recirculation zone on the outer cylinder becomes larger by increasing the Reynolds number Re. For the small outlet radius ratio $\eta^{\text{out}} = 0.1$, by increasing the Reynolds number Re further separation zones nested inside the original separation zone arise. Owing to the relatively strong flow inside the stretched separation zone on the outer cylinder co-rotating vortices resembling Kelvin's cat's eyes [53] are created inside the separation zone (Fig. 5.1(c),(d)).

Figure 5.4 shows the z coordinates of the centers of the co-rotating vortices inside the outer separation zone as functions of the Reynolds number for outlet radius ratios $\eta^{\text{out}} = 0.1$ and 0.3. At low Reynolds numbers only a single vortex is present, its center being an elliptic point. By
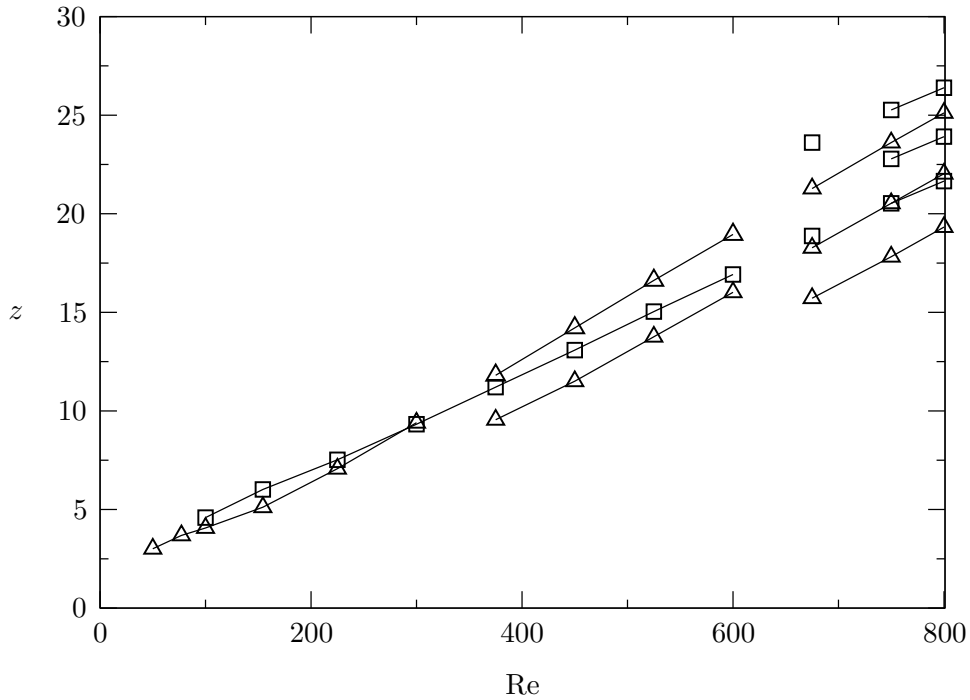
Figure 5.4.: Center of vortices inside the original separation zone on the outer cylinder as a function of Reynolds number Re for outlet radius ratio η^{out}: 0.3 ($\square$), 0.1 ($\triangle$).

increasing the Reynolds number the strain in the vortex center grows until a hyperbolic point is created associated with a splitting of the elliptic point into two. Upon a further increase of Re the more upstream located elliptic point suffers the same scenario and splits again. As a result, three elliptic points are found in the separated flow region on the outer cylinder for Re = 800.

Variation of the expansion ratio for $\eta^{\text{out}} = 0.1$

As it is shown in section 5.1.1, the steady axisymmetric annular flow over a backward-facing step is different from the flow over a backward-facing step in plane channel. It is also shown that these differences in the flow structure are due to the cylindrical geometry and they are most pronounced for a small outlet radius ratio. Therefore, in this section we discuss the basic flow for an outlet radius ratio $\eta^{\text{out}} = 0.1$ and for different expansion ratios in the range $\Gamma \in [0.25, 0.75]$.

Streamlines of the two-dimensional steady flow for outlet radius ratio $\eta^{\text{out}} = 0.1$ and three different expansion ratios $\Gamma = 0.25$, 0.5 and 0.75 are shown in Fig. 5.5 for Re = 800. Since the flow structures are extended in axial direction only part of the flow domain is shown, beginning at the step at $z = 0$ and including all recirculation regions. For all considered expansion ratios the annular flow emerging upstream of the step is deflected radially inward. Consequently a separated toroidal recirculation bubble is created instantly behind the step on the inner cylinder and the backward-facing annular disk. For Re = 800 the streamwise extension of the separated region is comparable to radial gap width of the outlet. Associated with the deflection of the annular jet towards the inner cylinder another separation zone on the outer cylinder emerges which extends in the downstream direction of the step. Streamwise extension of the outer

recirculation bubble is the most pronounced for smaller expansion ratios (Fig. 5.5(a)).

As it is shown in Fig. 5.5, by increasing the expansion ratio from $\Gamma = 0.25$, more structure are developed in the separation bubbles. By increasing the radial expansion ratio Γ, the outer separation bubble slightly expands in the radial direction, while it shrinks axially (Fig. 5.5(b),(c)). Expanding radially of the recirculation zone on the outer cylinder leads to the stronger confinement between the two separation zones and consequently forming the stronger annular jet. The annular jet attaches to the inner cylinder and widens slowly downstream until it reaches the region beyond $z = 25$ and $z = 15$ for $\Gamma = 0.5$ and $\Gamma = 0.75$ respectively, where the recirculation zone on the outer cylinder re-attaches. Cat's eyes vortices embedded in the downstream part of the separation bubble on the outer cylinder with periodically alternating elliptic and hyperbolic stagnation points are formed due to the strong shear created by the annular jet on the extended recirculation zone. Upon the increase of the expansion ratio Γ, the recirculation within the outer separation zone become stronger and consequently, the return flow along the outer cylinder inside of the large separated zone separates again which leads to emerging multiple separations of the upstream flow nested in the main recirculation bubble on the outer cylinder. Most obvious in Figs. 5.5(b),(c) is the nested separation on the outer cylinder close to the step.

Figure 5.5 also shows that, there is a recirculation region behind the step along the inner cylinder. For $\zeta = 0.25$ and 0.5, a single vortex and also a viscous eddy [70] at the corner behind the step are present. By further increase the step height, a seperation bubble nested into the original recirculation region appears and single vortex splits into several vortices owing to the strong strain in the vortex.
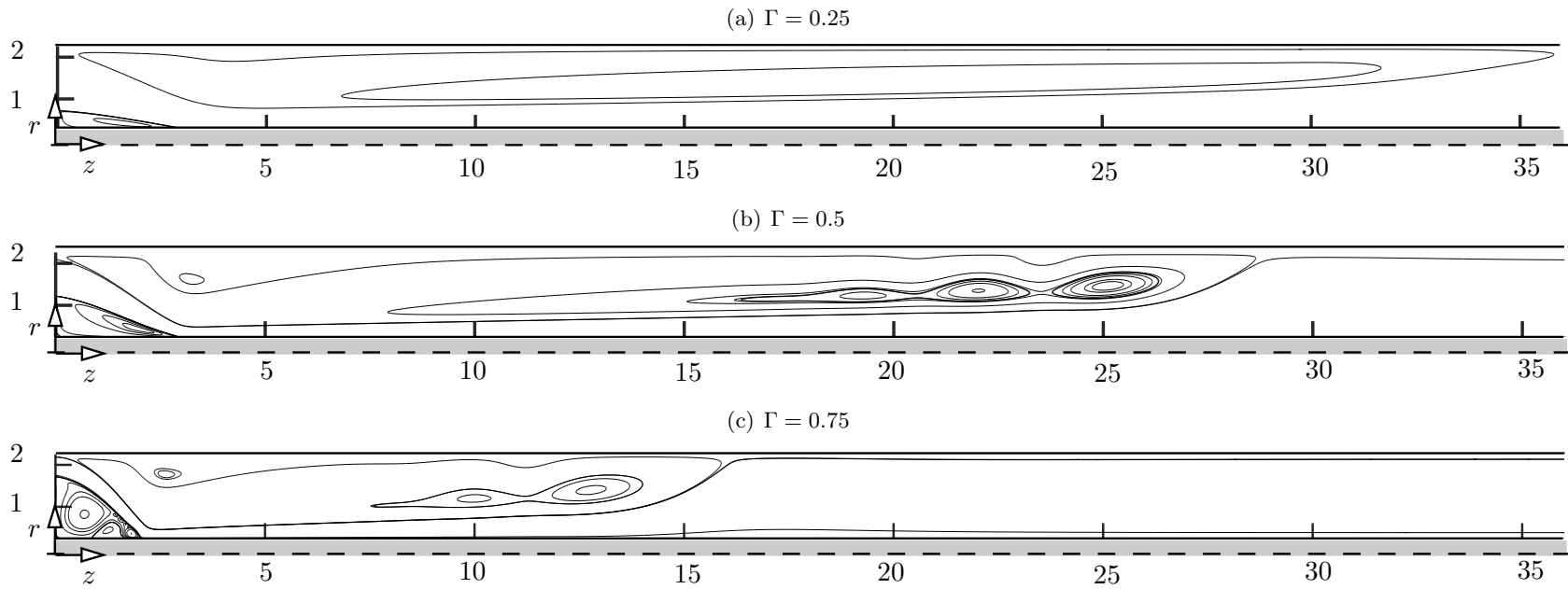
Figure 5.5.: Streamlines of the basic flow for outlet radius ratio $\eta^{\text{out}} = 0.1$ and Re $= 800$. Results are shown for expansion ratios $\Gamma = 0.25$ (a), $\Gamma = 0.5$ (b), and $\Gamma = 0.75$ (c). Only part of the full computational domain is shown. Stokes streamfunction isolines are not equidistant.

comparing Figs. 5.5(b),and 5.5(c), it can be seen that upon increase of the expansion ratio to $\Gamma = 0.75$ at $\text{Re} = 800$, in addition to the axial contraction and a slight radial expansion of the outer separation bubble, more structure developes within the recirculation zone on the inner cylinder (Fig. 5.5(c)). Figure 5.6 quantifies this change of the separated vortex on the inner cylinder and shows the separation (open symbols and dotted lines) and re-attachments (full symbols and solid lines) points on the inner cylinder as functions of the Reynolds number. It can be seen that the length of the separation bubble on the inner cylinder increases strongly by increasing the Re from zero to about $\text{Re} \approx 100$. The length of the inner recirculation zone remains of the same order of the outlet width for higher Reynolds numbers. As it is shown in Fig. 5.6, another separation bubble nested into the main separation zone emerges on the inner cylinder at $\text{Re} = 370 \pm 5$ which grows in size by increasing the Re. The Moffat vortex [70] is found for all investigated Reynolds numbers at the 90-degrees corner at the locus of the step which creates by the intersection of the inner cylinder and the annular disk. Figure 5.6 also shows that creating the nested separation bubble does not effect viscous eddies [70].
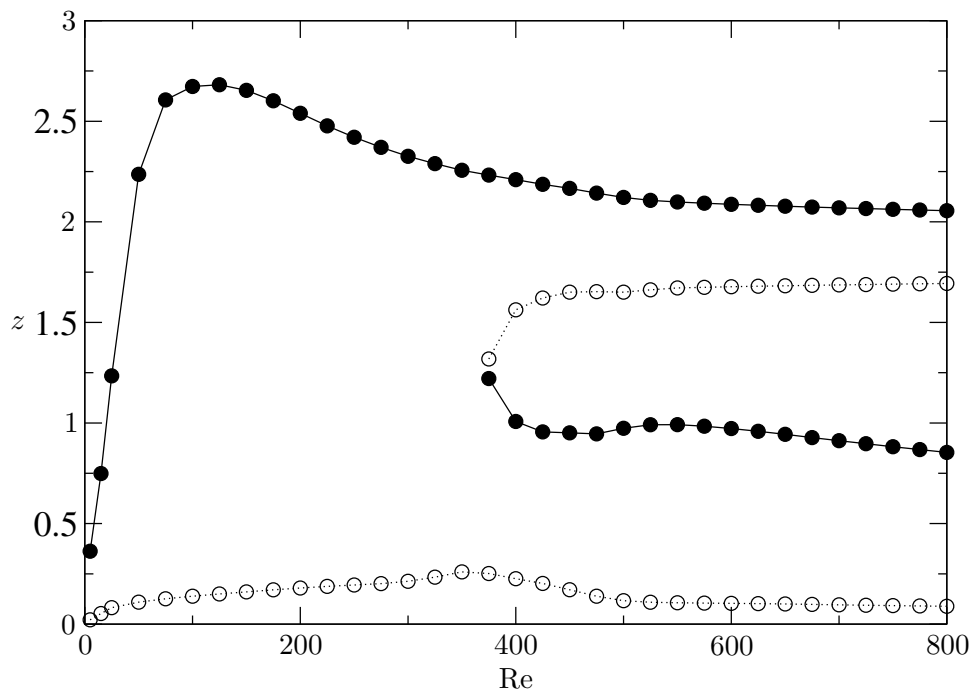

Figure 5.6.: Separation (open symbols and dotted lines) and reattachment points (full symbols and solid lines) on the inner outlet cylinder as functions of Re for $\eta = 0.1$ and $\Gamma = 0.75$ $(\circ, \bullet)$.

To better quantify the separation zones, Fig. 5.7 depicted the z locations of the separation (open symbols and dotted lines) and reattachment (full symbols and solid lines) points on the outer cylinder as function of the Reynolds number for three different expansion ratios $\Gamma = 0.25$, 0.5 and 0.75. It can be seen that for all expansion ratios considered, the main recirculation bubble on the outer cylinder creates at the range $\text{Re} \in [39, 54]$ depending on the expansion ratio Γ. By increasing the Reynolds number, the recirculation zones for all considered expansion ratios grow in streamwise direction. Upon the increase of Re, the separation point slightly
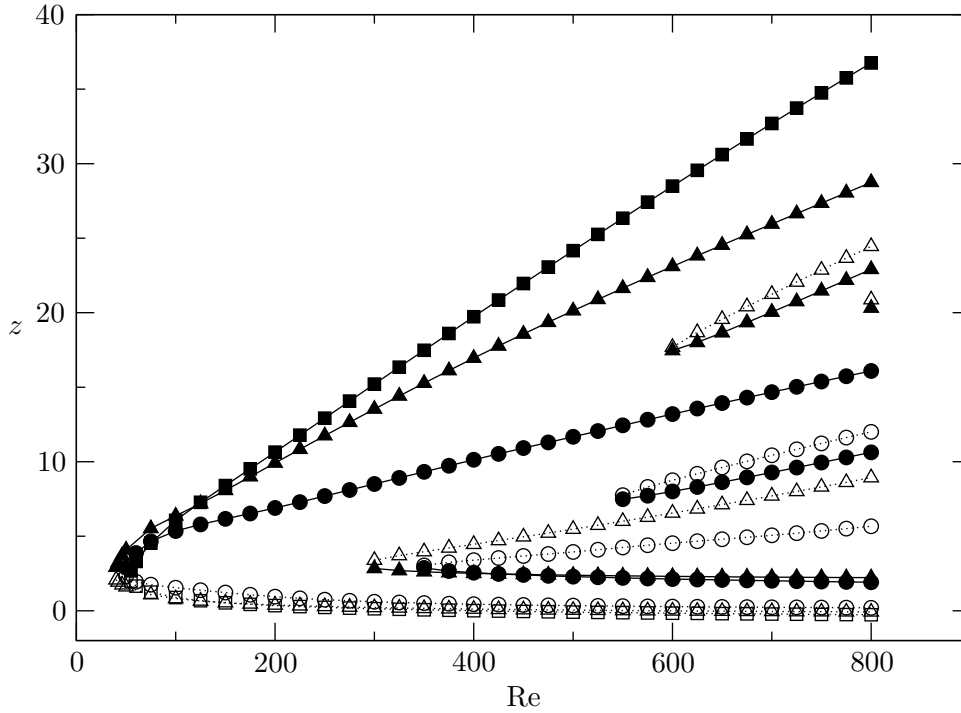
Figure 5.7.: Separation (open symbols and dotted lines) and reattachment points (full symbols and solid lines) on the outer cylinder as functions of Re for $\eta = 0.1$ and $\Gamma = 0.25$ ($\square$, $\blacksquare$), 0.5 ($\triangle$, $\blacktriangle$) and 0.75 ($\circ$, $\bullet$).

moves upstream and the re-attachment points, however, moves downstream. This effect is more pronounced for the smaller the expansion ratios.

Figure 5.5(a) shows that there is not any nested separation bubble in the upstream flow within the large separation zone on the outer cylinder for $\Gamma = 0.25$. In contrary, for $\Gamma = 0.5$ and $\Gamma = 0.75$, the first nested recirculation bubble emerges near the step at $\text{Re} = 290 \pm 10$ and $\text{Re} = 340 \pm 10$, respectively. Further nested recirculation bubbles arise for higher Reynolds numbers with up to three nested separations for $\Gamma = 0.75$ and $\text{Re} = 800$. All separation and re-attachment of the nested recirculation zones are displayed downstream as Re increases, except for the main nested separation for which the reattachment point moves upstream (full symbols in Fig. 5.7).

5.1.2. Expansion into a simple pipe

By removing the inner cylinder of the outlet, two-dimensional axisymmetric flow expansion into a simple pipe is computed by solving the steady Navier–Stokes and continuity equations. Except the axis of the symmetry the other boundary conditions are the same as annular backward-facing step flow problem.
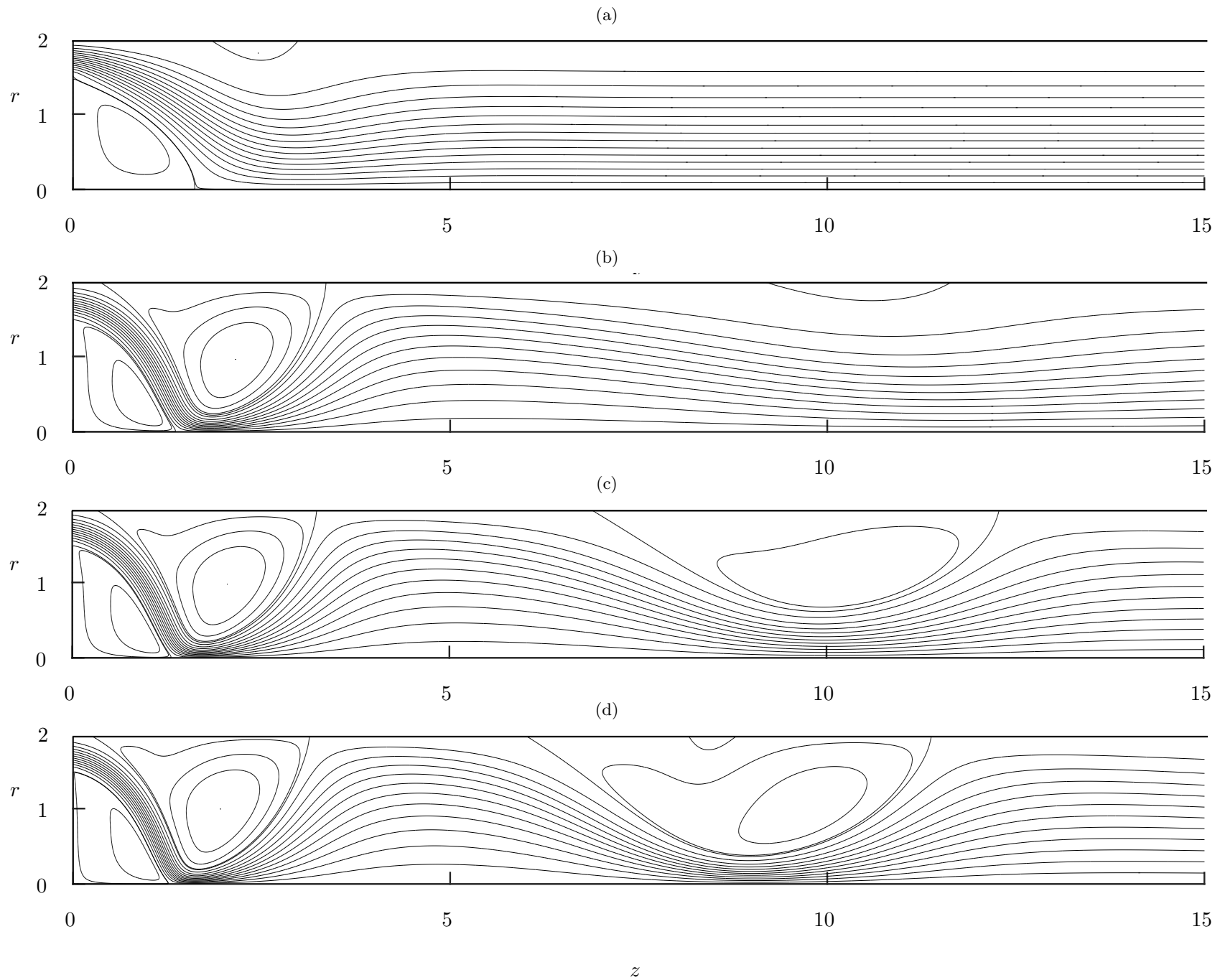
Figure 5.8.: Streamlines for the annular flow expansion into a simple pipe at Reynolds number (a) Re = 40, (b) Re = 240, (c) Re = 300 and (d) Re = 400. The expansion ratio is $\Gamma = 0.75$. The axes are in scale.

Two-dimensional flow is computed for three different expansion ratios $\Gamma = 0.75$, 0.5 and 0.25. To show the flow structure as a function of the Reynolds number Re qualitatively, streamlines for $\Gamma = 0.75$ for four different Reynolds numbers (Re $= 40$, 240, 300 and 400) are shown in Fig. 5.8. In this figure only a part of the domain where the recirculation bubbles emerges is shown beginning at the locus of the expansion at $z = 0$. As it can be seen in Fig. 5.8(a), at Re $= 40$, a recirculation zone immidiately behind the cylindrical disk along the axis and another seperation region on the wall of the pipe are present. By increasing the Reynolds number, the vortex on the pipe wall grows significantly in the radial direction and it moves toward upstream. Due to the topological changes (radial thickening and moving upstream) of the seperated recirculation zone, a strong annular jet is created at the center of the annular pipe.

Owing to the reattachment point of the first recirculation zone on the outer cylinder, the annular jet expands strongly and the flow slows down significantly. As a result, the boundary layer on the pipe wall decelerates and grows in a radial direction rapidly, and it separates again from the pipe wall (see Fig. 5.8(b)-(d)). By increasing the Reynolds number, the second recirculation zone on the pipe wall grows radially and axially. For the Re $= 400$, a seperation bubble nested inside the second recirculation zone on the outer cylinder is present (5.8(d)).
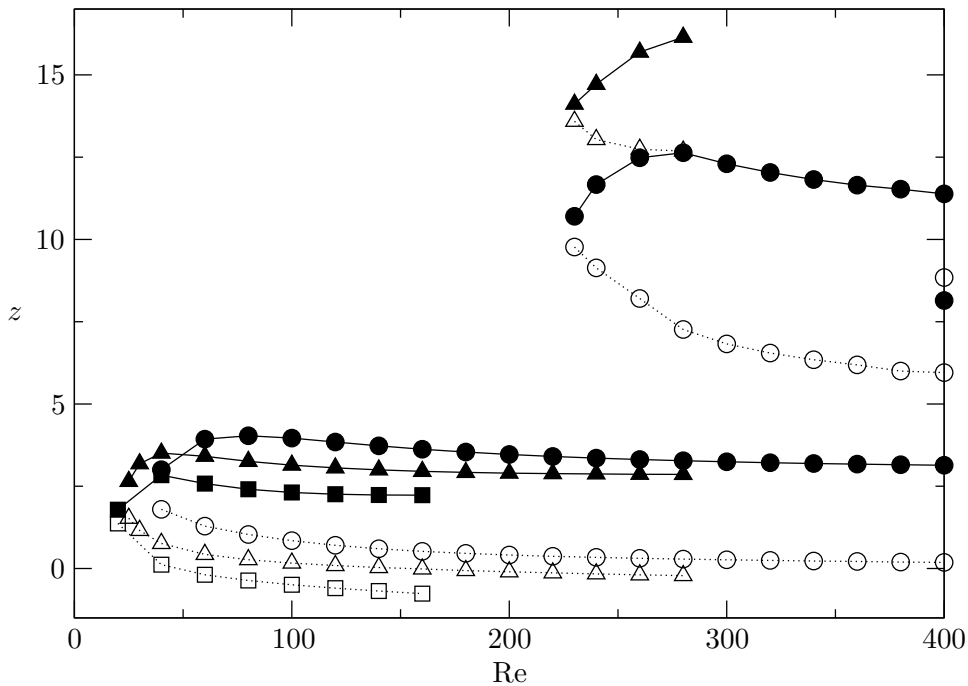

Figure 5.9.: Separation (open symbols and dotted lines) and reattachment points (full symbols and solid lines) on the outer cylinder as functions of Re for the expansion ratio Γ: 0.25 ($\square$, $\blacksquare$), 0.5 ($\triangle$, $\blacktriangle$), 0.75 ($\circ$, $\bullet$).

To better quantify the separation zones the separation points (full symboles and dotted lines) and the reattachment points (open symboles and solid lines) on the pipe wall as a function of Reynolds number Re for the expansion ratios $\Gamma = 0.75$, 0.5 and 0.25 are shown in Fig. 5.9. It can be seen that the first seperation zone arises at the Reynolds number in the range Re $\in [15, 40]$ depending on the expansion ratio Γ. This recirculation zone grows rapidly and after the certain

Reynolds number $\mathrm{Re} \in [40, 80]$ depends on Γ. By further increase of the Reynolds number, the size of the primary separation zone approximately remains constant. As is shown in Fig. 5.9, by increasing the Reynolds number, the first separation zone on the pipe wall moves upstream. This effect is more pronounced for smaller expansion ratios. It can be seen that, by further increase of the Reynolds number, another seperation occures downstream. By increasing the Reynolds number, the second recirculation zones extends in a streamwise direction and move toward upstream.

5.2. Stability analysis

In this section the results of the two and three-dimensional linear stability analysis for the investigated set-ups are addressed. Therefore, this section comprises of two main parts. In the first part, the flow over backward-facing step in an annular pipe and in the second part, the annular flow which expands into a simple pipe are considered. The neutral curves and stability boundary as a function of η^{out} and Γ are computed. Finally, by means of an *a posteriori* energy analysis pretained instability mechanisms are investigated and discussed in details for representative cases.

5.2.1. Flow over backward-facing step in an annular pipe

Since the flow stability in a streamwise sufficiently extended system depends on the radius ratio η^{out} and the expansion ratio Γ, in this section the neutral curves and the critical modes are computed and discussed for two different cases. In the first case, the expansion ratio is fixed ($\Gamma = 0.5$) and we vary the outlet radius ratio in the range $\eta^{\mathrm{out}} \in [0.1, 0.5]$ to investigate the deviation of the critical mode from the plane channel case. Since the effect of the cylindrical geometry becomes important as $\eta^{\mathrm{out}} \to 0$, in the second case, the outlet radius ratio is fixed to $\eta^{\mathrm{out}} = 0.1$ and we investigate the effect of the expansion ratio which varies in the range $\Gamma \in [0.25, 0.75]$. To understand the instability mechanisms an *a posteriori* energy analysis is performed for each investigated case, and the instability mechanisms for representative cases are discussed in each part based on the kinetic-energy-transfer characteristics.

Variation of the outlet radius ratio η^{out} for $\Gamma = 0.5$

A linear stability analysis for a radial step height $\Gamma = 0.5$ varying outlet radius ratios in the range $\eta^{\mathrm{out}} \in [0.1, 0.5]$ is performed for the integer azimuthal wave numbers in the range $m \in [0, ..., 8]$. The results of two dimensional linear stability analysis ($m = 0$) which is performed for $\eta^{\mathrm{out}} = 0.1$, 0.3 and 0.5 up to the Reynolds number $\mathrm{Re} = 1200$, show that the grow rate of axisymmetric perturbations are negative in all considerd cases. The results of the investigated parameters shown that no axisymmetric perturbation is found to be critical. Neutral curves for other considered wave numbers m are shown in Fig. 5.10. In this figure, we showed each wave number by a specific type of symbol and solid and dotted lines denote stationary and oscillatory modes, respectively.
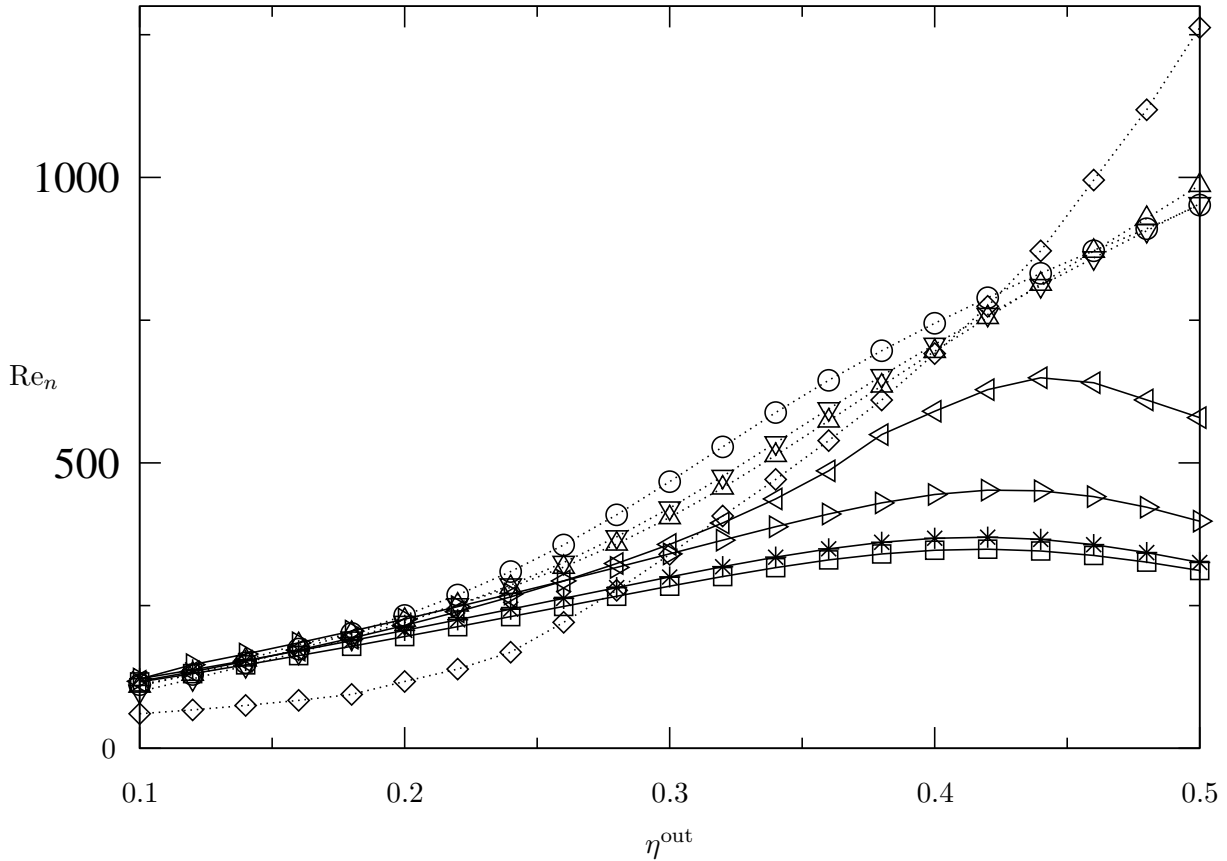
Figure 5.10.: Neutral Reynolds numbers Re_n as functions of outlet radius ratio η^{out} for various wave numbers m: 1 ($\diamond$), 2 ($\triangle$), 3 ($\triangledown$), 4 ($\circ$), 5 ($\triangleleft$), 6 ($\square$), 7 ($*$) and 8 ($\triangleright$) for $\Gamma = 0.5$. Stationary instabilities are shown by solid lines, whereas oscillatory instabilities are represented by dotted lines.

For $m = 1$, 2, 3 and 4 the instability is oscillatory. While, for higher wave numbers $m = 5$, 6, 7 and 8 the instability is stationary. The neutral Reynolds numbers for the oscillatory modes increase monotonically as outlet radius ratios (in the range investigated) increased, whereas the neutral Reynolds numbers of the stationary modes exhibit a maximum at outlet radius ratios in the range $\eta^{\mathrm{out}} \in [0.4, 0.45]$ depending on the outlet radius ratio η^{out}. At low radius ratios, the neutral curves are quite close to each other with $m = 1$ being the critical wave number in the range $\eta^{\mathrm{out}} \in [0.1, 0.274]$ and the instability is oscillatory. As η^{out} increases the oscillatory frequency increasing from 0.1247 at $\eta^{\mathrm{out}} = 0.1$ to 0.1423 at $\eta^{\mathrm{out}} = 0.26$ (see details in Table. 5.1). The oscillatory critical mode with $m = 1$ is replaced by another mode with the wave number $m = 6$ which is stationary. This mode become critical in the range $\eta^{\mathrm{out}} \in [0.275, 0.5]$ and shows a maximum as function of the radius ratio at $\eta^{\mathrm{out}} = 0.42 \pm 0.019$. Figure 5.10 also shows that for $\eta^{\mathrm{out}} < 0.2$ a complicated nonlinear flow dynamics can be expected already slightly above the critical Reynolds number.

By enveloping neutral curves for $\Gamma = 0.5$, two different branches depending on the outlet radius ratio η^{out} found to be critical (Fig. 5.10). Branch 1 with $m_c = 1$ is critical for the small

η^{out}	Re_c	m_c	$\pm\omega_c$
0.1	60.4998	1	0.1247
0.12	67.2582	1	0.1304
0.14	74.9573	1	0.1346
0.16	83.8607	1	0.1373
0.18	94.3104	1	0.1391
0.20	116.9833	1	0.1399
0.22	138.7573	1	0.1400
0.24	168.2524	1	0.1401
0.26	220.6734	1	0.1423
0.28	266.3725	6	0
0.30	283.9432	6	0
0.32	300.8558	6	0
0.34	316.4567	6	0
0.36	329.9698	6	0
0.38	340.4389	6	0
0.40	346.9104	6	0
0.42	348.7099	6	0
0.44	345.5370	6	0
0.46	337.7544	6	0
0.48	326.0799	6	0
0.50	311.4028	6	0

Table 5.1.: Critical parameters for different outlet radius ratios η^{out}.

outlet radius ratios in the range $\eta^{\mathrm{out}} \in [0.1, 0274]$ whereas branch 2 with $m_c = 6$ become critical for the larger radius ratios. The obtained crtitical Reynold number Re_c, wave number m_c and oscillation frequency ω_c are listed in Table 5.1 for the reference purposes.

To find the instability mechanisms of the critical modes, an *a posteriori* energy analysis of the exchange of kinetic energy between the basic flow and the critical mode is performed as in Lanzerstorfer and Kuhlmann [60] for selected outlet radius ratios. The derivation is provided in the appendix. Table 5.2 shows the normalized integral energy production rates in the bulk, the transport rate of perturbation energy through the outlet surface K^{out}, the locus z_{max} of the maximum total local energy transfer rates in a streamwise direction, the locus r_{max} of the maximum total local energy transfer rates in a radial direction, the critical wavenumber m_c, the critical Reynolds number Re_c and the critical frequency ω_c. Inserting the computed energy transfer terms from Table. 5.2 into (2.22) fulfil conservation of kinetic perturbation energy (see (2.29)) up to 5 decimal places for all of the representative cases. It can be been that for $\eta^{\mathrm{out}} = 0.5$ and 0.4, perturbations are not vanished at the outlet surface $K^{\mathrm{out}} \neq 0$ because of the finite length of the annular pipe.

The integral importance for the instability of each normalized energy production term $\int_V I_{\mathrm{i}}' dV$ shown in Table. 5.2 depends on its magnitude. A positive term contributes to a destabilization, whereas a negative term contributes to a stabilization of the respective mode.

As a representative case for branch 2 and large radius ratios we consider $\eta^{\mathrm{out}} = 0.5$ and

η^{out}	0.5	0.4	0.3	0.2	0.1
$\int_V I_1' dV$	0.5135	-0.2187	0.0025	0.0422	0.0134
$\int_V I_2' dV$	4.1520	-1.8294	0.0844	0.6120	0.3720
$\int_V I_3' dV$	-0.1993	0.1393	0.0249	0.0246	0.0315
$\int_V I_4' dV$	-3.4301	2.8888	0.8827	0.3212	0.5379
$\int_V I_5' dV$	-0.0384	0.0217	0.0056	0.7372×10^{-5}	0.0452
K^{out}	0.0023	-0.0017	0.0000	0.0000	0.0000
$z_{\max}$	3.4238	9.0626	7.2633	5.8334	4.2530
$r_{\max}$	2.9596	1.5878	1.0981	0.8281	0.5830
m_c	6	6	6	1	1
Re_c	311.4028	346.9104	283.9432	116.9833	60.4998
ω_c	0	0	0	0.1399	0.1247

Table 5.2.: Normalized energy production rates for different outlet radius ratios η^{out}. $z_{\max}$ and $r_{\max}$ are the place of the maximum total local energy production in z and r direction respectively.

$\Gamma = 0.5$ for which the critical wave number is $m_c = 6$. Figure 5.11(a) depicted streamlines of the basic flow (solid lines), the stationary critical mode (vectors), and the total local energy transfer rate $\sum_{i=1}^{5} I_i'$ (color map) in (r, z) plane through the locus at which the total local energy production takes its maximum value $(r_{\max}, z_{\max}) = (3.4238, 2.9595)$. According to Table. 5.2, for $\eta^{\text{out}} = 0.5$ both $\int_V I_1' dV$ and $\int_V I_2' dV$ are positive and act destabilizing with $\int_V I_2' dV$ being dominant. The integrand $I_2' = -D^{-1}\tilde{\boldsymbol{u}}_{\parallel} \cdot (\tilde{\boldsymbol{u}}_{\perp} \cdot \nabla \boldsymbol{u}_0)$ describes the amplification of streamwise perturbation momentum $\tilde{\boldsymbol{u}}_{\parallel}$ by cross-stream transport caused by the perturbation $\tilde{\boldsymbol{u}}_{\perp} \cdot \nabla$ of basic state momentum $\boldsymbol{u}_0$. It is shown that the perturbation velocity is increased in the shear layer around the separating streamline. The energy transfer due to $\int_V I_2' dV$ has a maximum in the region of strong shear gradient near the separating streamline of the recirculation zone on the inner cylinder. This is the typical lift-up mechanism which leads to a critical mode that is characterized by strong slow and fast streaks alternating in azimuthal direction (isolines in Fig. 5.12) associated with weak streamwise vortices in this region (see [58], [59]).

Figure 5.12 shows the streamwise perturbation $\tilde{w}$ (isolines), the critical flow field in (r, ϕ) plane (vectors) and the total local energy production (colormap) in a plane through the station $z_{max} = 3.4238$ at which the total local energy production takes its maximum value. It can be seen that the maximum local total energy is due to the strong streamwise perturbation component $\tilde{w}$ that is creates by the lift-up mechanism in which cross-stream transport of the base flow $\tilde{\boldsymbol{u}}_{\perp} \cdot \nabla$ amplifies the streamwise perturbations. In this case the streamwise perturbation component $\tilde{w}$ is much larger than the perturbation components in r ($\tilde{u}$) and ϕ ($\tilde{v}$) directions.

As it shown in Table 5.2, the second dominant term which destabilize the flow for $\eta^{\text{out}} = 0.5$ is $\int_V I_1' dV$. The integrand $I_1' = -D^{-1}\tilde{\boldsymbol{u}}_{\perp} \cdot (\tilde{\boldsymbol{u}}_{\perp} \cdot \nabla \boldsymbol{u}_0)$ describes the amplification of cross-stream perturbation momentum $\tilde{\boldsymbol{u}}_{\perp}$ by a cross-stream transport of the base flow $\boldsymbol{u}_0$ momentum caused by the perturbation $\tilde{\boldsymbol{u}}_{\perp} \cdot \nabla$. Figure 5.11(c) depicted the local energy production associated with the term I_1', in a plane where the total local energy takes its global maximum. It can be seen that the local maximum and minimum of the energy transfer due to I_1' is near the
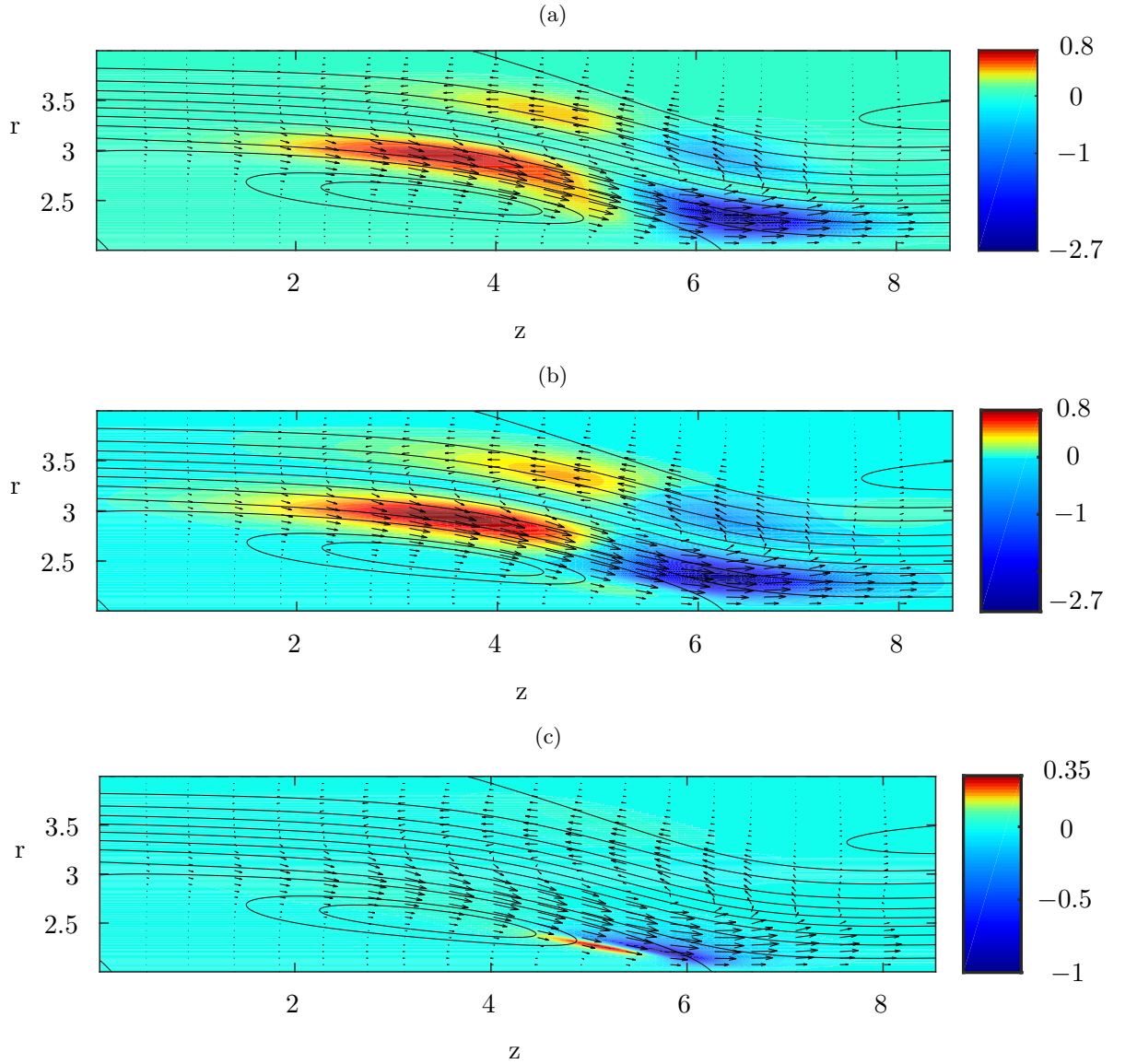
Figure 5.11.: Basic state (streamlines), critical velocity field (vectors) and local energy produc-
tion (colormap) for $\eta^{\text{out}} = 0.50$ and expansion ratio $\Gamma = 0.50$. Shown are the (r, z)
plane through the locus $(r_{\max}, z_{\max}, \phi_{max}) = (2.9596, 3.4238, 0)$ at which the total
local energy production takes its global maximum (a) total local production $\sum_i I_i'$,
(b) I_2', (c) I_1'.

reattachment point of the recirculation zone on the inner cylinder. In this case, the orientation
of the separating streamlines $\boldsymbol{u}_0$ changes with respect to itself which cause the amplification of
cross-stream perturbation $\tilde{\boldsymbol{u}}$. Comparing the importance of the destabilizing effect of I_1' (Fig.
5.11(c)) and I_2' (Fig. 5.11(b)), I_2' is by far dominant in this case. All the other terms have
stabilizing effect in the considered geometry.

By reducing the outlet radius ratio up to $\eta^{\text{out}} = 0.274 \pm 0.005$, the critical mode with the wave
number $m_c = 6$ remains same, but the structure of the critical mode changes smoothly (see Fig.
5.13). The reason is the existance of different instability mechanisms simultaneously, however
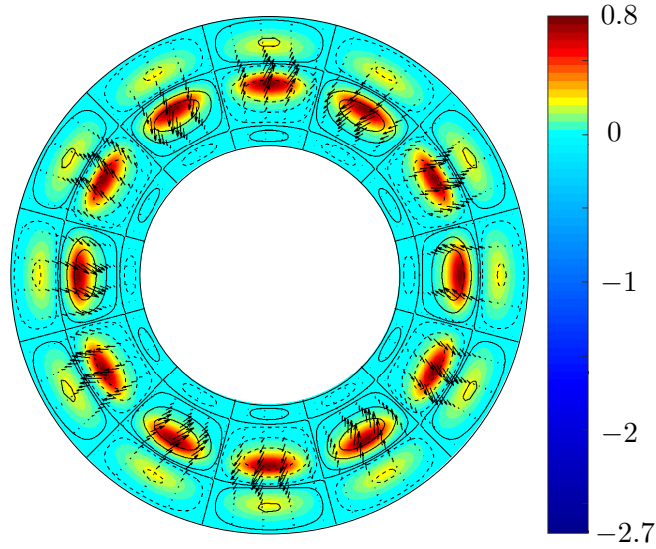
59

Figure 5.12.: Purturbations in (r, ϕ) plane (vectors), streamwise perturbation velocity $\tilde{w}$ (isolines) and the total local energy $\sum_i I_i'$ (colormap) at the station $z_{\max} = 3.4238$ for $\eta^{\mathrm{out}} = 0.50$ and expansion ratio $\Gamma = 0.50$ at the critical condition ($m_c = 6$, $\mathrm{Re}_c = 311.4028$). Solid (dashed) isolines indicated the positive (negative) value of the streamwise perturbation velocity $\tilde{w}$.

with different importance. Figure 5.13(a) shows that the dominant instability mechanism for $\eta^{\mathrm{out}} = 0.5$ is due to the local energy growth along the separating streamlines of the separation bubble on the inner cylinder. However, by decreasing the outlet radius ratio another instability mechanism becomes dominant. Based on the informations provided by Table. 5.2, this instability mechanism is characterized by the dominance of the integral over I_4'. The integrand $I_4' = -D^{-1}\tilde{\boldsymbol{u}}_\parallel \cdot \left(\tilde{\boldsymbol{u}}_\parallel \cdot \nabla \boldsymbol{u}_0 \right)$ describes the amplification of streamwise perturbation momentum $\tilde{\boldsymbol{u}}_\parallel$ by streamwise transport due to the perturbation flow $\tilde{\boldsymbol{u}}_\parallel \cdot \nabla$ of basic state momentum $\boldsymbol{u}_0$. Thus, this mechanism builds on the deceleration of the basic flow $\tilde{\boldsymbol{u}}_\parallel \cdot \nabla \boldsymbol{u}_0 < 0$. As shown in Fig. 5.13 for $0.274 \leq \eta^{\mathrm{out}} \leq 0.4$, a strong jet on the inner cylinder is formed behind the step. Owing to the slow reattachment of the outer recirculation zone, the basic flow jet at the center of the annular pipe gradually widens, as in a diffusor. As a result, the incompressible flow decelerates downstream leading to the instability caused by streamwise velocity gradients of the basic state.

By further decreasing of the outlet radius ratio another mode with $m = 1$ which is oscillatory intersects with the critical stationary mode with $m = 6$ at $eta^{\mathrm{out}} = 0.274 \pm 0.005$ and become the critical mode for the smaller outlet radius ratios (see Fig. 5.10). As a representative example for a critical mode with $m_c = 1$, the outlet radius ratio $\eta^{\mathrm{out}} = 0.2$ is considered. By looking into the integral budgets of the critical mode (Table. 5.2), it can be seen that all the energy production integrals $\int_V I_1' \mathrm{d}V$, $\int_V I_2' \mathrm{d}V$, $\int_V I_3' \mathrm{d}V$, $\int_V I_4' \mathrm{d}V$ and $\int_V I_5' \mathrm{d}V$ have a destabilizing effect with $\int_V I_2' \mathrm{d}V$ and $\int_V I_4' \mathrm{d}V$ being dominant. Therefore, several instability mechanisms are working simultaneously. The integrands $I_2' = -D^{-1}\tilde{\boldsymbol{u}}_\parallel \cdot \left(\tilde{\boldsymbol{u}}_\perp \cdot \nabla \boldsymbol{u}_0 \right)$ and $I_4' = -D^{-1}\tilde{\boldsymbol{u}}_\parallel \cdot \left(\tilde{\boldsymbol{u}}_\parallel \cdot \nabla \boldsymbol{u}_0 \right)$
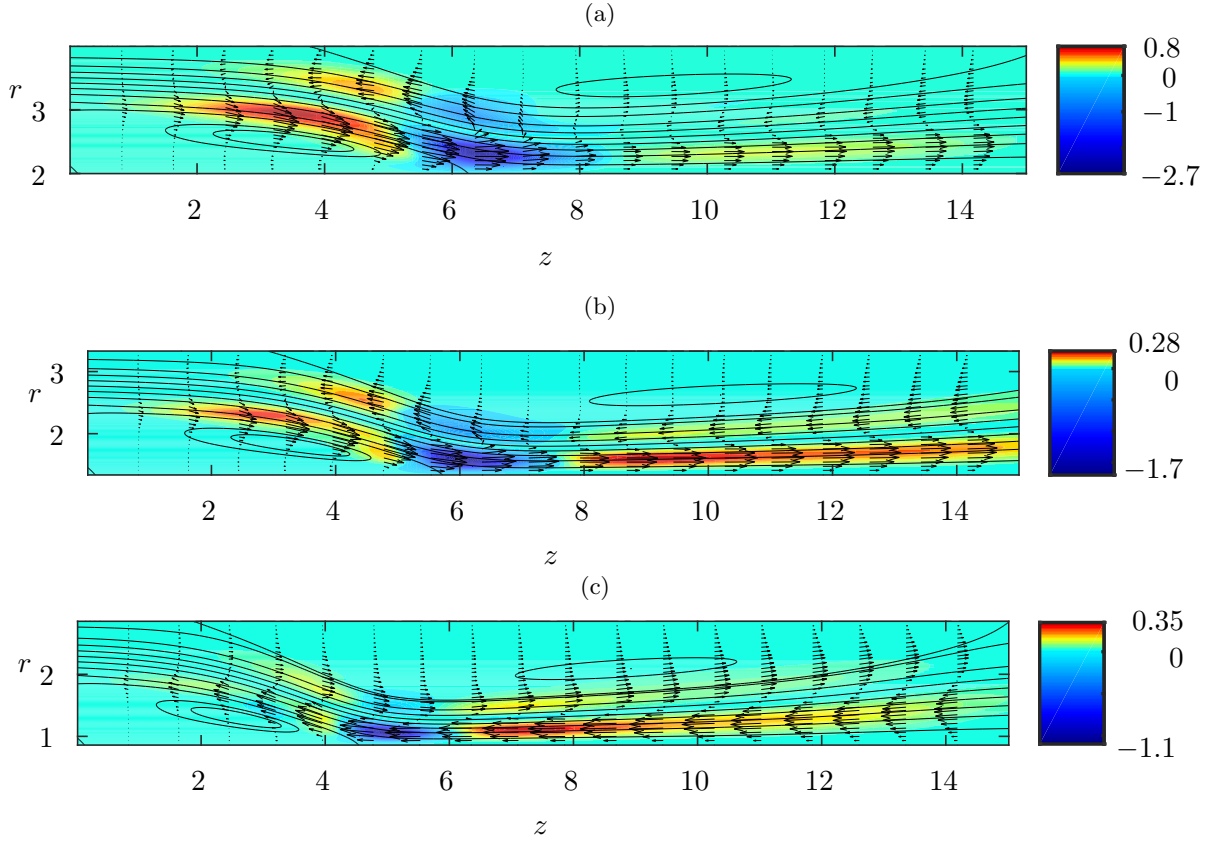
(a)

(b)

(c)

Figure 5.13.: Basic state (streamlines), critical velocity field (vectors) and total local energy production $\sum_i I_i'$ (colormap) in (r,z) plane at which the total local energy production $\sum_i I_i'$ takes its global maximum for various outlet radius ratios η^{out}: (a) 0.5, (b) 0.4, (c) 0.3.

describe the amplification of streamwise perturbation momentum $\tilde{\boldsymbol{u}}_{\parallel}$ by cross-stream $(\tilde{\boldsymbol{u}}_{\perp} \cdot \nabla)$ and streamwise $(\tilde{\boldsymbol{u}}_{\parallel} \cdot \nabla)$ transport of the basic flow momentum $\boldsymbol{u}_0$ caused by the perturbations respectively.

The total local energy production for the outlet radius ratio $\eta^{\text{out}} = 0.2$ and $\Gamma = 0.50$ at the (r,z) plane which the total local energy production takes its maximum is shown in Fig. 5.14(a). It can be seen that the total local energy takes its maximum at locus $(z_{\max}, r_{\max}) = (5.8334, 0.8281)$ where the jet starts to decelerate due to the reattachment point of the recirculation zone on the outer cylinder. In addition, there is a high shear gradient between the wall and the jet which induces instability due to the cross-stream transport of energy by $\tilde{\boldsymbol{u}}_{\perp}$. Therefore, both lift-up and deceleration instability mechanism superimposed in the region near the inner cylinder where the jet expands and lead to destabilization of the basic flow. Figures 5.14(b) and 5.14(c) represent the local energy transfer to the perturbation flow due to the contribution of the terms I_2' and I_4', respectively. As it is seen, different instability mechanisms with approximately same importance work simultaneously to destabilize the flow in this case. Although, the energy production integral $\int_V I_2' dV$ dominates over $\int_V I_4' dV$ in the whole volume (see Table. 5.2), however the local maximum production in (r,z) plane at which the total local energy production takes its maximum belongs to the term I_4' which correspond to the flow deceleration located downstream
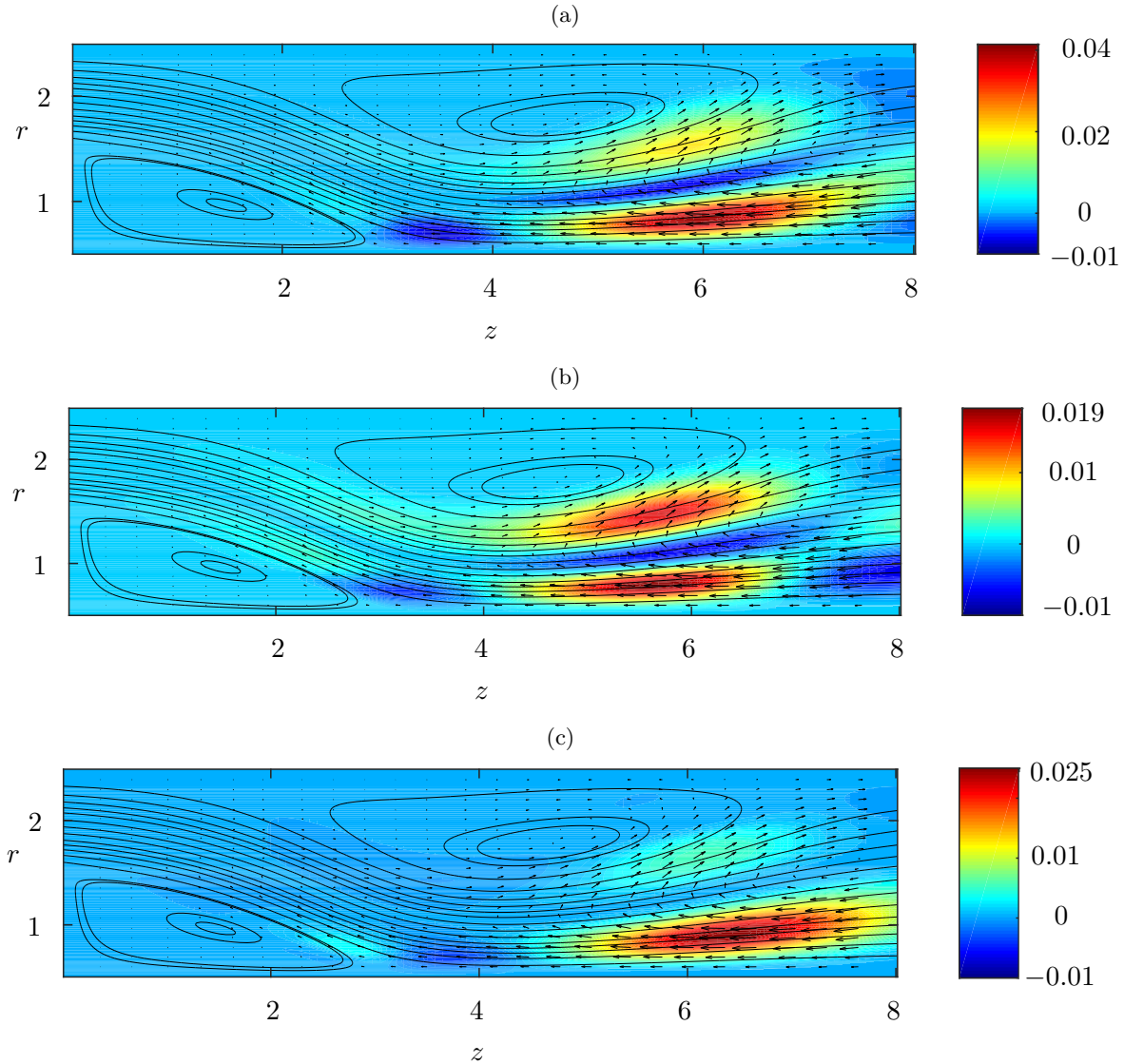
61

Figure 5.14.: Basic state (streamlines), critical velocity field (vectors) and the total local energy production $\sum_i I'_i$ for $\eta^{out} = 0.2$ and $\Gamma = 0.5$. Shown are the (r, z) plane through the locus $(r_{max}, z_{max}, \phi_{max}) = (0.8281, 5.8334, 1.9489\pi)$ at which the total local energy production takes its global maximum (a) total local production $\sum_i I'_i$, (b) I'_2, (c) I'_4. The axis are in scale.

of the jet slightly above the inner cylinder. Figure 5.15 shows perturbations in (r, ϕ) plane (vectors), streamwise perturbation velocity $\tilde{w}$ (isolines) and the total local energy $\sum_i I'_i$ (colormap) at the station $z_{max} = 5.8334$ for $\eta^{out} = 0.2$ and $\Gamma = 0.5$. The critical mode is oscillatory with $m_c = 1$ and it rotates in the counterclockwise direction with the angular frequency $\omega_c = 0.1399$. The wave rotates such that spirals characterized by $\tilde{w} = 0$ spiral outwards in the plane shown in Fig. 5.15.

In order to check if the area which experienced the instability is subjected to the centrifugal effects, the sufficient criterion of centerifugal instability is determind based on Sipp and Jacquin [94] and Rayleigh [84] formulation of generalized Rayleigh criterion. For this purpose, the local
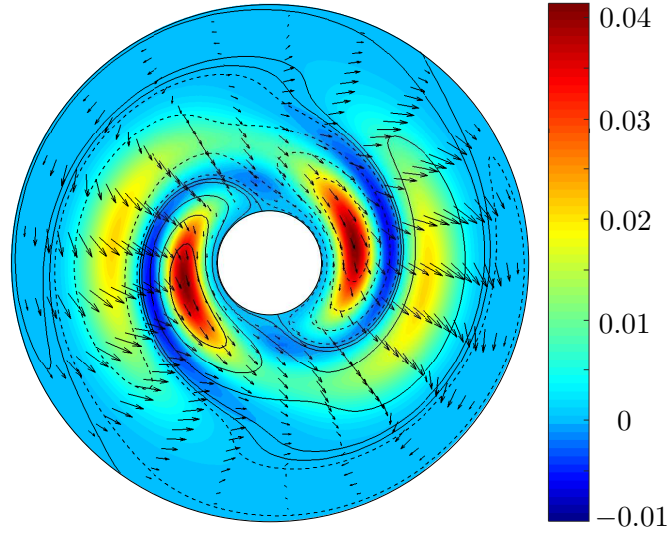
Figure 5.15.: Purturbation in (r, ϕ) plane (vectors), streamwise perturbation velocity $\tilde{w}$ (isolines) and the total local energy $\sum_i I_i'$ (colormap) at the station $z_{\max} = 5.8334$ for $\eta^{\text{out}} = 0.2$ and $\Gamma = 0.5$ at critical condition ($m_c = 1$, $\text{Re}_c = 116.9833$) and the total local energy $\sum_i I_i'$ (colormap). Solid (dashed) isolines indicated the positive (negative) value of the streamwise perturbation velocity $\tilde{w}$.

Figure 5.16.: Basic state (streamlines) and Rayleigh criteria (contour) for the outlet radius ratio $\eta^{\text{out}} = 0.2$ and the radial expansion $\Gamma = 0.5$.

algebraic radius of curvature R at the given point of streamline is defined as

$$R = \frac{\| \boldsymbol{u}_0^3 \|}{(\nabla \Psi) \cdot [\boldsymbol{u}_0 \cdot \nabla \boldsymbol{u}_0]} \tag{5.1}$$

here the subscript 0 refers to the basic state and $\boldsymbol{u}_0 = (u_0, w_0, 0)^T$, the $\| \boldsymbol{u}_0 \|$ is the norm of velocity field, and Ψ refers to the stream function. Therefore, the generalized Rayleigh criterion

is defined as

$$\delta = \frac{\| \, \boldsymbol{u}_0 \, \| \, \omega}{R} < 0 \qquad (5.2)$$

where the relative vorticity is shown by $\omega = \nabla \times \boldsymbol{u}_0$.

Figure 5.16 shows the obtained generalized Rayleigh criteria for outlet radius ratio $\eta^{\text{out}} = 0.2$ and radial expansion ratio $\Gamma = 0.5$. By comparing Fig. 5.14 and Fig. 5.16, it is obvious that in the area where the total energy production is maximum (at locus $(z_{\max}, r_{\max}) = (5.8334, 0.8281)$), $\delta \not< 0$. Therefore, in this case, the instability can not be centerifugal in nature.

(a)

(b)
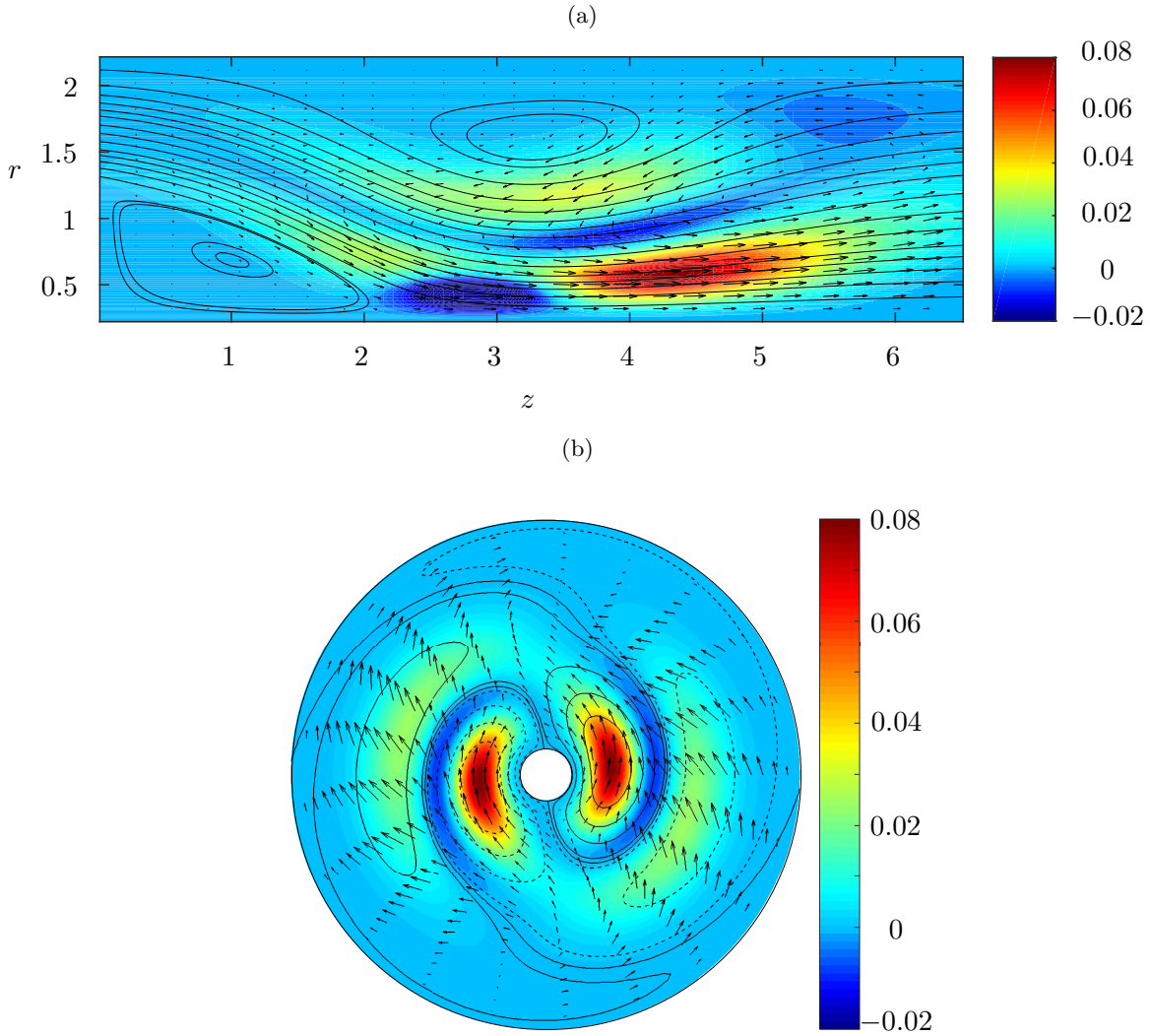
Figure 5.17.: Basic state (streamlines), critical velocity field (vectors) and the total local energy production $\sum_i I_i'$ (colormap) for $\eta^{\text{out}} = 0.1$ and expansion ratio $\Gamma = 0.5$. Shown are the (r, z) plane through the locus $(r_{\max}, z_{\max}, \phi_{\max}) = (0.5830, 4.2530, 1.9777\pi)$ at which the total local energy production takes its global maximum (a) and the corresponding (r, ϕ) plane (Solid (dashed) isolines indicated the positive (negative) value of the streamwise perturbation velocity $\tilde{w}$)(b).

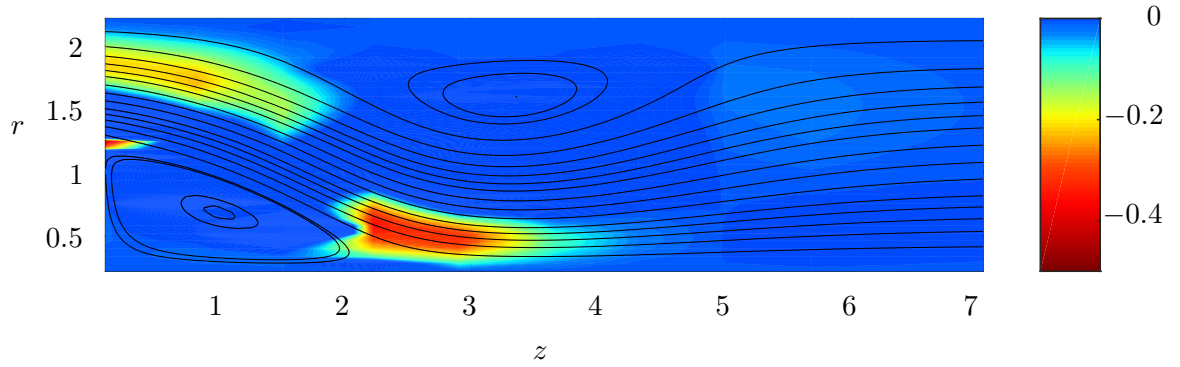For the outlet radius ratio $\eta^{\text{out}} = 0.1$ and $\Gamma = 0.5$, the basic flow (streamlines), the total local energy transfer rate (colormap) and the critical velocity field (vectors) in the (r, z) plane at which the total local energy production takes its global maximum are shown in Fig. 5.17(a). It can be seen that the total local energy production takes its maximum at $(r_{\max}, z_{\max}) = (0.5830, 4.2530)$ where the annular jet widens and decelerates (I_4') due to the reattachment of the outer recirculation zone. The lift-up effect (I_2') also has an important role and helps the instability acting on the shear layer slightly outside of the separating streamline of outer recirculation zone and downstream near to the inner cylinder where there is a high shear gradient. Downstream of the recirculation zone that is located on the outer cylinder, perturbations at the critical mode form the streamwise vortex which is centered near the separating streamline. Figure 5.17(b) shows the critical mode (vectors) and the total local energy production at the station $z_{max} = 4.2530$. It is clearly seen that the perturbations are displace the recirculation zone on the outer cylinder in the azimuthal direction. The critical mode is oscillatory with $m_c = 1$ and it rotates in the counterclockwise direction with the angular frequency $\omega_c = 0.1247$. The wave rotates such that spirals characterized by $\tilde{w} = 0$ spiral outwards in the plane shown in Fig. 5.17(b).

Variation of the expansion ratio Γ for $\eta^{\text{out}} = 0.1$

In this section a three-dimensional linear stability analysis is performed for a fixed outlet radius ratio $\eta^{\text{out}} = 0.1$ and for the expansion ratios in the range $\Gamma \in [0.25, 0.75]$. The most dangerous modes for $\eta^{\text{out}} = 0.1$ have a small wave number m. Therefore, the most dangerous modes for the wave numbers in the range $m \in [0, ..., 8]$ are computed. Neutral curves for the integer azimuthal wave numbers in the range $m \in [1, ..., 8]$ are shown in Fig. 5.18, where the wave number is indicated by symbol type and full and open symbols indicate stationary and oscillatory modes, respectively.

A complicated behaviour is observed. For $m = 1$, by increasing the expansion ratio Γ from 0.25, the oscillatory neutral mode destabilize and intersects with another oscillatory mode with $m = 1$ at $\Gamma = 0.325 \pm 0.004$. By further increase of the expansion ratio, the neutral Reynolds number of the oscillatory mode exhibit a minimum at the step height $\Gamma = 0.53 \pm 0.009$. The oscillatory mode with $m = 1$ change its nature to stationary when the expansion ratio is $\Gamma = 0.625 \pm 0.005$. For $m = 2$, by increasing the expansion ratio from $\Gamma = 0.25$, the oscillatory neutral mode destabilize and exhibit a minimum at $\Gamma = 0.4 \pm 0.04$. By further increase of the step height, another mode with $m = 2$ which is stationary intersects with the oscillatory mode at $\Gamma = 0.535 \pm 0.004$ and become neutral for larger expansion ratios. By increasing the expansion ratio from $\Gamma = 0.54$ the stationary neutral mode destabilize and it shows a minimum at $\Gamma = 0.71 \pm 0.009$.

For $m = 3$, the neutral mode for the expansion ratios in the range $\Gamma \in [0.25, 0.341]$ is stationary and exhabits a minimum at $\Gamma = 0.33 \pm 0.009$. By a further increase of Γ, the neutral mode changes its character by turning oscillatory (dotted lines and $\triangledown$) with a frequency increasing from zero at $\Gamma = 0.345 \pm 0.004$. Another oscillatory mode intersects with this mode at $\Gamma = 0.545 \pm 0.004$ and become the neutral mode for larger step heights. For $m = 4$, the stationary neutral mode
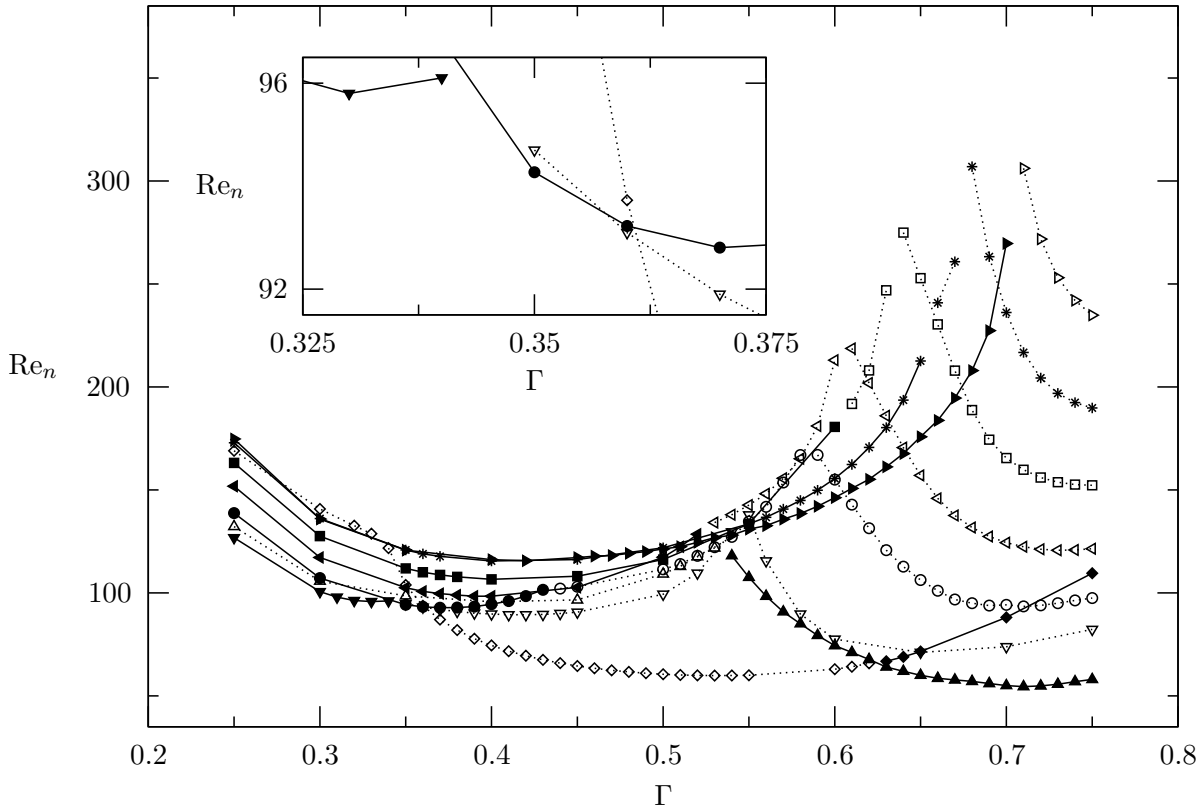
Figure 5.18.: Neutral Reynolds numbers Re_n as functions of step height Γ for $\eta^{\mathrm{out}} = 0.1$ and wave numbers $m = 1$ ($\diamond$), 2 ($\triangle$), 3 (∇), 4 ($\circ$), 5 ($\triangleleft$), 6 ($\square$), 7 ($\ast$), and 8 ($\triangleright$). Stationary instabilities are shown by solid lines and full symbols. Oscillatory instabilities are represented by dotted lines and open symbols.

for the expansion ratios in the range $\Gamma \in [0.25, 0.43]$ exhabits a minimum at $\Gamma = 0.37 \pm 0.009$. The stationary neutral mode change its nature to oscillatory at $\Gamma = 0.435 \pm 0.004$. By increasing the expansion ratio from $\Gamma = 0.44$, the oscillatory neutral mode stabilize and intersects with another oscillatory mode with $m = 4$ at $\Gamma = 0.585 \pm 0.004$. By further increase of the expansion ratio, the neutral Reynolds number of the oscillatory mode exhibit a minimum at the expansion ratio $\Gamma = 0.69 \pm 0.009$.

For higher wave numbers $m = 5$, 6, 7, similar trend for the neutral curves is obtained. For small and medium expansion ratios the neutral mode is stationary however, by increasing the expansion ratio the neutral mode change its nature to oscillatory with a frequency increasing from zero at expansion ratios in the range $\Gamma \in [0.52, 0.66]$ depending on the wave number. This behaviour is due to merging of two real eigenvalues and consequently turning to two complex ones along the neutral curves for the wave numbers $m = 5$, 6 and 7. However, these modes never become critical in the range of considered expansion ratios. By further increase of the step height, depending on the wave number at the expansion ratio in the range $\Gamma \in [0.60, 0.68]$, this neutral mode intersect with another mode with the same wave number m which is oscillatory.

For $m = 8$, the neutral mode is stationary for the expansion ratios in the range $\Gamma \in [0.25, 0.7]$ and exhibits a minimum at $\Gamma = 0.42 \pm 0.019$. By further increase of the step height another

mode which is oscillatory intersects with this stationary mode at $\Gamma = 0.705 \pm 0.004$ and become neutral for larger expansion ratios.

The two dimensional linear stability analysis ($m = 0$) is also performed for $\Gamma \in [0.25, 0.75]$ with increments of $\Delta\Gamma = 0.05$ up to the Re $= 1200$ which is three times of the largest neutral Reynolds number Re_n that we found for three dimensional stability analysis. The results showed that the axisymmetric perturbations are never critical for the parameters considered.

Γ	Re_c	m_c	$\pm\omega_c$
0.25	126.7841	3	0
0.30	100.6017	3	0
0.34	96.1011	3	0
0.35	94.2707	4	0
0.36	93.0966	3	0.0409
0.40	74.5061	1	0.1710
0.45	64.5135	1	0.1495
0.50	60.4998	1	0.1247
0.55	60.0161	1	0.0958
0.60	62.9609	1	0.0590
0.65	60.0020	2	0
0.70	55.0063	2	0
0.75	57.9763	2	0

Table 5.3.: Critical parameters for $\eta^{\mathrm{out}} = 0.1$ and different step heights Γ.

By the envelope of the neutral curves for all wave numbers, the critical parameters are obtained. As shown in Fig. 5.18 at expansion ratios in the range $\Gamma \in [0.25, 0.341]$ the neutral curves are quite dense and the critical mode is stationary with the critical wave number $m = 3$. In the narrow range of expansion ratios $\Gamma \in [0.34, 0.37]$ four different neutral stability modes are competing to represent the critical condition (see zoom in region in Fig. 5.18). From the stationary mode with wave number $m = 3$ (solid line and $\blacktriangledown$), the critical conditions swap to a stationary mode with wave number $m = 4$ (solid line and $\bullet$), then to an oscillatory mode with wave number $m = 3$ (dotted line and $\triangledown$) and, finally, to an oscillatory mode with wave number $m = 1$ (dotted line and $\diamond$). The transitions between the critical conditions occur at $\Gamma = 0.342 \pm 0.0009$, 0.357 ± 0.0009 and 0.361 ± 0.0009, respectively. An oscillatory mode with $m = 1$ is critical in the range $\Gamma \in [0.361, 0.62]$. This critical mode exhibits a minimum at the expansion ratio $\Gamma = 0.535 \pm 0.004$. Finally, for expansion ratios in the range $\Gamma \in [0.63, 0.75]$, stationary mode with the wave number $m = 2$ become critical. This critical mode has a weak minimum at Re $= 0.715 \pm 0.004$. Table 5.3, shows the critical data including wave number m_c, Reynolds number Re_c and oscillation frequency ω_c of selected representative cases for a reference purposes.

We performed an a posteriori energy analysis, in order to understand the instability mechanisms of the obtained critical modes. Therefore, representative cases are considered and the instability mechanisms are disscussed based on the characteristics of the transfered kinetic-energy between basic flow and purturbations. Table. 5.4 represents the normalized integral energy pro-

duction rates in the bulk, the transport rate of perturbation energy through the outlet surface K^{out}, the locus $z_{\max}$ of the maximum total local energy transfer rates in a streamwise direction, the locus $r_{\max}$ of the maximum total local energy transfer rates in a radial direction, the critical wavenumber m_c, the critical Reynolds number Re_c and the critical oscillation frequency ω_c. The conservation of the kinetic perturbation energy is checked and confirmed up to 5 decimal places for all of the considered cases by substituting the obtained energy production terms from Table. 5.4 into Eq. (2.22).

Γ	0.34	0.35	0.36	0.40	0.60	0.75
$\int_V I_1' dV$	0.0130	0.0148	0.0163	0.0085	0.0193	-0.0047
$\int_V I_2' dV$	0.2402	0.1841	0.2515	0.4763	0.2729	0.2149
$\int_V I_3' dV$	0.0077	0.0139	0.0096	0.0253	0.0322	0.0409
$\int_V I_4' dV$	0.7259	0.7708	0.7089	0.4856	0.5931	0.5420
$\int_V I_5' dV$	0.0132	0.0163	0.0138	0.0043	0.0825	0.2069
K^{out}	0.0000	0.0000	0.0000	0.0000	0.0000	0.0000
$z_{\max}$	4.5541	4.4035	4.4035	4.5541	4.2530	2.2211
$r_{\max}$	0.5622	0.5504	0.6130	0.5342	0.5830	0.9235
m_c	3	4	3	1	1	1
Re_c	96.1011	94.2707	93.0966	74.5061	62.9609	57.9763
ω_c	0	0	0.0409	0.1710	0.0590	0

Table 5.4.: Normalized energy production rates for different expansion ratios Γ. $z_{\max}$ and $r_{\max}$ are the place of the maximum total local energy production in z and r direction respectively.

The magnitude of each normalized energy production term $\int_V I_i' \mathrm{d}V$ shows the importance of this integral for the instability. Moreover, destabilization of a mode shows by the positive sign, whereas stabilization effect represents with the negative sign of each integral term. The results show that, for the smaller expansion ratios Γ, the flow destabilize at relatively higher Reynolds numbers (see Fig. 5.18 and Table. 5.3). As it is shown by Fig. 5.18, four different branches depending on the expansion ratio Γ found to be critical for $\eta^{\text{out}} = 0.1$. Branch 1 with the wavenumber $m = 3$ found to be critical for the expansion ratios in the range $\Gamma \in [0.25, 0.341]$ and $\Gamma \in [0.357, 361]$. In the small range of the step heights $\Gamma \in [0.342, 0.356]$ another mode with the wave number $m = 4$ is found to be critical (branch 2). Branch 3 for which $m = 1$ is critical for the moderate expansion ratios in the range $\Gamma = [0.362, 0.62]$, while branch 4 with the wavenumber $m = 2$ become critical for larger expansion ratios.

For branch 1, two representative cases are considered. The first representative case corresponds to $\Gamma = 0.34$ and $\eta^{\text{out}} = 0.1$ for which $m_c = 3$ and the mode is stationary. We considered $\Gamma = 0.36$ and $\eta^{\text{out}} = 0.1$ as the second representative case for branch 1 for which $m_c = 3$ and the mode found to be oscillatory. Figure 5.19 shows streamlines of the basic flow (solid lines), the critical flow field (vectors), and the total local energy transfer rate $\sum_{i=1}^5 I_i'$ (colormap) in two planes through the locus at which the total local energy production takes its maximum value $(r_{\max}, z_{\max})$ for both $\Gamma = 0.34$ and $\eta^{\text{out}} = 0.1$ (Fig. 5.19(a),(c)) and $\Gamma = 0.36$ and $\eta^{\text{out}} = 0.1$ (Fig. 5.19(b),(d)).

Figures 5.19(a),(c) show that the critical mode has the wave number $m_c = 3$ and the instability is stationary in this case. Due to the elongation of the recirculation zone on the outer cylinder, the perturbation flow is aligned almost parallel to the base flow streamlines and the perpendicular perturbations $\tilde{\boldsymbol{u}}_\perp$ are weak. As expected, in this case, the most dominant integral which has destabilizing effect is $\int_V I_4' \mathrm{d}V$ (Table 5.4). Therefore, when the basic flow decelerates, $\tilde{\boldsymbol{u}}_\parallel \cdot \nabla \boldsymbol{u}_0 < 0$, the integrand $I_4' = -D^{-1} \tilde{\boldsymbol{u}}_\parallel \cdot \left(\tilde{\boldsymbol{u}}_\parallel \cdot \nabla \boldsymbol{u}_0 \right) > 0$. Hence, the deceleration of the basic flow has the destabilizing effect and acceleration would stabilize the base flow. Downstream of the recirculation zone on the inner cylinder, the base flow accelerates (dark blue region) due to the deflection of the base flow from the outer towards the inner cylinder and consequently the radial thickening of the recirculation zone on the outer cylinder. The perturbation flow looses kinetic energy in this region. Therefore the magnitude of the perturbations parallel to the streamlines $\tilde{\boldsymbol{u}}_\parallel$ reduced and stabilize the base flow in this region (dark blue shadings in Fig. 5.19(a)). Further downstream, the base flow widens gradually due to the reattachment of the recirculation zone on the outer cylinder and consequently it decelerates. The magnitude of the parallel perturbations $\tilde{\boldsymbol{u}}_\parallel$ are increased and the base flow destabilized in this region (dark red shadings in Fig. 5.19(a) and Fig. 5.19(b)). The positive (negative) value of the streamwise perturbation velocity $\tilde{w}$ is shown by solid (dashed) isolines in Fig. 5.19(b). It can be seen that the perturbation flow appears in form of periodic streaks which are azimuthally centered with the maxima of the local energy production rate. Both the positive (solid-lines) and negative (dashed-lines) contours are almost the same as he local production rate contours.

By comparing the stationary critical mode for the expansion ratio $\Gamma = 0.34$, the oscillatory critical mode for the expansion ratio $\Gamma = 0.36$ and the corresponding total energy transfer rates which are shown in Fig. 5.19(a),(c) and Fig. 5.19(b),(d) respectively, it can be seen that the two critical modes are very similar to each other qualitatively. In both cases, the dominant energy transfer rates are due to deceleration ($\int_V I_4' \mathrm{d}V$) and the second positive integral which destabilize the base flow is $\int_V I_2' \mathrm{d}V$ which corresponds to the lift-up effect (see 5.4). The only exception is that the term $I_2' = -D^{-1} \tilde{\boldsymbol{u}}_\parallel \cdot \left(\tilde{\boldsymbol{u}}_\perp \cdot \nabla \boldsymbol{u}_0 \right)$ which is typical lift-up mechanism and located in the shear layer around the separating streamline on the outer cylinder, is more remarkable for the oscillatory mode with $\Gamma = 0.36$ rather than the stationary mode with $\Gamma = 0.34$ (see Fig. 5.19). Therefore, character of the critical mode is same for $\Gamma = 0.34$ and $\Gamma = 0.36$ but the latter case becomes oscillatory with a rotation rate growing from zero at $\Gamma = 0.345 \pm 0.004$. Although I_4' which corresponds to basic flow deceleration has always the primary importance to instability along branch 1, however by increasing the expansion ratio Γ along this branch, the lift-up mechanism gains importance while the deceleration mechanism becomes weaker. Figure 5.19(d) shows that the critical mode for $\Gamma = 0.36$ and $\eta^\mathrm{out} = 0.1$ is oscillatory with $m_c = 3$ and it rotates in a clockwise direction with the angular frequency $\omega_c = 0.0409$. However, owing to relatively low oscillation frequency $omeg_c$, the asymmetry of the critical mode is weak.

As a representative case for branch 2 for which the critical mode is stationary with the critical wave number $m_c = 4$, $\Gamma = 35$ and $\eta^\mathrm{out} = 0.1$ is considered. Figure 5.20 depicted the basic flow streamlines, the critical velocity field (vectors) and the total local energy production $\sum_i I_\mathrm{i}'$ (colormap) $(r_\mathrm{max}, z_\mathrm{max}) = (0.6130, 4.4035)$ at which the total local energy production takes its
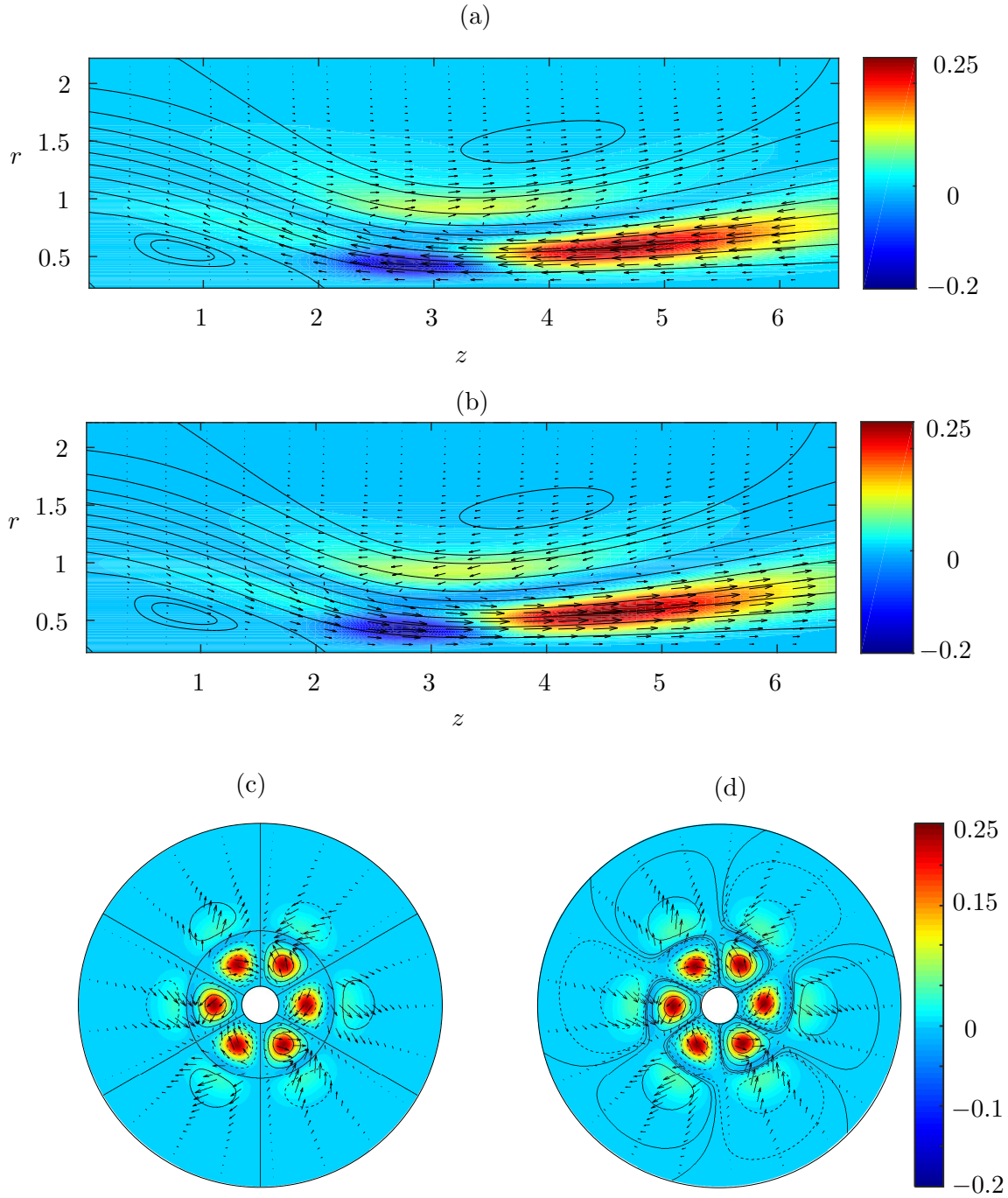
Figure 5.19.: Basic state (streamlines), critical velocity field (vectors) and total local energy production $\sum_i I_i'$ for $\eta^{\text{out}} = 0.1$ and expansion ratios $\Gamma = 0.34$ and $\Gamma = 0.36$. Shown are the (r, z) plane through the locus $(r_{\max}, z_{\max}, \phi_{\max}) = (0.5622, 4.5541, 0)$ at which the total local energy production takes its global maximum for $\Gamma = 0.34$ (a), (r, z) plane through the locus $(r_{\max}, z_{\max}, \phi_{\max}) = (0.5504, 4.4035, 0.3253\pi)$ at which the total local energy production takes its global maximum for $\Gamma = 0.36$ (b), and the corresponding (r, ϕ) plane (Solid (dashed) isolines indicated the positive (negative) value of the streamwise perturbation velocity $\tilde{w}$) for $\Gamma = 0.34$ (c) and $\Gamma = 0.36$ (d).
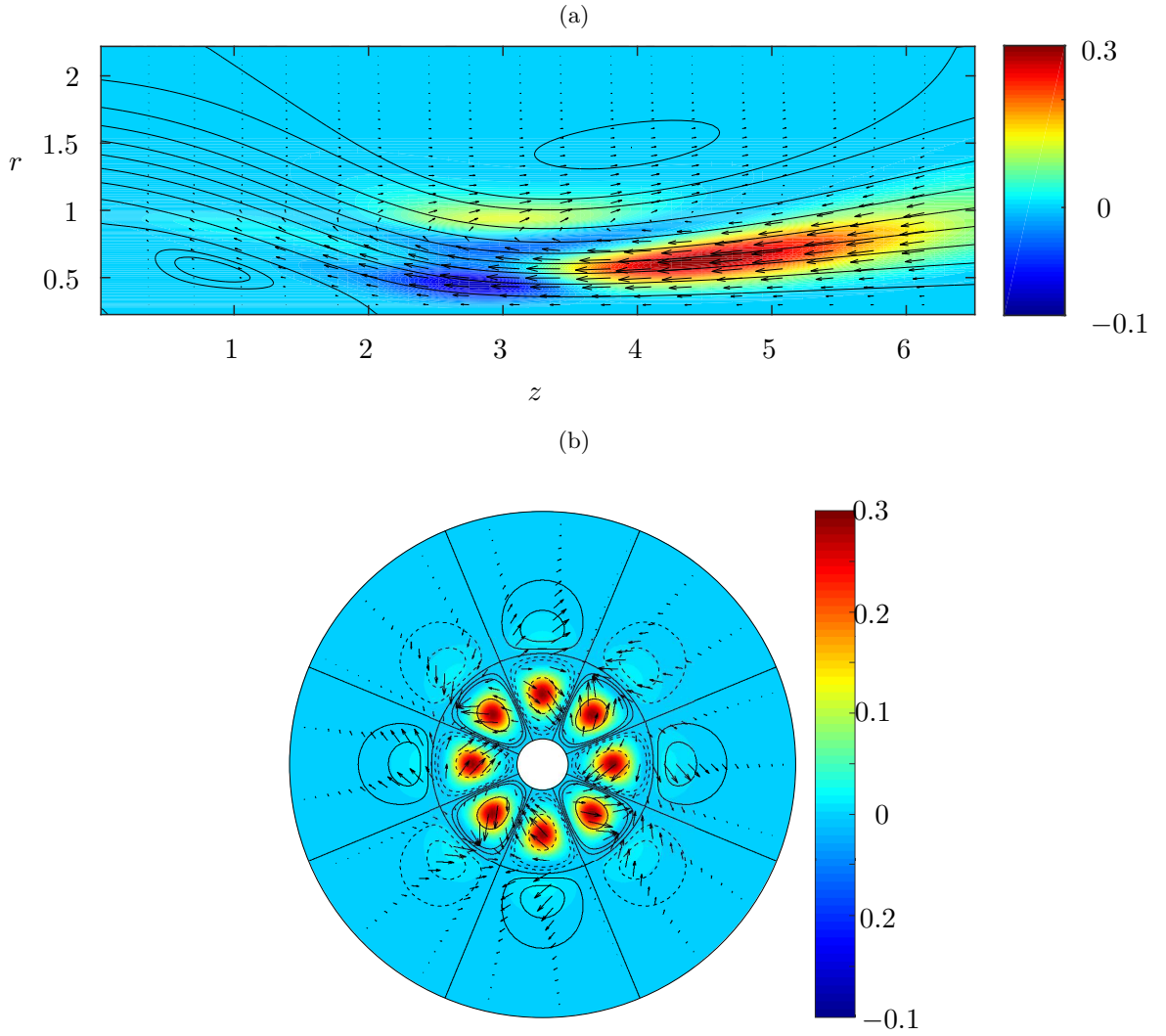
Figure 5.20.: Basic state (streamlines), critical velocity field (arrows) and the total local energy production $\sum_i I'_i$ (colormap) for $\eta^{\mathrm{out}} = 0.1$ and expansion ratio $\Gamma = 0.35$. Shown are the (r, z) plane through the locus $(r_{\max}, z_{\max}) = (0.6130, 4.4035)$ at which the total local energy production takes its global maximum (a) and the corresponding (r, ϕ) plane (Solid (dashed) isolines indicated the positive (negative) value of the streamwise perturbation velocity $\tilde{w}$)(b).

global maximum. For $\Gamma = 35$ the instability is dominated by the deceleration of the expanding annular jet on the inner cylinder. Table 5.4 also shows that $\int_V I'_4 \mathrm{d}V$ is by far dominant. It can be concluded that the mechanism of the instability along branch 2 is similar with the one along branch 1, but with $m = 4$.

To investigate the instability mechanism of the oscillatory mode with $m = 1$ which is found to be critical for the step heights in the range $\Gamma \in [0.362, 0.62]$ (branch 3), two representative cases with the expansion ratios $\Gamma = 0.40$ and 0.60 are considered.

For $\Gamma = 0.40$ and $\eta^{\mathrm{out}} = 0.1$, $\int_V I'_2 \mathrm{d}V$ and $\int_V I'_4 \mathrm{d}V$ have the most significant contributions for

Figure 5.21.: Basic state (streamlines), critical velocity field (vectors) and the total local energy production $\sum_i I'_i$ (colormap) for $\eta^{\text{out}} = 0.1$ and expansion ratio $\Gamma = 0.40$. Shown are the (r, z) plane through the locus $(r_{\max}, z_{\max}, \phi_{\max}) = (0.5342, 4.5541, 1.4609\pi)$ at which the total local energy production takes its global maximum (a) total local production $\sum_i I'_i$, (b) I'_2, (c) I'_4 and (d) the corresponding (r, ϕ) plane for total local production $\sum_i I'_i$ (Solid (dashed) isolines indicated the positive (negative) value of the streamwise perturbation velocity $\tilde{w}$). The axis are in scale.

destabilizing the basic flow (see Table. 5.4). Figures 5.21(b),and 5.21(c) show the local energy transfer from the basic state to the perturbation flow due to the contribution of terms I_2' and I_4' respectively in a plane through the locus $(r_{\max}, z_{\max}, \phi_{\max}) = (0.5342, 4.5541, 1.4609\pi)$ at which the total local energy production takes its global maximum value. It can be seen that the enery transfer to the perturbations due to I_2' which is a typical lift up mechanism arises in downstream at the shear layer outside the recirculation zone on the outer cylinder as well as the shear layer between the inner wall and the annular jet. In the latter region, the annular jet widens and decelerates ,therefore I_4' which is a typical decelaration instability mechanism has also a significant contribution of enery transfer to the perturbation flow in this region (Fig. 5.21(c)). Although $\int_V I_2' dV$ and $\int_V I_4' dV$ have nearly equal importance in the whole domain (see Table. 5.4), however, the local maximum production belong to the term I_4' being about more than twice as large as I_2' in a plane the total local energy takes its maximum. The streamlines of the basic flow, the total local energy and the critical mode (vectors) in a plane through the locus $(r_{\max}, z_{\max}, \phi_{\max}) = (0.5342, 4.5541, 1.4609\pi)$ at which the total local energy production takes its global maximum value is shown in Fig. 5.21(a). Both I_2' and I_4' terms leaves their fingerprints in the total local energy budget. It can clearly seen that a combination of the flow deceleration (I_4') where the jet expands and a lift-up mechanism (I_2') in both regions of the high shear gradient have the major contribution to the flow instability. The critical mode is oscillatory with $m_c = 1$ and it rotates in the counterclockwise direction with the angular frequency $\omega_c = 0.1710$ (Fig. 5.21(d)). The wave rotates such that spirals characterized by $\tilde{w} = 0$ spiral outwards in the plane shown in Fig. 5.21(d).

For $\Gamma = 0.60$ and $\eta^{\text{out}} = 0.1$, the dominant contributions to the energy transfer from the basic flow to the perturbations are due to I_4' and I_2' with $\int_V I_4' dV$ being almost twice as large as $\int_V I_2' dV$ (see Table. 5.4). The local energy transfer in the (r, z) plane at which the maximum total energy production occures due to the contribution of term I_2' is shown in Fig. 5.22(b) whereas the contribution of the term I_4' depicted in Fig. 5.22(c). It can be seen that the local energy transfers to the perturbations due to lift-up (I_2') occures at the upstream side of the outer recirculation region as well as in the shear layer slightly outside of the recirculation zone on the inner cylinder. However, the local energy supply to the perturbations due to the deceleration (I_4') arise in two different regions (Fig. 5.22(c)). A strong annular jet emerges from the inlet opening which is widens and consequently decelerates due to the reattachment of the inner recirculation zone. However, after the reattachment point of the recirculation bubble on the inner cylinder the basic flow confined and accelerates again due to the radial tickening of the outer separation zone. Further downstream in the region near the inner cylinder, the annular jet expands and decelerates again. The maximum production of the term I_4' is located downstream near the inner cylinder, while the maximum energy production due to I_2' arise at the upstream side of the outer recirculation zone.

Figure 5.22(a) depicted the streamlines of the basic flow, the total local energy and the critical mode (vectors) in a plane through the locus $(r_{\max}, z_{\max}, \phi_{\max}) = (0.5830, 4.2530, 1.4833\pi)$ at which the total local energy production takes its global maximum value. The largest local maxima belongs to I_4' which is reflected in the total local energy transfer. Eventhough, the
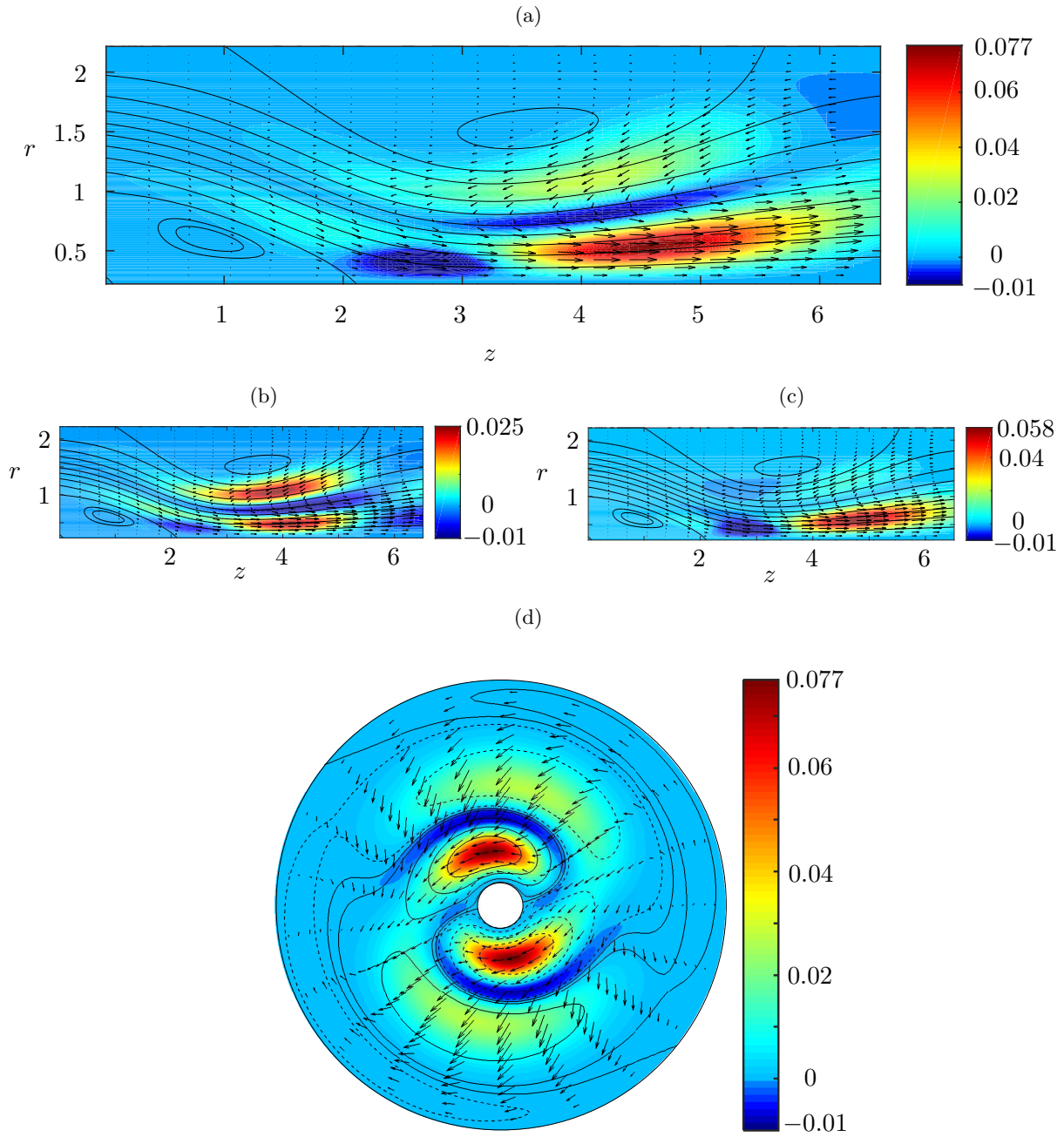
(a)

(b)

(c)

(d)
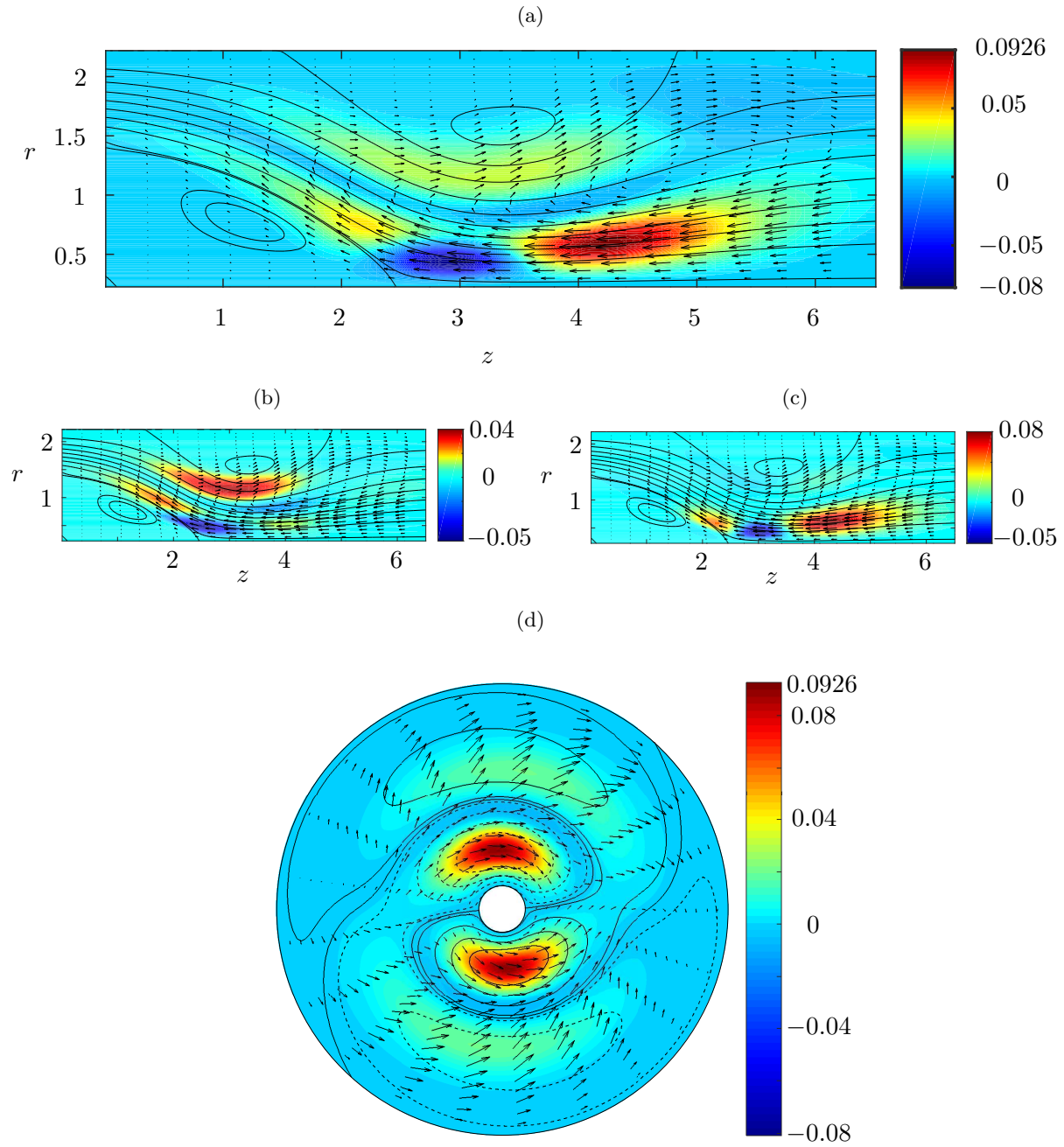
Figure 5.22.: Basic state (streamlines), critical velocity field (vectors) and the total local energy production $\sum_i I'_i$ (colormap) for $\eta^{\text{out}} = 0.1$ and expansion ratio $\Gamma = 0.60$. Shown are the (r, z) plane through the locus $(r_{\text{max}}, z_{\text{max}}, \phi_{\text{max}}) = (0.5830, 4.2530, 1.4833\pi)$ at which the total local energy production takes its global maximum (a) total local production $\sum_i I'_i$, (b) I'_2, (c) I'_4 and (d) the corresponding (r, ϕ) plane total local production $\sum_i I'_i$ (Solid (dashed) isolines indicated the positive (negative) value of the streamwise perturbation velocity $\tilde{w}$). The axis are in scale.

dominant stability mechanism is due to deceleration (I'_4) however, this instability mechanism is not the only mechanism contributes to the distabilization process. Figure 5.22(a) also shows the fingerprtint of the lift-up mechanism (I'_2) which acts on both sides of the annular jet, around the seperating streamlines where the flow exprience a high shear gradient. Although, $\int_V I'_4 \mathrm{d}V$ is the most dominant integral in the total energy budget, $\int_V I'_2 \mathrm{d}V$ is another integral which shows its maximum in the same plane and has its own fingerprint in the total local energy budget. Figure 5.22(d) shows that the oscillatory critical mode with the critical wave number $m_c = 1$ rotates in the counterclockwise direction with the angular frequency $\omega_c = 0.0590$. The wave rotates such that spirals characterized by $\tilde{w} = 0$ spiral outwards in the plane shown in Fig. 5.22(d).

At the step height $\Gamma = 0.625 \pm 0.004$ a mode with $m = 2$, which is stationary, intersects with the oscillatory mode with $m = 1$ and become the critical for larger step heights (see Fig. 5.18). To investigate the instability mechanism of the stationary critical mode with $m = 2$, we consider $\Gamma = 0.75$ and $\eta^{\mathrm{out}} = 0.1$ as the representative case along branch 4. The streamlines of the basic flow, the critical velocity field (vectors) and the total local energy (colormap) in (r, z) and (r, ϕ) planes through the locus $(r_{\max}, z_{\max}) = (0.9235, 2.2211)$ at which the total local energy production takes its global maximum value are shown in Fig. 5.23(a) and Fig. 5.24. Since the step height is larger than other considered expansion ratios, the annular jet emerges from the smaller gap. On the other hand, the recirculation zone on the outer cylinder is smaller than for smaller expansion ratios. Therefore, the annular jet widens and decelerate just before the reattachment point of the inner recirculation zone. The perturbation forms a vortex placed downstream of the recirculation zone on the inner cylinder. Therefore, the disturbance displaces the recirculation zones on the inner and outer cylinder.

For the step heigh $\Gamma = 0.75$ and $\eta^{\mathrm{out}} = 0.1$, except the $\int_V I'_1 \mathrm{d}V$ all other integrals have a destabilizing effect, however with different importance (see Table. 5.4). As it is seen in Fig. 5.23(e), for $\Gamma = 0.75$, the strongest local maxima belongs to I'_4 which is reflected in the total local energy transfer (see Fig. 5.23(a)). Table 5.4 shows that I'_4 has also the dominant integral contribution in the total local energy budget. The second dominant integral contribution and also the second local maximum of the energy production belongs to I'_2 (Table. 5.4 and Fig. 5.23(c)) which is acting on the both sides of the jet around the seperating streamlines where there is a strong shear flow. The third dominant intergral contribution corresponds to I'_5 (see Table. 5.4). However, the local contribution of I'_5 in a (r, z) plane where the total local energy production takes its global maximum is not pronounced (see Fig. 5.23(f)). On the other hand, the integral contribution of I'_1 is negative therefore has a stabilizing effect in the whole volume, however, I'_1 exhibits its local extrema in the plane where the total energy production is maximum (see Fig. 5.23(b)). As it can be seen this local maximum has its fingerprint on the total local energy production (see Fig. 5.23(a)). The integrand $I'_3 = -D^{-1}\tilde{\boldsymbol{u}}_\perp \cdot \left(\tilde{\boldsymbol{u}}_\parallel \cdot \nabla \boldsymbol{u}_0\right)$ describes the amplification of cross-stream perturbation momentum $\tilde{\boldsymbol{u}}_\perp$ by streamwise transport due to the perturbation flow $\tilde{\boldsymbol{u}}_\parallel \cdot \nabla$ of basic state momentum $\boldsymbol{u}_0$. The contribution of I'_3 is not dominant in the total local energy budget (Table. 5.4), however, this term exhibits a remarkable extrema of the local energy production (see Fig. 5.23(d)).

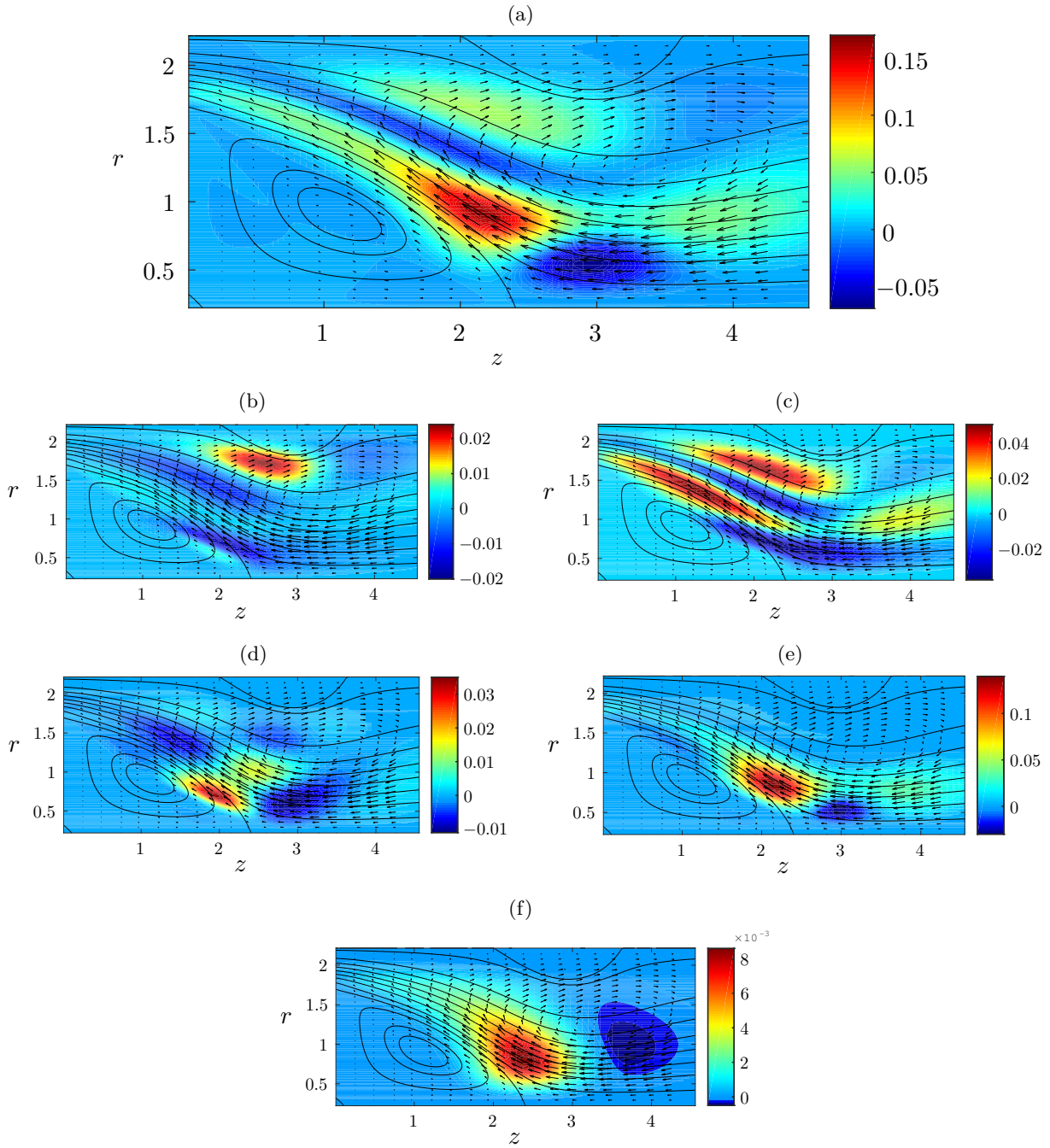Figure 5.23.: Basic state (streamlines), critical velocity field (arrows) and local energy transfer rates for $\eta^{\mathrm{out}} = 0.1$ and $\zeta = 0.75$ at the (r, z) plane with $\phi = \mathrm{const.}$ in which all energy production terms which are shown here exhibit their local maxima: (a) the total local energy production $\sum_i I'_i$, (b) I'_1, (c) I'_2 (d) I'_3 (e) I'_4 (f) I'_5
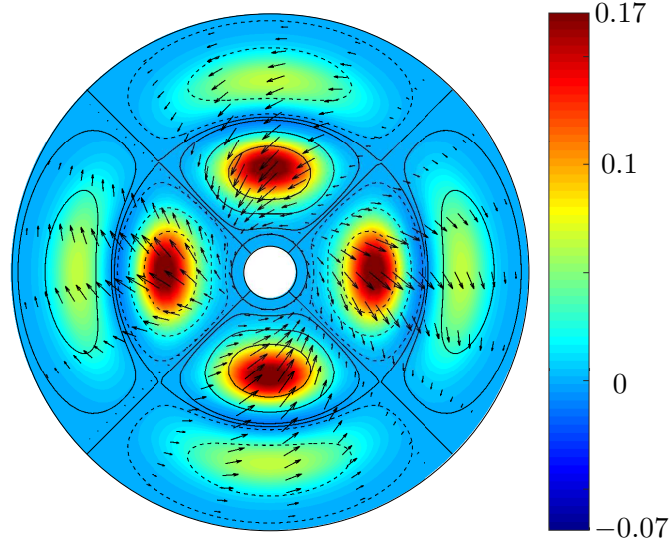
Figure 5.24.: Basic state (streamlines), critical velocity field (arrows) and the total local energy production $\sum_i I_i'$ (colormap) for $\eta^{\text{out}} = 0.1$ and the step height $\Gamma = 0.75$ in (r, ϕ) plane at the station $z_{max} = 2.2211$ where the total local energy production takes its global maximum.

5.2.2. Expansion into a simple pipe

In this section, the two and three dimensional linear stability analysis when the annular pipe transits to simple pipe is investigated for three different expansion ratios $\Gamma = 0.75$, 0.5 and 0.25. for this purpose, the inner cylinder at the outlet is completely removed. The boundary conditions for perturbation at the inlet, outlet and walls are the same as the backward-facing step annular flow. However, different boundary conditions are implemented for the axis of symmetry depending on the azimuthal wave number m (see (2.21)).

Table. 5.5 shows the obtained critical Reynolds number Re_c, the critical wave number m_c and oscillation frequency ω_c for each of the considered expansion ratios. Four different wave numbers $m = 0$, 1, 2, 3 are considered. The smallest Reynolds number Re_c which distabilize the flow corresponds to the wave number $m_c = 1$ for all three expansion ratios. The two-dimensional ($m = 0$) and three-dimensional linear stability analysis (for $m = 2$ and 3) are performed up to twice a critical value which is found for the onset of three-dimensional instability. The flow was linearly stable up to twice of the Re_c for all three expansion ratios. As it is shown in Table. 5.5, the critical mode for all three expansion ratios are stationary. It can be seen that, by decreasing the expansion ratio Γ, the critical Reynolds number also decreases.

In order to understand the instability mechanism of the critical modes for the mentioned three expansion ratios, an *a posteriori* energy analysis is performed. The normalized integral of the energy production rates in the whole volume, the energy which is advected throught the outlet surface K^{out}, the locus z_{max} of the maximum total local energy transfer rates in

Γ	Re_c	m_c	$\pm\omega_c$
0.75	184.5504	1	0
0.5	144.9611	1	0
0.25	105.4386	1	0

Table 5.5.: Critical parameters for different expansion ratios Γ.

a streamwise direction, the locus $r_{\max}$ of the maximum total local energy transfer rates in a radial direction, the critical wavenumber m_c, critical Reynolds number Re_c and the critical oscillation frequency ω_c for all three investigated cases are shown in Table. 5.6. By substituting the energy production terms (Table. 5.6) into the (2.22), the conservation of kinetic energy of the perturbation is confirmed up to 5 decimal places.

Γ	0.25	0.5	0.75
$\int_V I_1' dV$	0.1070	-1.5076	0.1181
$\int_V I_2' dV$	0.2500	3.9276	2.0019
$\int_V I_3' dV$	-0.0499	1.3229	0.1323
$\int_V I_4' dV$	0.1185	-2.2732	-1.3378
$\int_V I_5' dV$	0.5744	-0.4697	0.0855
K^{out}	0.0000	0.0000	0.0000
$z_{\max}$	0.5375	1.2625	1.6125
$r_{\max}$	0.0250	0.0833	0.0829
m_c	1	1	1
Re_c	105.4386	144.9611	184.5504
ω_c	0	0	0

Table 5.6.: Normalized energy production rates for different expansion ratios Γ. $z_{\max}$ and $r_{\max}$ are the place of the maximum total local energy production in z and r direction respectively.

The instability mechanism for $\Gamma = 0.75$

For $\Gamma = 0.75$ various instability mechanisms are present simultaneously. The computations showed that the integral energy production $\int_V I_1' dV$, $\int_V I_2' dV$, $\int_V I_3' dV$ and $\int_V I_5' dV$ are positive (Table. 5.6) and act destabilizing with $\int_V I_2' dV$ being dominant by far. The term $I_1' = -D^{-1}\tilde{\boldsymbol{u}}_\perp \cdot (\tilde{\boldsymbol{u}}_\perp \cdot \nabla \boldsymbol{u}_0)$ describes the amplification of cross-stream perturbation momentum $\tilde{\boldsymbol{u}}_\perp$ by a cross-stream transport of the basic flow $\boldsymbol{u}_0$ momentum caused by the perturbation $\tilde{\boldsymbol{u}}_\perp \cdot \nabla$. Figure 5.25(a) shows streamlines of the basic flow (solid lines), critical velocity field (vectors) and the total local energy production $\sum_i I_i'$ (colormap) in a plane through the locus $(r_{\max}, z_{\max}) = (0.0829, 1.6125)$ at which the total local energy production takes its global maximum value. Due to the small opening at the inlet, a strong annular jet of the basic flow emerges and behind the inner cylinder the basic flow is significantly deflected toward the axis which causes a flow acceleration. After the largest radial tickness of the recirculation zone on the pipe wall the basic state annular jet expands and consequently decelerates. As it is shown in Fig. 5.25(b),

the local maximum of I_1' is located in the range $z \in [1.5, 2]$, where the basic flow streamlines converge and the direction of $\boldsymbol{u}_0$ change with respect to itself in a perpendicular direction which amplifies the perpendicular perturbations. The integrand $I_2' = -D^{-1}\tilde{\boldsymbol{u}}_\parallel \cdot (\tilde{\boldsymbol{u}}_\perp \cdot \nabla \boldsymbol{u}_0)$ describes the amplification of streamwise perturbation momentum $\tilde{\boldsymbol{u}}_\parallel$ by cross-stream transport caused by the perturbation $\tilde{\boldsymbol{u}}_\perp \cdot \nabla$ of basic state momentum $\boldsymbol{u}_0$ which is the typical lift-up mechanism. This term has the largest integral contribution as destabilizing factor in the total energy budget (Table. 5.6) and also it has the strongest local extrema (Fig. 5.25(c)) which leaves its fingerprint in the total energy production (Fig. 5.25(a)).

The term $I_3' = -D^{-1}\tilde{\boldsymbol{u}}_\perp \cdot (\tilde{\boldsymbol{u}}_\parallel \cdot \nabla \boldsymbol{u}_0)$ describes the amplification of cross-stream perturbation momentum $\tilde{\boldsymbol{u}}_\perp$ by streamwise transport due to the perturbation flow $\tilde{\boldsymbol{u}}_\parallel \cdot \nabla$ of basic state momentum $\boldsymbol{u}_0$. This term exhibit its local maxima in the range $z \in [1.5, 2]$ where the jet accelerates and amplifies the perpendicular perturbations. The integrand $I_4' = -D^{-1}\tilde{\boldsymbol{u}}_\parallel \cdot (\tilde{\boldsymbol{u}}_\parallel \cdot \nabla \boldsymbol{u}_0)$ describes the streamwise transport of basic flow momentum $\tilde{\boldsymbol{u}}_\parallel \cdot \nabla \boldsymbol{u}_0$ which effects on the streamwise perturbation momentum $\tilde{\boldsymbol{u}}_\parallel$. As it is shown in Table. 5.6, the integral of I_4' is negative and act as stabilizing process. The integrand I_4' exhibits the strongest local extrema for stabilizing the basic flow in the range $z \in [1.5, 2]$ where the annular jet accelerates/decelerate and effects on the parallel perturbations (see Fig. 5.25(e)). The term $I_5' = -D^{-1}\tilde{\boldsymbol{u}}_\varphi \cdot (\tilde{\boldsymbol{u}}_\varphi \cdot \nabla \boldsymbol{u}_0)$ describes the amplification of perturbation momentum in azimuthal direction $\tilde{\boldsymbol{u}}_\varphi$ by transport of basic flow momentum in azimuthal direction due to the azimuthal perturbations $(\tilde{\boldsymbol{u}}_\varphi \cdot \nabla \boldsymbol{u}_0)$. As it shown in Table. 5.6, the contribution of $\int_V I_5' \mathrm{d}V$ in the total energy budget is not significant. The local extrema of I_5' acts also in the range $z \in [1.5, 2]$ (Fig. 5.25(f)). Therefore, the interpretation of the instability mechanism is difficult because several mechanism with different importance are present in the same region and help to destabilize the basic flow.

Due to the high curvature of the basic flow streamlines and also the dominance of the lift-up mechanism as a destabilizing factor, we suspect that the region of instability expriences the centrifugal effects. Therefore, the sufficient criterion of centerifugal instability is determined based on Sipp and Jacquin [94] and Rayleigh [84] formulation of generalized Rayleigh criterion (5.2). Figure 5.26 shows the generalized Rayleigh criterion for the expansion ratio $\Gamma = 0.75$ at the critical Reynolds number $\mathrm{Re}_c = 184.5504$. By comparing Fig. 5.25(a) and Fig. 5.26, it can be concluded that the instability is mainly due to the lift-up mechanism and expriences a centrifugal effect. In this case the most dominant term which destabilize the flow is I_2' and the largest energy production region arise due to the high shear that is present in the curved jet.

The instability mechanism for $\Gamma = 0.5$

As it is shown in Table. 5.6, for $\Gamma = 0.5$, the integral energy production $\int_V I_2' \mathrm{d}V$ and $\int_V I_3' \mathrm{d}V$ are positive and have the destabilizing effect. The term I_2' has the strongest local maxima where there exist the high shear gradient in the flow (Fig. 5.27(c)). As it mentioned before, this term is the usual lift-up mechanism where the parallel perturbations $\tilde{\boldsymbol{u}}_\parallel$ are amplified by the transport of basic state momentum $\boldsymbol{u}_0$ caused by the perpendicular perturbation $\tilde{\boldsymbol{u}}_\perp \cdot \nabla$. The second strong local maxima belongs to the term I_3' (Fig. 5.27(d)) at the place where the annular jet amplifies the perpendicular perturbations. Although integral energy production $\int_V I_1' \mathrm{d}V$

Figure 5.25.: Basic state (streamlines), critical velocity field (vectors) and the total local energy production $\sum_i I_i'$ (colormap) for expansion ratio $\Gamma = 0.75$. Shown are the (r, z) plane through the locus $(r_{\max}, z_{\max}) = (0.0829, 1.6125)$ at which the total local energy production takes its global maximum (a) total local production $\sum_i I_i'$, (b) I_1', (c) I_2', (d) I_3', (e) I_4' and (f) I_5'.

Figure 5.26.: Basic state (streamlines) and Rayleigh criteria (contour) for the expansion $\Gamma = 0.75$.

contributes as the stabilizing integral in the energy budget (Table. 5.6), however, the term I_1' shows a noticeable extrema (5.27(b)) at the location where the basic flow streamlines are highly curved, converging and change their orientation perpendicular to themselves $\tilde{\boldsymbol{u}}_\perp \cdot \nabla \boldsymbol{u}_0$ which leads to the amplification of perpendicular perturbation momentum $\tilde{\boldsymbol{u}}_\perp$ in that region. The energy budget (Table. 5.6) shows that the integral energy production $\int_V I_4' \mathrm{d}V$ has the largest contribution in the stabilizing process. By looking into the local energy production due to I_4' (5.27(e)), it can be seen that this term is locally strongly stabilizing the flow at the place where there is an acceleration of the base flow $\tilde{\boldsymbol{u}}_\parallel \cdot \nabla \boldsymbol{u}_0$ which feedback on the streamwise perturbations $\tilde{\boldsymbol{u}}_\parallel$. The term I_4' has destabilizing effect where the basic flow widens and decelerates due to the reattachment of the recirculation zone on the outer cylinder.

The integral contribution of I_5' is not dominant in the integral budget and it acts as stabilizing process in the bulk (Table. 5.6). However, the local maximum which is produced due to the term I_5' is not negligible (Fig. 5.27(f)) and it reflected in the total local energy production (Fig. 5.27(a)). The term $I_5' = -D^{-1}\left(\tilde{v}^2 u_0/r\right)$ exhibits its maximum downstream of the recirculation zone behind the disk along the axis, where the basic flow momentum transports in azimuthal direction $(\tilde{\boldsymbol{u}}_\varphi \cdot \nabla \boldsymbol{u}_0)$ which feeds back on the azimuthal perturbation $\tilde{\boldsymbol{u}}_\varphi$. Therefore, also in this case, several instability mechanism exist and work simultaneously to destabilize the basic flow.

The instability mechanism for $\Gamma = 0.25$

Figure 5.28(a), shows the streamlines for $\Gamma = 0.25$ at the critical Reynolds number $\mathrm{Re}_c = 105.4386$. In order to have a better visualization, we zoom into the part of the interest where different instability mechanism arises for this case (dashed square). Figure 5.28(b) shows streamlines of the basic flow (solid lines), critical velocity field (vectors) and the total local energy production $\sum_i I_i'$ (colormap) in a plane through at which the total local energy production takes its global maximum value in the part of the interest which is shown by the dashed square in Fig. 5.28(a). As it is shown in Fig. 5.28(b), the total local energy production has its maximum at $(r_{\max}, z_{\max}) = (0.0250, 0.5375)$ slightly above the reattachment point of the recirculation zone
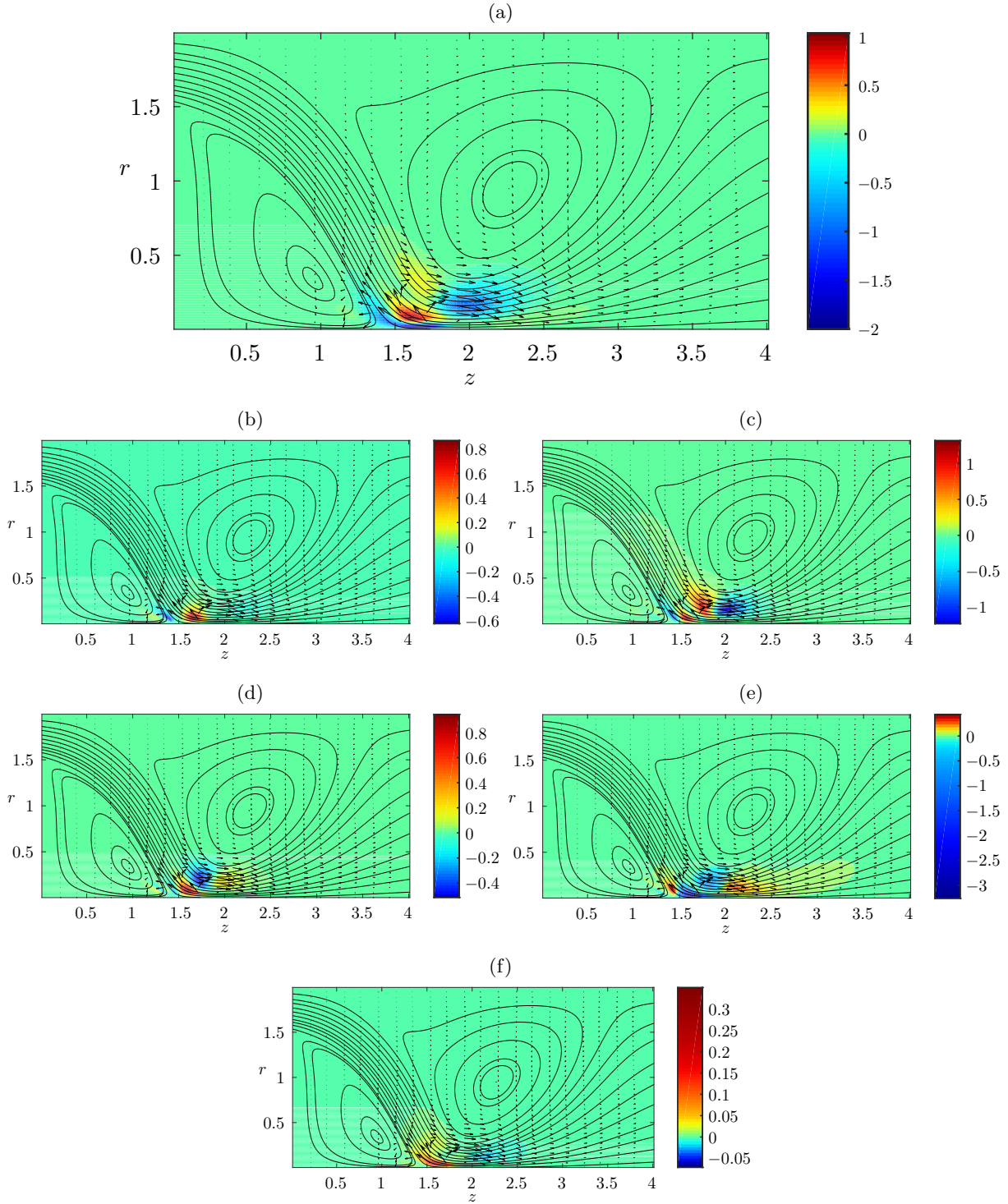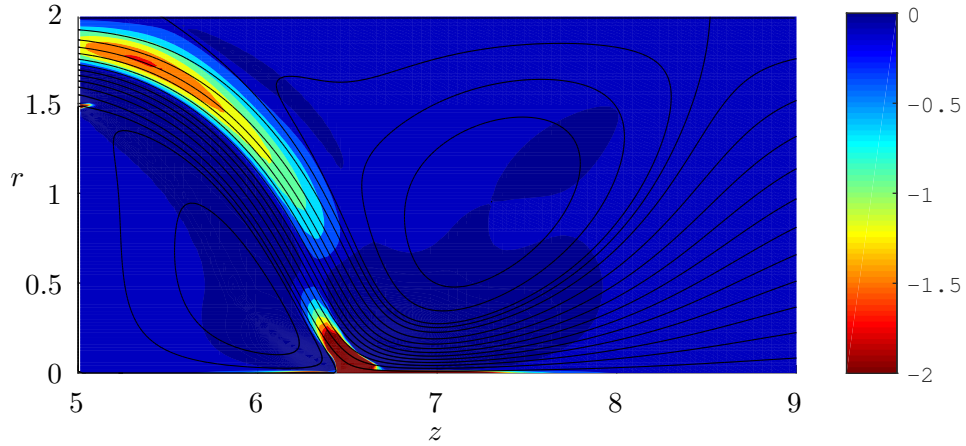
Figure 5.27.: Basic state (streamlines), critical velocity field (vectors) and the total local energy production $\sum_i I_i'$ (colormap) for expansion ratio $\Gamma = 0.5$. Shown are the (r, z) plane through the locus $(r_{\max}, z_{\max}) = (0.0833, 1.2675)$ at which the total local energy production takes its global maximum (a) total local production $\sum_i I_i'$, (b) I_1', (c) I_2', (d) I_3', (e) I_4' and (f) I_5'.

Figure 5.28.: (a) Streamlines of the annular flow expansion into a simple pipe at the critical Reynolds number $\mathrm{Re}_c = 105.4386$, basic state (streamlines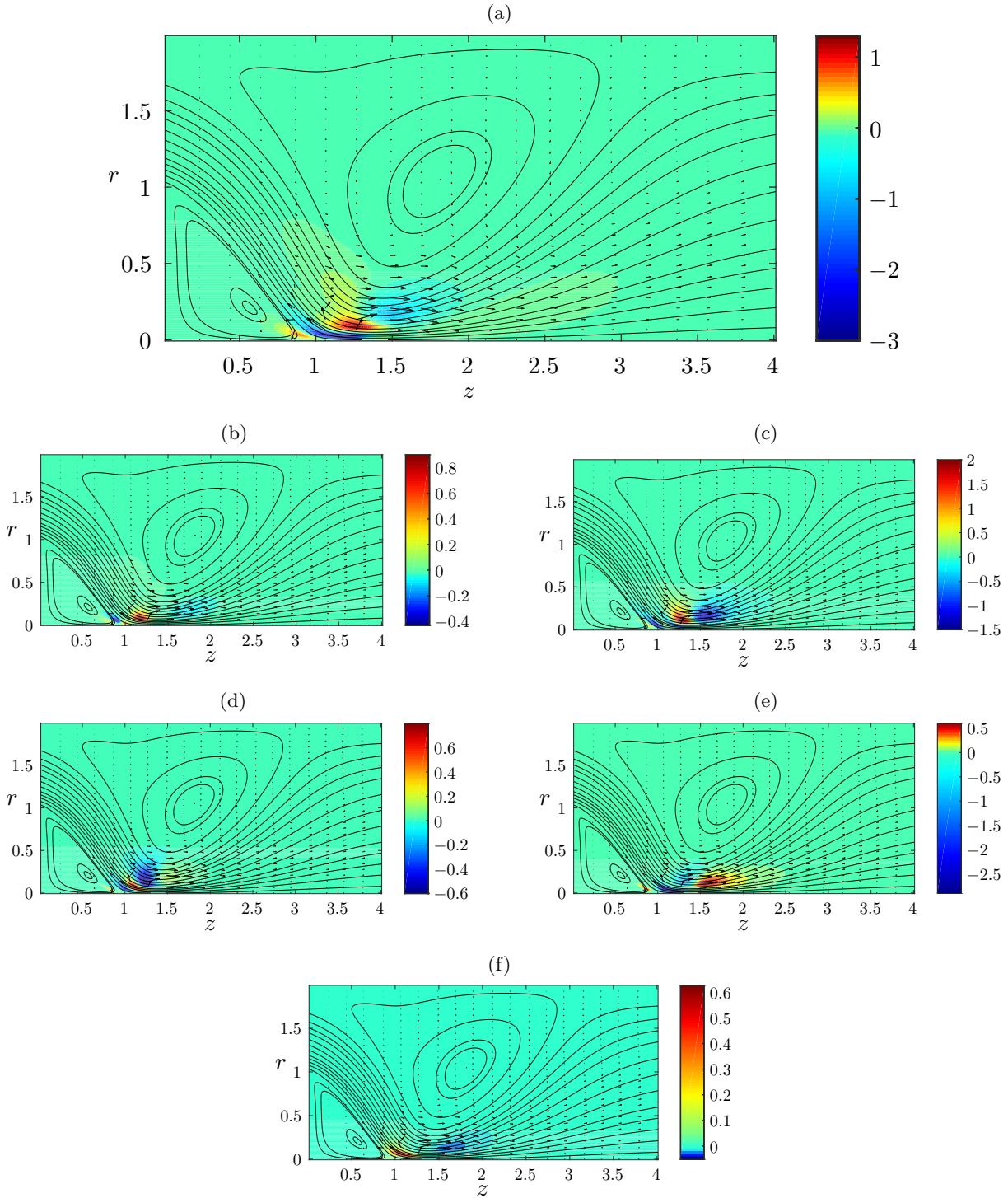), critical velocity field (vectors) and the total local energy production $\sum_i I'_i$ (colormap) for expansion ratio $\Gamma = 0.25$. Shown are the (r, z) plane through the locus $(r_{\max}, z_{\max}) = (0.0250, 0.5375)$ at which the total local energy production takes its global maximum (b) total local production $\sum_i I'_i$, (c) I'_1, (d) I'_2, (e) I'_3, (f) I'_4 and (g) I'_5.
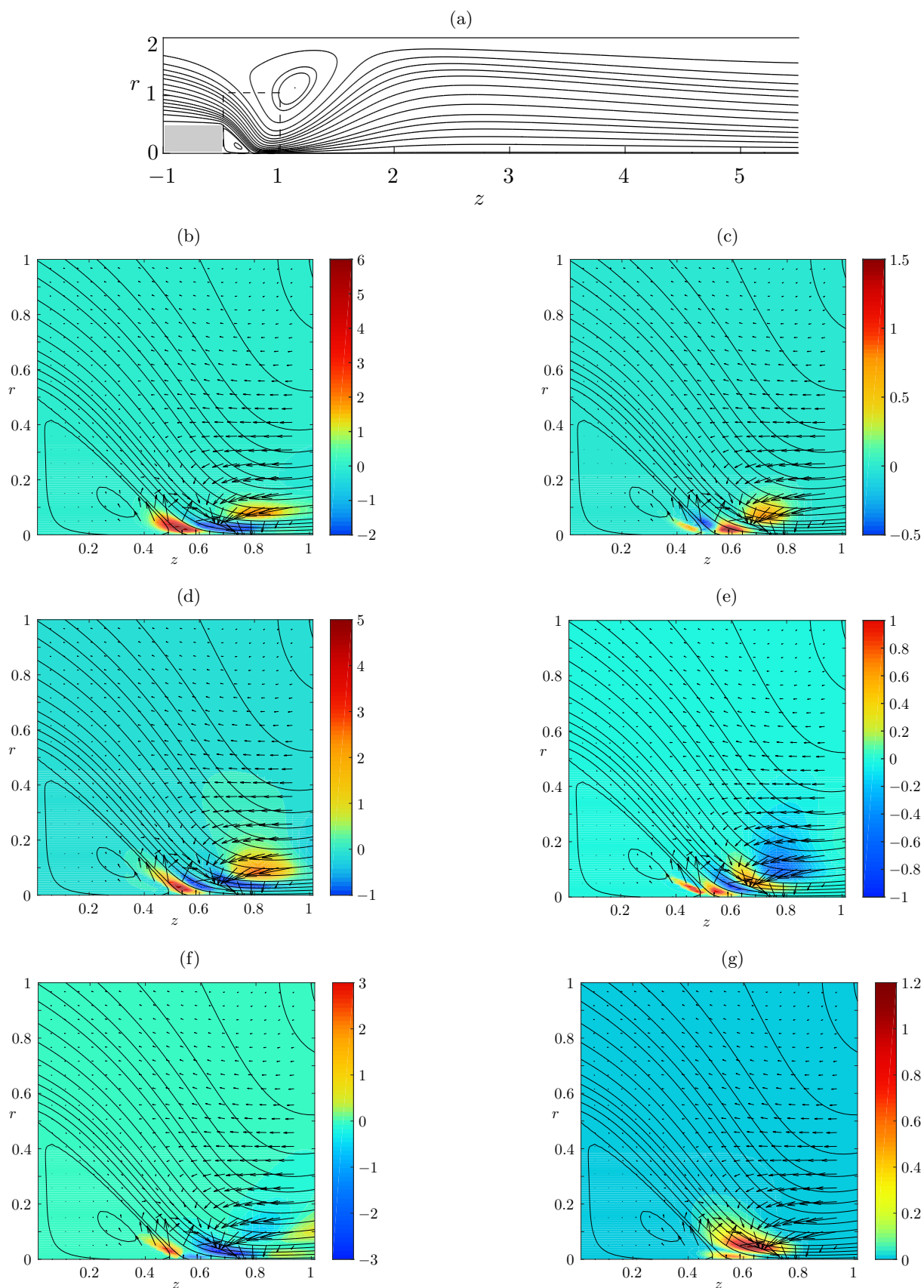
behind the disk along the axis. Table. 5.6 shows that except $\int_V I'_3 \mathrm{d}V$ all other integrals have positive sign and act as destabilizing in the energy budget. In order to have a better understanding of the instability mechanism which destabilize the basic flow, the local energy production of all energy terms are shown at the plane at which the total energy production takes its global maximum (Fig. 5.28(c)-(g)). It can be seen that, I'_2 (Fig. 5.28(d)) exhibit the strongest local maximum and I'_4 (Fig. 5.28(f)) exhibit the strongest local minimum. The maximum local energy production due to I'_2 arises downstream of the reattachment point of the recirculation zone on the axis where there is a high shear rate between the jet and the axis. The fingerprint of the energy transfer rate due to the term I'_2 which is the typical lift-up mechanism can be clearly seen in the total energy production budget (5.28(b)). The strongest minimum of the local energy production due to the I'_4 is present at the place where the jet accelerates which is feedback on the streamwise perturbation. The term I'_4 also shows the second strong maximum energy production at the reattachment point of the recirculation zone behind the inner cylinder on the axis. This destabilizing effect comes from the deceleration of the basic-flow due to the reattachment of the recirculation zone which feeds back on the parallel perturbation.

Although the $\int_V I'_2 \mathrm{d}V$ dominates as destabilizing factor in the whole volume (see Table. 5.6) however, the term I'_5 does not exhibit the strongest local maximum in the plane at which the total local energy production takes its global maximum. On the other hand, the maximum production of the integrand I'_5 is located at the same region where the annular jet accelerates strongly due to the radial tickening of the upper recirculation bubble. Therefore, the term I'_4 locally stabilize the basic flow in the same region (see Fig 5.28(f)(e)) and cause the integrand I'_5 does not leave its fingerprint on the total local energy production budget.

6. Summary and Conclusion

In the current research the pressure driven flow in an annular pipe with a backward-facing step in the radial direction and when the annular pipe transits to simple pipe have been studied. In order to find the necessary conditions for the onset of non-axisymmetric motion of the flow, a global temporal linear stability analysis considering three-dimensional perturbations has been performed to compute the critical Reynolds numbers and wave numbers. By the variation of the geometric control parameters including the Reynolds number, the outlet radius ratio (inner-to-outer radius ratio at the outlet cross section) and expansion ratio (ratio of the step height to the outlet gap), a wide range of parameter space is covered. Finally, the instability mechanisms which cause the two-dimensional flow to become three-dimensional were investigated by means of an *a posteriori* energy analysis.

In chapter 2, the governing equations for the two-dimensional basic flow as well as three-dimensional temporal linear stability problem and the pretained boundary conditions has been introduced for the considered geometries. Moreover, the governing equations for an *a posteriori* energy analysis has been derived based on the Reynolds–Orr equation for the specific set-ups of the problem.

Numerical implementation of the governing equations, together with the discretization techniques for the basic flow and linear stability problem is explained in chapter 3. The discretization process via a second-order finite volume method on a staggered grid has been employed. To solve the algebraic equations, Newton-Raphson method, polynomial line-search strategy and the arclength continuation method are used. The eigenvalues are computed by means of an implicitly restarted Arnoldi algorithm which is provided by ARPACK software library and is implemented with eigs command in MATLAB. In addition, Cayley transformation is employed to assure that the eigenvalue with the smallest real part is not missed.

chapter 4 presented the validation tests of the developed finite volume solver for the basic state as well as two and three-dimensional stability problem. This chapter also showed the grid dependency test of calculated critical Reynolds number and brought the results of the independence study for the inlet/outlet lenghts, upstream and downstream of the step, respectively.

In chapter 5 the main results of this study have been shown and discussed. This chapter comprises of two main sections. In section 5.1, the two-dimensional incompressible Newtonian flow over a radially inward backward-facing step in an annular pipe has been computed for a range of outlet radius ratios η^{out}, expansion ratios Γ and Reynolds numbers Re. In addition, the axisymmetric flow in an annular pipe which transits to the simple pipe is calculated for three different expansion ratios $\Gamma = 0.75$, 0.5 and 0.25 as a function of the Reynolds number. In the section 5.2, the stability boundaries for the range of different geometric control parameters including the outlet radius ratio and the expansion ratio have been computed for the considered

set-ups and the underlying instability mechanism have been found and explaind by means of an *a posteriori* energy analysis.

In the first part of section 5.1, the outlet radius ratio is varied in the range $\eta^{\text{out}} \in [0.1, 0.5]$ while the expansion ratio is fixed to $\Gamma = 0.5$. The results show that the Reynolds number at which the flow starts to separate from the outer cylinder decreases as the outlet radius ratio η^{out} decreases which is the indication of stronger flow separation on the outer cylinder for the smaller inner radius R_i^{out} of the outlet. In fact, for $\eta^{\text{out}} < 0.3$ the jet emerging from the narrow upstream annulus into the wider downstream annulus remains attached to the inner cylinder for a long distance downstream of the step. This is accompanied with the separation zone on the outer cylinder being elongated in downstream direction. As result further separation zones arise nested inside the separation zone defined by the streamline separating first from the outer cylinder. Moreover, owing to the intense flow inside the stretched separation zone on the outer wall co-rotating vortices resembling Kelvin's cat's eyes arise inside the separation zone.

In the second part of the section 5.1, the incompressible Newtonian flow in an annular pipe suddenly expanding radially inward is calculated numerically for outlet radius ratios $\eta^{\text{out}} = 0.1$ while the radial expansion ratio is varied in the range $\Gamma \in [0.25, 0.75]$. The results revealed that beyond the Reynolds number at which the recirculation bubble is created on the outer cylinder the growth with Re of the length of the recirculation zone on the inner outlet cylinder does not change linearly. For small and moderate expansion ratios, a single vortex and also a viscous eddy arise behind the step on the inner cylinder. However for large expansion ratios, a separation bubble nested into the original recirculation region appears. Therefore, owing to the strong strain in the vortex, single vortex splits into several vortices. By increasing the expansion ratio, the original separation zone on the outer cylinder grows in the radial direction while it shrinks axially. Moreover, the single vortex splits into co-rotating vortices for bigger expansion ratios and nested separation zones arise. For large expansion ratios, by increasing the Reynolds number, a strong annular jet creates due to the radial thickening of the vortical structure on the outer cylinder along with displacing the separation point upstream.

Finally in the third part of the section 5.1 the axisymmetric flow in an annular pipe which expands into the simple pipe is calculated numerically for three different expansion ratios $\Gamma = 0.75, 0.5$ and 0.25. The results showed that the annular jet immediately deflected from the outer cylinder and enters the wider pipe behind the disk which cause a seperation zone arise at the pipe wall. By increasing the Reynolds number, this recirculation zone grows rapidly in the radial direction which causes the jet accelerates at first and contracts when turning radially inward. After the longest radial width of the outer recirculation zone on the pipe wall the basic state annular jet expands and decelerate strongly. Therefore, the boundary layer on the pipe wall decelerates and grows in a radial direction rapidly, and it separates again from the pipe wall. By further increase of the Reynolds number, the second recirculation zone on the pipe wall grows in both radial and axial directions. The recirculation zone on the pipe wall is moving toward upstream. This effect is more pronounced for smaller expansion ratios.

In the first part of subsection 5.2.1, neutral curves and critical modes were calculated for the flow over a backward-facing step in an annular pipe as a function of the outlet radius ratio η^{out}

while the expansion ratio has been fixed to $\Gamma = 0.5$. A pronounced clustering of neutral modes for small radius ratios have been found. The critical mode for outlet radius ratios $\eta^{\mathrm{out}} \leqslant 0.27$ is oscillatory with the azimuthal wave number $m = 1$, whereas for larger outlet radius ratios, the critical mode is stationary with an azimuthal wave number $m = 6$. An *a posteriori* kinetic energy transfer analysis shows that for the large outlet radius ratios e.g. for $\eta^{\mathrm{out}} = 0.5$ the kinetic energy supply to the perturbation within the shear layer on both sides of the annular jet which is formed in the basic flow just behind the backward-facing step. As a result, lift-up mechanism creates slow and fast streaks alternating in azimuthal direction. For outlet radius ratios in the range $\eta^{\mathrm{out}} \in [0.275, 0.4]$, the critical mode with the wave number $m_c = 6$ remains same, however deceleration of the annular jet downstream become more dominant than lift-up mechanism and leads to an instability.

In the second part of subsection 5.2.1, global linear stability analysis was performed for the flow over a backward-facing step in an annular pipe for a range of non-dimensional step heights Γ while outlet radius ratio has been fixed to $\eta^{\mathrm{out}} = 0.1$. The two dimensional linear stability analysis shows that the flow over an annular backward facing step is linearly stable up to Re = 1200 for the investigated range of expansion ratios. By the envelope of the neutral curves, the critical parameters were obtained. A mode with the wavenumber $m = 3$ found to be critical for the expansion ratios in the range $\Gamma \in [0.25, 0.341]$ and $\Gamma \in [0.357, 361]$. This mode is stationary for small expansion ratios however, it changes its character by turning to oscillatory with the frequency increasing from zero at $\Gamma = 0.345 \pm 0.004$. In the narrow range of the step heights $\Gamma \in [0.342, 0.356]$ another mode with the wave number $m = 4$ which is stationary becomes critical. For the moderate expansion ratios in the range $\Gamma = [0.362, 0.62]$, an oscillatory critical mode with $m = 1$ has been found whereas, another mode with the wavenumber $m = 2$ which is stationary becomes critical for larger step heights. An *a posteriori* energy analysis showed that deceleration of the basic flow with the support of the lift-up mechanism are the most important mechanisms to the instability. For small and moderate step heights Γ, the deceleration of the basic flow downstream in the region near the inner cylinder where the annular jet expands decelerates which leads to instability. For large expansion ratios ($\Gamma \geqslant 0.63$), the instability mechanism is still dominated by flow deceleration however, the energy transfer to the perturbation arises in a different region of the flow. Since, the annular jet emerges from the smaller opening when the step height is large, the expansion of the jet into the wider annulus dominates its acceleration and the energy transfer due to deceleration occures in the jet before the reattachment of the inner recirculation zone.
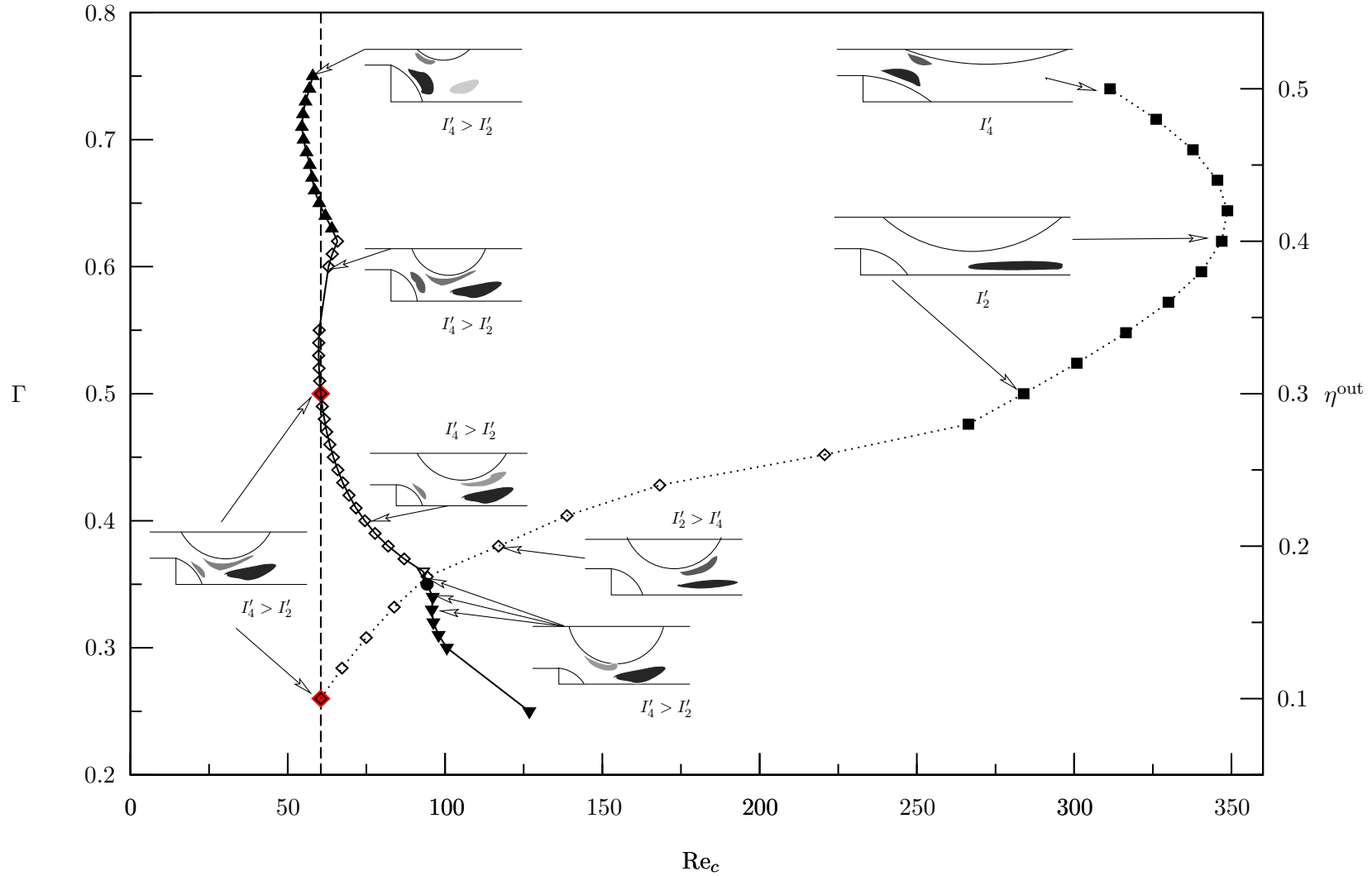
Figure 6.1.: The stability boundary for constant radius ratio $\eta^{\mathrm{out}} = 0.1$ as a function of the step height Γ (solid line) and for fixed step height $\Gamma = 0.5$ as a function of radius ratio η^{out} (dotted line). Symbol type shows the critical wave number: wave numbers $m = 1$ ($\diamond$), 2 ($\triangle$), 3 (∇), 4. Stationary instabilities are shown by full symbols. Oscillatory instabilities are represented by open symbols.

Figure 6.1 summarizes $(\Gamma, Re_c, \eta^{\text{out}})$ parameter space which were investigated in this study. Dotted curve shows the calculated critical Reynolds numbers as a function of outlet radius ratio η^{out} considering constant step height $\Gamma = 0.5$ whereas the solid curve denotes the computed critical Reynolds number as a function of the step height Γ for a constant outlet radius ratio $\eta^{\text{out}} = 0.1$. The critical wave numbers shown by symbol type. Full and open symbols show stationary and oscillatory instabilities respectively. The sketch of different instability scenarios is also shown in Fig. 6.1 for representative cases. The black regions in each sketch shows the locus at which the total local energy production takes its maximum value and the gray zones represent the areas where the energy transfer to the perturbation are smaller in magnitude but they are at the same order with the maximum energy production. As it is shown in Fig. 6.1, we have found both steady and oscillatory instabilities. The regions of the basic flow in which the most dangerous perturbation is supplied with kinetic energy varies with Γ and η^{out} (black zones in the sketches depicted in Fig. 6.1). In general, we have found two dominant instability mechanisms. The first one is the famous lift-up mechanism (I_2' in Fig. 6.1) which arise due to the shear gradient in the basic flow. In this mechanism the cross-stream transport of basic flow momentum amplifies the streamwise perturbation momentum. As a result, the fluid is lift-up from the low velocity areas and intercts with high velocity regions and the three dimensional perturbation is evolved into streaks. The other mechanism occures due to the deceleration (I_4' in Fig. 6.1) of the basic state in which the streamwise transport of basic flow momentum amplifies the streamwise perturbation momentum. Since the considered set-up is very long and the inner recirculation zone is short, the basic annular wall jet expands and decelerates downstream of the short separation zone on the inner cylinder. This makes the deceleration mechanism very important for the current set-up. Comparing the instability of the flow in the present geometry with the instability of the flow over a backward-facing step in plane channel [10, 60], the wall jet arised upon the impingement on the inner cylinder behind the inner recirculation zone can be much thinner in the annular geometry. As a result, deceleration of the basic state play a much more important role in the annular set-up.

The critical mode for the flow in an annular pipe which expands into the simple pipe for three different expansion ratios $\Gamma = 0.75, 0.5, 0.25$ was calculated (subsection 5.2.2). For all three cases, a mode with the wavenumber $m = 1$, which is stationary was found to be critical. An *a posteriori* energy analysis shows that lift-up mechanism has a significant role to instability and energy transfer to the perturbations arise on the downstream side of the jet where the centrifugal forces are significant.

This study succeeded to increase the understanding of the underlying physical mechanisms of the critical mode in which an axisymmetric flow becomes unstable to three dimensional perturbation mode. The limitation of this study is that it only investigates the linear instabilities of the flow over backward-facing step in an annular pipe and finite amplitude perturbations are not considered. In this thesis, we investigated a simplified case to conceptually understand the role of geometric discontinuity in annular pipe flows. However, in order to investigate real engineering systems which are more complex, we need to include the other effects in order to make our model nearer to the real problem. Therefore, the current results arise many interesting

problems and open questions. Considering the drill strings, since the crude oil is a non-Newtonian fluid, the problem under consideration can be extended by investigating the behaviour of non-Newtonian fluid in the same geometry. It would also be worthwhile to consider the effect of inner cylinder rotation since the drill pipe and the drill colar are not stationary in the reality. In order to investigate the flow in heat-exchangers, including the effect of heat transfer and buoyancy would be an interesting extension of the present study.

As it is mentioned in the introduction, flow induced vibrations in most engineering systems arise in flexible structures at high Reynolds number, unsteady and seperated flows. Therefore, the current results also arise interesting open questions. First of all, it would be interesting to perform time dependent simulations considering the same boundary conditions imposed in this study. Moreover, future studies might perform the Direct Numerical Simulations (DNS) to investigate the transition from laminar to fully turbulent flow. The applied method in this thesis cannot grab higher order nonlinear interaction of the modes, therefore performing the perturbation analysis in order to investigate the dominant nonlinear effects of higher orders is also of interest. Finally, in order to have a practical engineering tool, it is useful to develop a CFD code which can calculate the structure response to the flow with high Reynolds number.

A. Derivation of the Reynolds–Orr equation

The scalar product of the perturbation velocity vector $\tilde{\boldsymbol{u}}$ with the linear perturbation equations (2.16a)–(2.16d) followed by the integration over the annular volume V yields

$$\frac{1}{2}\partial_t \left\langle \tilde{\boldsymbol{u}}^2 \right\rangle + \left\langle \tilde{\boldsymbol{u}} \cdot (\boldsymbol{u}_0 \cdot \nabla \tilde{\boldsymbol{u}}) \right\rangle + \left\langle \tilde{\boldsymbol{u}} \cdot (\tilde{\boldsymbol{u}} \cdot \nabla \boldsymbol{u}_0) \right\rangle = \frac{1}{\mathrm{Re}} \left\langle \tilde{\boldsymbol{u}} \cdot \nabla^2 \tilde{\boldsymbol{u}} \right\rangle - \left\langle \tilde{\boldsymbol{u}} \cdot \nabla \tilde{p} \right\rangle \tag{A.1}$$

where $\langle ... \rangle = \int_V ...\mathrm{d}V$. The first term of equation (A.1) is temporal change of kinetic energy $1/2\partial_t \left\langle \tilde{\boldsymbol{u}}^2 \right\rangle = \partial E^{\mathrm{kin}}/\partial t$. In order to obtain the Reynolds–Orr equation for the considered geometry, the boundary conditions and continuity equation ($\nabla \cdot \tilde{\boldsymbol{u}} = 0$) were considered and each term of the equation (A.1) splits into the volume and surface integrals. Therefore the integral of the non-linear term $\int_V \tilde{\boldsymbol{u}} \cdot (\boldsymbol{u}_0 \cdot \nabla \tilde{\boldsymbol{u}})\mathrm{d}V$ is equal to

$$\int_V \tilde{\boldsymbol{u}} \cdot (\boldsymbol{u}_0 \cdot \nabla \tilde{\boldsymbol{u}})\mathrm{d}V = \int_S \tilde{\boldsymbol{u}}^2 \left(\boldsymbol{u}_0 \cdot e_{\mathrm{n}}\right)\mathrm{d}S - \int_V \tilde{\boldsymbol{u}}^2 \underbrace{\left(\nabla \cdot \boldsymbol{u}_0\right)}_{=0}\mathrm{d}V - \int_V \tilde{\boldsymbol{u}} \cdot \left(\boldsymbol{u}_0 \cdot \nabla \tilde{\boldsymbol{u}}\right)\mathrm{d}V$$

$$= \frac{1}{2}\int_S \tilde{w}^2 w_0 \mathrm{d}S^{\mathrm{out}} \tag{A.2}$$

where e_{n} is the unit vector which is normal to the surface and $\int_S ...\mathrm{d}S$ is the integral over the surface of the volume. Since perturbation vanishes at the inlet and all the walls ($\tilde{u} = 0$), the surface integral $\int_S \tilde{\boldsymbol{u}}^2 \left(\boldsymbol{u}_0 \cdot e_{\mathrm{n}}\right)\mathrm{d}S$ is zero everywhere except at the outlet which is shown by S^{out}.

The integral of diffusive term $1/\mathrm{Re} \int_V \tilde{\boldsymbol{u}} \cdot \nabla^2 \tilde{\boldsymbol{u}}\mathrm{d}V$ is equal to

$$D = \frac{1}{\mathrm{Re}}\int_V \tilde{\boldsymbol{u}} \cdot \nabla^2 \tilde{\boldsymbol{u}}\mathrm{d}V = \frac{1}{\mathrm{Re}}\left[\int_S \underbrace{\tilde{\boldsymbol{u}} \cdot [(e_{\mathrm{n}} \cdot \nabla)\,\tilde{\boldsymbol{u}}]}_{=0}\mathrm{d}S - \int_V (\nabla \tilde{\boldsymbol{u}})^2\,\mathrm{d}V\right]$$

$$= -\frac{1}{\mathrm{Re}}\left[\int_V (\nabla \times \tilde{\boldsymbol{u}})^2\,\mathrm{d}V + \int_S \tilde{\boldsymbol{u}}\,(e_{\mathrm{n}} \cdot \nabla \tilde{\boldsymbol{u}})\,\mathrm{d}S\right] \tag{A.3}$$

$$= -\frac{1}{\mathrm{Re}}\left[\int_V (\nabla \times \tilde{\boldsymbol{u}})^2\,\mathrm{d}V + \int_S \left(\tilde{u}\partial_r \tilde{w} + \underbrace{\frac{\tilde{v}}{r}\partial_\phi \tilde{w}}_{=0} + \underbrace{\tilde{w}\partial_z \tilde{w}}_{=0}\right)\mathrm{d}S^{\mathrm{out}}\right],$$

here the dissipation rate $-\int_V (\nabla \tilde{\boldsymbol{u}})^2\,\mathrm{d}V$ is always negative which shows the decrease of the kinetic energy. This term is reformulated to $-1/\mathrm{Re}\left[\int_V (\nabla \times \tilde{\boldsymbol{u}})^2\,\mathrm{d}V + \int_S \tilde{\boldsymbol{u}}\,(e_{\mathrm{n}} \cdot \nabla \tilde{\boldsymbol{u}})\,\mathrm{d}S\right]$ by using a vector identity. The surface integral of the $\tilde{\boldsymbol{u}}\,(e_{\mathrm{n}} \cdot \nabla \tilde{\boldsymbol{u}})$ is written for the outlet where

S^{out} shows the surface at the outlet and is zero for all other boundaries where the perturbation velocity $\tilde{\boldsymbol{u}} = \boldsymbol{0}$ is considered to be zero.

The partial integration of the pressure is

$$\int_V \tilde{\boldsymbol{u}} \cdot \nabla \tilde{p} \, \mathrm{d}V = \int_S \underbrace{(\tilde{\boldsymbol{u}} \cdot e_{\mathrm{n}})}_{=0} \tilde{p} \, \mathrm{d}S - \int_V \underbrace{(\nabla \cdot \tilde{\boldsymbol{u}})}_{=0} \tilde{p} \, \mathrm{d}V \tag{A.4}$$

in the considered geometry Pressure perturbation $\tilde{p}$ is zero on all boundaries therefore the surface integrals on the boundaries are zero.

we decomposed the local energy transfer rates $-\tilde{\boldsymbol{u}} \cdot (\tilde{\boldsymbol{u}} \cdot \nabla \boldsymbol{u}_0)$ into different terms in both cylindrical and streamline coordinate systems. In cylindrical coordinate system the local energy production rates $-\tilde{\boldsymbol{u}} \cdot (\tilde{\boldsymbol{u}} \cdot \nabla \boldsymbol{u}_0)$ are

$$-\tilde{\boldsymbol{u}} \cdot (\tilde{\boldsymbol{u}} \cdot \nabla \boldsymbol{u}_0) = - \begin{pmatrix} \tilde{u} \\ \tilde{w} \\ \tilde{v} \end{pmatrix} \cdot \left[\begin{pmatrix} \tilde{u} \\ \tilde{w} \\ \tilde{v} \end{pmatrix} \cdot \begin{pmatrix} \partial_r u_0 & \partial_z u_0 & 0 \\ \partial_r w_0 & \partial_z w_0 & 0 \\ 0 & 0 & u_0/r \end{pmatrix} \right] \tag{A.5}$$
$$= - \left[\tilde{u}^2 \partial_r u_0 + \tilde{u}\tilde{w} \partial_z u_0 + \tilde{w}\tilde{u} \partial_r w_0 + \tilde{w}^2 \partial_z w_0 + \tilde{v}^2 \frac{u_0}{r} \right].$$

The local energy transfer rate $-\tilde{\boldsymbol{u}} \cdot (\tilde{\boldsymbol{u}} \cdot \nabla \boldsymbol{u}_0)$ normalized by the total dissipation D is decomposed into the following five terms in cylindrical coordinate

$$\begin{aligned}
I_1 &= -\frac{1}{D} \tilde{w}^2 \frac{\partial w_0}{\partial z}, & I_2 &= -\frac{1}{D} \tilde{w}\tilde{u} \frac{\partial w_0}{\partial r}, \\
I_3 &= -\frac{1}{D} \tilde{u}\tilde{w} \frac{\partial u_0}{\partial z}, & I_4 &= -\frac{1}{D} \tilde{u}^2 \frac{\partial u_0}{\partial r}, \\
I_5 &= -\frac{1}{D} \tilde{v}^2 \frac{u_0}{r}.
\end{aligned} \tag{A.6}$$

In streamline coordinates the perturbation flow is decomposed into

$$\tilde{\boldsymbol{u}} = \tilde{\boldsymbol{u}}_{\|} + \tilde{\boldsymbol{u}}_{\perp} + \tilde{\boldsymbol{u}}_{\varphi}, \tag{A.7}$$

where $\tilde{\boldsymbol{u}}_{\|}$ denotes the perturbation velocity in direction of the basic flow, $\tilde{\boldsymbol{u}}_{\perp}$ is the perturbation velocity perpendicular to the basic flow and in the (r, z) plane, and $\tilde{\boldsymbol{u}}_{\varphi}$ represents the perturbation velocities in azimuthal direction. Defining the unit vectors on (r, z) plane

$$\hat{e}_{\|} = \frac{1}{N} \begin{pmatrix} u_0 \\ w_0 \end{pmatrix} \tag{A.8}$$

$$\hat{e}_{\perp} = \frac{1}{N} \begin{pmatrix} w_0 \\ -u_0 \end{pmatrix},$$

where $N = (u^2 + w^2)^{0.5}$, the parallel, perpendicular and azimuthal perturbation velocity are

$$\tilde{\boldsymbol{u}}_\parallel = \underbrace{\left(\frac{\tilde{u}u_0 + \tilde{w}w_0}{N}\right)}_{=M} \hat{e}_\parallel,$$

$$\tilde{\boldsymbol{u}}_\perp = \underbrace{\left(\frac{\tilde{u}w_0 - \tilde{w}u_0}{N}\right)}_{=P} \hat{e}_\perp, \tag{A.9}$$

$$\tilde{\boldsymbol{u}}_\varphi = \tilde{\boldsymbol{u}}_\varphi \hat{e}_\phi.$$

Therefore, the local normalized energy transfer terms in streamline coordinate are obtained as

$$-\tilde{\boldsymbol{u}} \cdot (\tilde{\boldsymbol{u}} \cdot \nabla \boldsymbol{u}_0) = -\left[\tilde{\boldsymbol{u}}_\perp \cdot (\tilde{\boldsymbol{u}}_\perp \cdot \nabla \boldsymbol{u}_0) + \tilde{\boldsymbol{u}}_\parallel \cdot (\tilde{\boldsymbol{u}}_\perp \cdot \nabla \boldsymbol{u}_0) \right. \tag{A.10}$$
$$\left. + \tilde{\boldsymbol{u}}_\perp \cdot \left(\tilde{\boldsymbol{u}}_\parallel \cdot \nabla \boldsymbol{u}_0\right) + \tilde{\boldsymbol{u}}_\parallel \cdot \left(\tilde{\boldsymbol{u}}_\parallel \cdot \nabla \boldsymbol{u}_0\right) + \tilde{\boldsymbol{u}}_\varphi \cdot (\tilde{\boldsymbol{u}}_\varphi \cdot \nabla \boldsymbol{u}_0)\right].$$

Following the expansion of obtained five contributions which is normalized by total dissipation D is shown

$$I_1' = -\frac{1}{D}\left(\tilde{w}_\perp^2 \frac{\partial w_0}{\partial z} + \tilde{w}_\perp \tilde{u}_\perp \frac{\partial w_0}{\partial r} + \tilde{u}_\perp \tilde{w}_\perp \frac{\partial u_0}{\partial z} + \tilde{u}_\perp^2 \frac{\partial u_0}{\partial r}\right),$$

$$I_2' = -\frac{1}{D}\left(\tilde{w}_\parallel \tilde{w}_\perp \frac{\partial w_0}{\partial z} + \tilde{w}_\parallel \tilde{u}_\perp \frac{\partial w_0}{\partial r} + \tilde{u}_\parallel \tilde{w}_\perp \frac{\partial u_0}{\partial z} + \tilde{u}_\parallel \tilde{u}_\perp \frac{\partial u_0}{\partial r}\right),$$

$$I_3' = -\frac{1}{D}\left(\tilde{w}_\parallel \tilde{w}_\perp \frac{\partial w_0}{\partial z} + \tilde{w}_\perp \tilde{u}_\parallel \frac{\partial w_0}{\partial r} + \tilde{u}_\perp \tilde{w}_\parallel \frac{\partial u_0}{\partial z} + \tilde{u}_\parallel \tilde{u}_\perp \frac{\partial u_0}{\partial r}\right), \tag{A.11}$$

$$I_4' = -\frac{1}{D}\left(\tilde{w}_\parallel^2 \frac{\partial w_0}{\partial z} + \tilde{w}_\parallel \tilde{u}_\parallel \frac{\partial w_0}{\partial r} + \tilde{u}_\parallel \tilde{w}_\parallel \frac{\partial u_0}{\partial z} + \tilde{u}_\parallel^2 \frac{\partial u_0}{\partial r}\right),$$

$$I_5' = -\frac{1}{D}\left(\tilde{v}^2 \frac{u_0}{r}\right).$$

By bringing together all the introduced terms for the problem under consideration, the Reynold–Orr equation obtained as

$$\frac{1}{D}\frac{dE^{\text{kin}}}{dt} = -1 + \sum_{n=1}^{5} \int_V I_i' dV + -\frac{1}{2D}\text{Re}\int_S w_0 \tilde{w}^2 dS^{\text{out}}, \tag{A.12}$$

where E^{kin} is the total kinetic energy and D the viscous dissipation.

Bibliography

[1] Simplified sketch of a drilling rig. http://shaleintl.com/drilling-for-oil/.

[2] Albensoeder, S., Kuhlmann, H. C., and Rath, H. J. (2001). Three-dimensional centrifugal-flow instabilities in the lid-driven-cavity problem. *Phys. Fluids*, 13(1):121–135.

[3] Alderman, N. J., Gavignet, A., Guillot, D., Maitland, G. C., et al. (1988). High-temperature, high-pressure rheology of water-based muds. In *SPE Annual Technical Conference and Exhibition*. Society of Petroleum Engineers.

[4] Alleborn, N., Nandakumar, K., Raszillier, H., and Durst, F. (1997). Further contributions on the two-dimensional flow in a sudden expansion. *J. Fluid Mech.*, 330:169–188.

[5] Andereck, C. D., Liu, S. S., and Swinney, H. L. (1986). Flow regimes in a circular couette system with independently rotating cylinders. *J. Fluid Mech.*, 164:155–183.

[6] Armaly, B. F., Durst, F., Pereira, J. C. F., and Schönung, B. (1983). Experimental and theoretical investigation of backward-facing step flow. *J. Fluid Mech.*, 127:473–496.

[7] Bäck, M., Gasser, T. C., Michel, J., and Caligiuri, G. (2013). Biomechanical factors in the biology of aortic wall and aortic valve diseases. *Cardiovasc. Res.*, 99(2):232–241.

[8] Badekas, D. and Knight, D. D. (1992). Eddy correlations for laminar axisymmetric sudden expansion flows. *J. Fluids Eng.*, 114(1):119–121.

[9] Bai, Z., Demmel, J., Dongarra, J., Ruhe, A., and Van der Vorst, H. (2000). *Templates for the solution of algebraic eigenvalue problems: a practical guide*, volume 11. SIAM.

[10] Barkley, D., Gomes, M. G. M., and Henderson, R. D. (2002). Three-dimensional instability in flow over a backward-facing step. *J. Fluid Mech.*, 473:167–190.

[11] Bayly, B. J., Orszag, S. A., and Herbert, T. (1988). Instability mechanisms in shear-flow transition. *Annu. Rev. Fluid Mech.*, 20(1):359–391.

[12] Bers, A. (1975). Linear waves and instabilities. In *Plasma physics–les houches 1972*.

[13] Biasetti, J., Gasser, T. C., Auer, M., Hedin, U., and Labruto, F. (2010). Hemodynamics of the normal aorta compared to fusiform and saccular abdominal aortic aneurysms with emphasis on a potential thrombus formation mechanism. *Ann. Biomed. Eng.*, 38(2):380–390.

[14] Biasetti, J., Hussain, F., and Gasser, T. C. (2011). Blood flow and coherent vortices in the normal and aneurysmatic aortas: a fluid dynamical approach to intra-luminal thrombus formation. *J. R. Soc. Interface*, pages 1449–1461.

[15] Biswas, G., Breuer, M., and Durst, F. (2004). Backward-facing step flows for various expansion ratios at low and moderate Reynolds numbers. *J. Fluids Eng.*, 126(3):362–374.

[16] Blackburn, H. M., Barkley, D., and Sherwin, S. J. (2008). Convective instability and transient growth in flow over a backward-facing step. *J. Fluid Mech.*, 603:271–304.

[17] Boyd, J. (1964). The influence of fluid forces on the sticking and the lateral vibration of pistons. *J. Appl. Mech.*, 31(3):397–401.

[18] Brent, R. P. (2013). *Algorithms for minimization without derivatives*. Courier Corporation.

[19] Briggs, R. J. (1964). Electron-stream interaction with plasmas.

[20] Brücker, C. (1999). The 3-d evolution and bursting of the starting vortex downstream of a backward-facing step studied by sequential high-speed scanning piv. In *Proc. 8th Int. Conf. On Laser Anemometry, Sept.*, volume 6.

[21] Chang, P. K. (2014). *Separation of flow*. Elsevier.

[22] Chen, Q. S. and Hu, W. R. (1998). Influence of liquid bridge volume on instability of floating half zone convection. *Int. J. Heat Mass Transf.*, 41(6):825–837.

[23] Chomaz, J. M., Huerre, P., and Redekopp, L. G. (1991). A frequency selection criterion in spatially developing flows. *Stud. Appl. Math.*, 84(2):119–144.

[24] Cliffe, K. A., Garratt, T. J., and Spence, A. (1993). Eigenvalues of the discretized navier-stokes equation with application to the detection of hopf bifurcations. *Adv. Comput. Math.*, 1(3):337–356.

[25] Cruchaga, M. A. (1998). A study of the backward-facing step problem using a generalized streamline formulation. *Commun. Numer. Methods Eng.*, 14(8):697–708.

[26] Denham, M. K. and Patrick, M. A. (1974). Laminar flow over a downstream-facing step in a two-dimensional flow channel. *Trans. Inst. Chem. Eng.*, 52(4):361–367.

[27] Drazin, P. G. and Reid, W. H. (1981). Hydrodynamic stability. cambridge monographs on mechanics and applied mathematics.

[28] Durst, F. and Pereira, J. C. F. (1988). Time-dependent laminar backward-facing step flow in a two-dimensional duct. *J. Fluids Eng.-T. ASME*, 110:289–296.

[29] Durst, F., Pereira, J. C. F., and Tropea, C. (1993). The plane symmetric sudden-expansion flow at low reynolds numbers. *J. Fluid Mech.*, 248:567–581.

[30] Ellingsen, T. and Palm, E. (1975). Stability of linear flow. *Phys. Fluids*, 18(4):487–488.

[31] Erturk, E. (2008). Numerical solutions of 2-d steady incompressible flow over a backward-facing step, part i: High reynolds number solutions. *Comput. Fluids*, 37(6):633–655.

[32] Escudier, M. P. and Gouldson, I. W. (1995). Concentric annular flow with centerbody rotation of a newtonian and a shear-thinning liquid. *Int. J. Heat Fluid Fl.*, 16(3):156–162.

[33] Escudier, M. P., Gouldson, I. W., and Jones, D. M. (1995). Flow of shear-thinning fluids in a concentric annulus. *Exp. Fluids*, 18(4):225–238.

[34] Ferziger, J. H. and Perić, M. (2002). *Solution of the Navier-Stokes Equations*. Springer.

[35] Fortin, A., Jardak, M., Gervais, J. J., and Pierre, R. (1997). Localization of Hopf bifurcations in fluid flow problems. *Int. J. Numer. Meth. Fluids*, 24(11):1185–1210.

[36] Furuichi, N. and Kumada, M. (2002). An experimental study of a spanwise structure around a reattachment region of a two-dimensional backward-facing step. *Exp. Fluids*, 32(2):179–187.

[37] Gartling, D. K. (1990). A test problem for outflow boundary conditions flow over a backward-facing step. *Int. J. Numer. Meth. Fluids*, 11(7):953–967.

[38] Giannetti, F. and Luchini, P. (2007). Structural sensitivity of the first instability of the cylinder wake. *J. Fluid Mech.*, 581:167–197.

[39] Goldstein, R. J., Eriksen, V. L., Olson, R. M., and Eckert, E. R. G. (1970). Laminar separation, reattachment, and transition of the flow over a downstream-facing step. *J. BASIC ENG.-T. ASME*, 92(4):732–741.

[40] Gottlieb, G. R. and Thompson, B. F. (2010). Bisected direct quadratic regula falsi. *Appl. Math. Sci*, 4(15):709–718.

[41] Gresho, P. M., Gartling, D. K., Torczynski, J. R., Cliffe, K. A., Winters, K. H., Garratt, T. J., Spence, A., and Goodrich, J. W. (1993). Is the steady viscous incompressible two-dimensional flow over a backward-facing step at Re=800 stable? *Int. J. Num. Meth. Fluids*, 17(6):501–541.

[42] Hajidavalloo, E., Sadeghi-Behbahani-Zadeh, M., and Shekari, Y. (2013). Simulation of gas–solid two-phase flow in the annulus of drilling well. *Chem. Eng. Res. Des.*, 91(3):477–484.

[43] Hobson, D. E. and Jedwab, M. (1990). Investigations of the effect of eccentricity on the unsteady fluid forces on the centrebody of an annular diffuser. *J. Fluids Struct.*, 4(2):155–169.

[44] Howell, J. S. (2009). Computation of viscoelastic fluid flows using continuation methods. *J. Comput. Appl. Math.*, 225(1):187–201.

[45] Huerre, P. and Monkewitz, P. A. (1990). Local and global instabilities in spatially developing flows. *Annu. Rev. Fluid Mech.*, 22(1):473–537.

[46] Joseph, D. D. (1976). *Stability of Fluid Motions*, volume 2. Springer-Verlag.

[47] Joseph, D. D., Bai, R., Chen, K. P., and Renardy, Y. Y. (1997). Core-annular flows. *Annu. Rev. Fluid Mech.*, 29(1):65–90.

[48] Kaiktsis, L., Karniadakis, G. E., and Orszag, S. A. (1991). Onset of three-dimensionality, equilibria, and early transition in flow over a backward-facing step. *J. Fluid Mech.*, 231:501–528.

[49] Kaiktsis, L., Karniadakis, G. E., and Orszag, S. A. (1996). Unsteadiness and convective instabilities in two-dimensional flow over a backward-facing step. *J. Fluid Mech.*, 321:157–187.

[50] Kays, W. M. and London, A. L. (1984). Compact heat exchangers.

[51] Keller, H. B. (1977). Numerical solution of bifurcation and nonlinear eigenvalue problems. In Rabinowitz, P. H., editor, *Applications of bifurcation theory*, pages 359–384. Academic Press, New York.

[52] Kelley, C. T. (1995). *Iterative Methods for Linear and Nonlinear Equations*, volume 16. SIAM.

[53] Kelvin, W. (1880). On a disturbing infinity in lord rayleigh's solution for waves in a plane vortex stratum. *Nature*, 23(1):45–46.

[54] Kim, J. and Moin, P. (1985). Application of a fractional-step method to incompressible Navier–Stokes equations. *J. Comput. Phys.*, 59(2):308–323.

[55] Koschmieder, E. L. (1993). *Bénard cells and Taylor vortices*. Cambridge University Press.

[56] Kostas, J., Soria, J., and Chong, M. (2002). Particle image velocimetry measurements of a backward-facing step flow. *Exp. Fluids*, 33(6):838–853.

[57] Lacroix, L. V. (1982). Flow-induced vibration characteristics of the bwr/5-201 jet pump. Technical report, General Electric Co., San Jose, CA (USA). Nuclear Fuel and Special Projects Div.

[58] Landahl, M. T. (1975). Wave breakdown and turbulence. *SIAM J. Appl. Math.*, 28(4):735–756.

[59] Landahl, M. T. (1980). A note on an algebraic instability of inviscid parallel shear flows. *J. Fluid Mech.*, 98(2):243–251.

[60] Lanzerstorfer, D. and Kuhlmann, H. C. (2012). Global stability of the two-dimensional flow over a backward-facing step. *J. Fluid Mech.*, 693:1–27.

[61] Lehoucq, R. B. and Scott, J. A. (1997). *Implicitly restarted Arnoldi methods and eigenvalues of the discretized Navier Stokes equations.* Citeseer.

[62] Lehoucq, R. B., Sorensen, D. C., and Yang, C. (1998). *ARPACK users' guide: solution of large-scale eigenvalue problems with implicitly restarted Arnoldi methods*, volume 6. SIAM.

[63] LeVeque, R. J., Mihalas, D., Dorfi, E. A., and Müller, E. (2006). *Computational Methods for Astrophysical Fluid Flow: Saas-Fee Advanced Course 27. Lecture Notes 1997 Swiss Society for Astrophysics and Astronomy*, volume 27. Springer Science & Business Media.

[64] Leypoldt, J. (1999). *Dreidimensionale numerische Simulation thermokapillarer Strömungen in zylindrischen Flüssigkeitsbrücken.* PhD thesis, Universität Bremen.

[65] Leypoldt, J., Kuhlmann, H. C., and Rath, H. J. (2000). Three-dimensional numerical simulation of thermocapillary flows in cylindrical liquid bridges. *J. Fluid Mech.*, 414:285–314.

[66] Macagno, E. O. and Hung, T. K. (1967). Computational and experimental study of a captive annular eddy. *J. Fluid Mech.*, 28(1):43–64.

[67] Mateescu, D. and Païdoussis, M. P. (1987). Unsteady viscous effects on the annular-flow-induced instabilities of a rigid cylindrical body in a narrow duct. *J. Fluids Struct.*, 1(2):197–215.

[68] Mateescu, D., Païdoussis, M. P., and Bélanger, F. (1991). Computational solutions based on a finite difference formulation for unsteady internal flows. In *AIAA 29th Aerospace Science Meeting. Reno. AIAA Paper*, number 91-0724.

[69] Meerbergen, K., Spence, A., and Roose, D. (1994). Shift-invert and Cayley transforms for detection of rightmost eigenvalues of nonsymmetric matrices. *BIT Numer. Math.*, 34(3):409–423.

[70] Moffatt, H. K. (1964). Viscous and resistive eddies near a sharp corner. *J. Fluid Mech.*, 18(1):1–18.

[71] Mohamed, A. G., Valentine, D. T., and Hassel, R. E. (1991). Numerical study of laminar separation over an annular backstep. *Comput. Fluids*, 20(2):121–143.

[72] Mott, J. E. and Joseph, D. D. (1968). Stability of parallel flow between concentric cylinders. *Phys. Fluids*, 11(10):2065–2073.

[73] Mulcahy, T. M. (1988). One-dimensional leakage-flow vibration instabilities. *J. Fluids Struct.*, 2(4):383–403.

[74] Mullin, T., Seddon, J. R. T., Mantle, M. D., and Sederman, A. J. (2009). Bifurcation phenomena in the flow through a sudden expansion in a circular pipe. *Phys. Fluids*, 21(1):014110.

[75] Nie, J. H. and Armaly, B. F. (2003). Reattachment of three-dimensional flow adjacent to backward-facing step. *J. Heat Transfer.*, 125(3):422–428.

[76] Nienhüser, C. (2002). *Lineare Stabilität achsensymmetrischer thermokapillarer Konvektion in Flüssigkeitsbrücken mit statisch und dynamisch deformierbarer Grenzfläche.* PhD thesis, University of Bremen.

[77] Orr, W. M. (1907). The stability or instability of the steady motions of a perfect liquid and of a viscous liquid. part i: A perfect liquid. In *Proc. Roy. Irish Acad. A*, volume 27, pages 9–68. JSTOR.

[78] Orszag, S. A. (1971). Accurate solution of the Orr–Sommerfeld stability equation. *J. Fluid Mech.*, 50(4):689–703.

[79] Paidoussis, M., Mateescu, D., and Sim, W. (1990). Dynamics and stability of a flexible cylinder in a narrow coaxial cylindrical duct subjected to annular flow. *J. Appl. Mech.-T. ASME*, 57(1):232–240.

[80] Paidoussis, M. P. (1985). The unsteady potential flow in an axially variable annulus and its effect on the dynamics of the oscillating rigid center-body. *J. Fluids Eng.*, 107:421–422.

[81] Païdoussis, M. P. (1987). Flow-induced instabilities of cylindrical structures. *Appl. Mech. Rev.-T. ASME*, 40(2):163–175.

[82] Paidoussis, M. P. and Pettigrew, M. J. (1979). Dynamics of flexible cylinders in axisymmetrically confined axial flow. *J. Appl. Mech.*, 46(1):37–44.

[83] Press, W. H. (1989). *Numerical recipes in Pascal: the art of scientific computing*, volume 1. Cambridge University Press.

[84] Rayleigh, L. (1917). On the dynamics of revolving fluids. *Proc. R. Soc. A*, 93(648):148–154.

[85] Reynolds, O. (1883). An experimental investigation of the circumstances which determine whether the motion of water shall be direct or sinuous, and of the law of resistance in parallel channels. *Proceedings of the royal society of London*, 35(224-226):84–99.

[86] Reynolds, O. (1894). On the dynamical theory of incompressible viscous fluids and the determination of the criterion. *Proc. R. Soc. A*, 56(336-339):40–45.

[87] Romanò, F. (2016). *Particle Accumulation in Incompressible Laminar FLows due to Particle–Boundary Interaction*. PhD thesis, Technische Universität Wien.

[88] Sadeghi, V. M. and Higgins, B. G. (1991). Stability of sliding couette–poiseuille flow in an annulus subject to axisymmetric and asymmetric disturbances. *Phys. Fluids*, 3(9):2092–2104.

[89] Sanmiguel-Rojas, E. and Mullin, T. (2012). Finite-amplitude solutions in the flow through a sudden expansion in a circular pipe. *J. Fluid Mech.*, 691:201–213.

[90] Schultz, A. and Pfister, G. (2000). Bifurcation and structure of flow between counter-rotating cylinders. *Lecture Notes in Phys.*, 549:37–54.

[91] Scott, P., Mirza, F., and Vlachopoulos, J. (1986). A finite element analysis of laminar flows through planar and axisymmetric abrupt expansions. *Comput. Fluids*, 14(4):423–432.

[92] Seydel, R. (2009). *Practical bifurcation and stability analysis*, volume 5. Springer Science & Business Media.

[93] Shah, R. K. and London, A. L. (2014). *Laminar flow forced convection in ducts: a source book for compact heat exchanger analytical data*. Academic press.

[94] Sipp, D. and Jacquin, L. (2000). Three-dimensional centrifugal-type instabilities of two-dimensional flows in rotating systems. *Phys. Fluids*, 12(7):1740–1748.

[95] Sohn, J. L. (1988). Evaluation of FIDAP on some classical laminar and turbulent benchmarks. *Int. J. Numer. Meth. Fluids*, 8(12):1469–1490.

[96] Taylor, G. I. (1923). Stability of a viscous liquid contained between two rotating cylinders. *Philosophical Transactions of the Royal Society of London. Series A, Containing Papers of a Mathematical or Physical Character*, 223:289–343.

[97] Theofilis, V. (2003). Advances in global linear instability analysis of nonparallel and three-dimensional flows. *Prog. Aerospace Sci.*, 39(4):249–315.

[98] Theofilis, V. (2011). Global linear instability. *Annu. Rev. Fluid Mech.*, 43:319–352.

[99] Thomas, L. H. (1953). The stability of plane poiseuille flow. *Phys. Rev.*, 91(4):780–783.

[100] Thompson, J. F. (1984). Grid generation techniques in computational fluid dynamics. *AIAA J.*, 22(11):1505–1523.

[101] Tylli, N., Kaiktsis, L., and Ineichen, B. (2002). Sidewall effects in flow over a backward-facing step: Experiments and numerical simulations. *Phys. Fluids*, 14(11):3835–3845.

[102] Versteeg, H. K. and Malalasekera, W. (2007). *An introduction to computational fluid dynamics: the finite volume method*. Pearson Education.

[103] Vinokur, M. (1983). On one-dimensional stretching functions for finite-difference calculations. *J. Comput. Phys.*, 50(2):215–234.

[104] Wanschura, M. (1996). *Lineare Instabilitäten kapillarer und natürlicher Konvektion in zylindrischen Flüssigkeitsbrücken*. PhD thesis, Universität Bremen.

[105] Wanschura, M., Shevtsova, V. M., Kuhlmann, H. C., and Rath, H. J. (1995). Convective instability mechanisms in thermocapillary liquid bridges. *Phys. Fluids*, 7(5):912–925.

[106] Wesseling, P. (2009). *Principles of computational fluid dynamics*, volume 29. Springer Science & Business Media.

[107] Williams, P. T. and Baker, A. J. (1997). Numerical simulations of laminar flow over a 3d backward-facing step. *Int. J. Numer. Meth. Fluids*, 24(11):1159–1183.